Microbially Influenced Corrosion in Sour Environments

by

Kwan Li

B.S., Duke University (2011)

Submitted to the Department of Materials Science and Engineering
in partial fulfillment of the requirements for the degree of

Master of Science in Materials Science and Engineering

at the

MASSACHUSETTS INSTITUTE OF TECHNOLOGY

February 2014

Author .....
Department of Materials Science and Engineering
January 9th, 2014

Certified by .....
Krystyn J. Van Vliet
Associate Professor of Materials Science and Engineering
Thesis Supervisor

Accepted by .....
Gerbrand Ceder
Chair, DMSE Committee on Graduate Students

Contents

List of Figures

List of Tables

Microbially Influenced Corrosion in Sour Environments
by
Kwan Li

Submitted to the Department of Materials Science and Engineering
on January 16th, 2014, in partial fulfillment of the
requirements for the degree of
Master of Science in Materials Science and Engineering

Abstract

Microbially influenced corrosion (MIC) is a costly and poorly understood source of corrosion that plagues many modern industrial processes such as oil extraction and transportation. Throughout the years, many possible mechanisms for MIC have been proposed. One specific proposed mechanism was tested in this thesis: that the metal-binding characteristic of bacterial biofilms enhanced corrosion when it appears in conjunction with an iron sulfide film. Two model biogels were used: calcium alginate, which has this metal-binding property, and agarose, which does not.

In pursuit of this hypothesis, iron sulfide films were grown on mild steel coupons. Two distinct forms of iron sulfides were grown: a loose black product at low sulfide concentrations, and an adherent gold product at high sulfide concentrations. Many materials characterization techniques were attempted, and the black corrosion product was found to be a mixture of greigite and marcasite. However, this composition was observed to change irreversibly with the application of a laser that caused the material to either heat and/or dry. The resulting golden-colored corrosion product was found to consist mainly of monosulfides, implying the presence of mackinawite or pyrrhotite.

By using electrochemical polarization experiments, it was found that calcium alginate enhanced the rate of corrosion; agarose reduced the rate of corrosion. This is in contrast to previously published literature. Contrary to the initial hypothesis, adding an underlying iron sulfide film did not appreciably alter the measured rate of corrosion. Additionally, it was found that biofilms generated by sulfate-reducing bacteria (SRB) enhanced corrosion in a manner similar to the calcium alginate gel, and lysing the cells within the biofilm did nothing to alter this effect. This implies that the biofilm itself, even in the absence of active bacterial metabolic activity, can enhance corrosion rates observed in MIC.

Thesis Supervisor: Krystyn J. Van Vliet
Title: Associate Professor of Materials Science and Engineering

Chapter 1

The Role of the Biofilm in Microbially Influenced Corrosion

1.1 Challenges of Microbially Influenced Corrosion

Microbially influenced corrosion (MIC) is accelerated corrosion that occurs in the presence of or due to the action of biological agents such as, but not limited to, bacteria, fungi, archaea, and other microorganisms. Of the approximate $300 billion USD direct annual losses due to corrosion in the United States alone, 20% of it is estimated to be a result of MIC, totaling a cost of $100 million USD per year in the gas and oil industry alone [1]. MIC has been noted to occur for a variety of metals and alloys such as iron and steel, copper, and titanium as well as for nonmetallic materials like concrete or ceramics. MIC occurs across a wide range of environments ranging from oil and water pipelines and machinery to biomedical devices [2, 3]. For example, MIC has been implicated in several rapid, high-profile failures of installations [4], leaks in a stainless steel cooling water system [5], and leaks in the Trans-Alaskan Pipeline [6]. All told, MIC and its associated biofouling are estimated to account for 20% of direct fuel pipeline integrity and reliability costs exceeding $2 billion USD per year worldwide.

Despite decades of research, the exact mechanisms and environments through which MIC enhances corrosion remain poorly understood owing to the complexity of the microbe-metal interaction. Indeed, even within the same oilfield or pipeline, some locations may exhibit MIC while others do not [5, 7, 8]. The genetic variation, mutations, and interactions among bacterial species render MIC difficult to study, as two different species of bacteria within the same genus can corrode quite differently [9], or that a mixed culture of two different species can corrode faster than pure

cultures of either species [10].

Clearly, MIC is a complex problem that plagues industrial processes worldwide. It is particularly important in industries where large scale machinery is exposed to uncontrolled chemical environments, namely buried and deep ocean pipelines. Adding to this is the fact that MIC is a problem that encompasses several disparate fields of study; traditionally, MIC has been studied either from a purely biological perspective – investigating the nature and biology of the wild bacteria consortia – or from a purely materials corrosion perspective – investigating the interplay between the material and its chemical environment under controlled conditions. In recent years, as interdisciplinary collaborations become more commonplace and laboratory techniques continue to improve, large strides in the study of MIC can be seen. This chapter lays the foundation for the rest of this thesis by giving an introduction to the electrochemical process that is corrosion; as well as by presenting a review of the characteristics of MIC, the mitigation techniques used against it, and the proposed mechanisms that have been hypothesized in the literature. This chapter also draws chiefly from a recent review co-authored by the thesis author [11].

1.2 Characteristics of Microbially Influenced Corrosion

MIC can occur in both aerobic an anaerobic environments and is characterized by three key features: the presence of pitting corrosion (Figure 1-1), an enhanced rate of corrosion relative to the equivalent abiotic environment, and the presence of a biofilm (Figure 1-2) [1].

Pitting corrosion consists of the development of small surface defects with diameters typically on the order of millimeters, but can be as small as on the order of micrometers [12]. Because of their small size and possible deep penetration into the core of the corroded structure, this form of corrosion can be both difficult to detect and devastating in damages caused. These pits can both act as stress concentrators – leading to cracking of the metal and as weak points in whatever protective surface treatments that had previously been applied to the metal. The presence of certain bacteria have been shown to greatly decrease the time to failure of mild steel in stress corrosion cracking tests [1]. Bacteria are known to adhere preferentially to anodic sites such as welded joints, scratched edges, grain boundaries, or to pre-existing pits, making it unclear whether the bacteria actually initiated the pits or not [13]. Moreover, studies have found no unique characteristics that distinguish the morphology of MIC pits from abiotic pits [12]. These latter two factors render the study of MIC pitting difficult to approach.

The corrosion rate due to MIC has been measured to be greater than that of

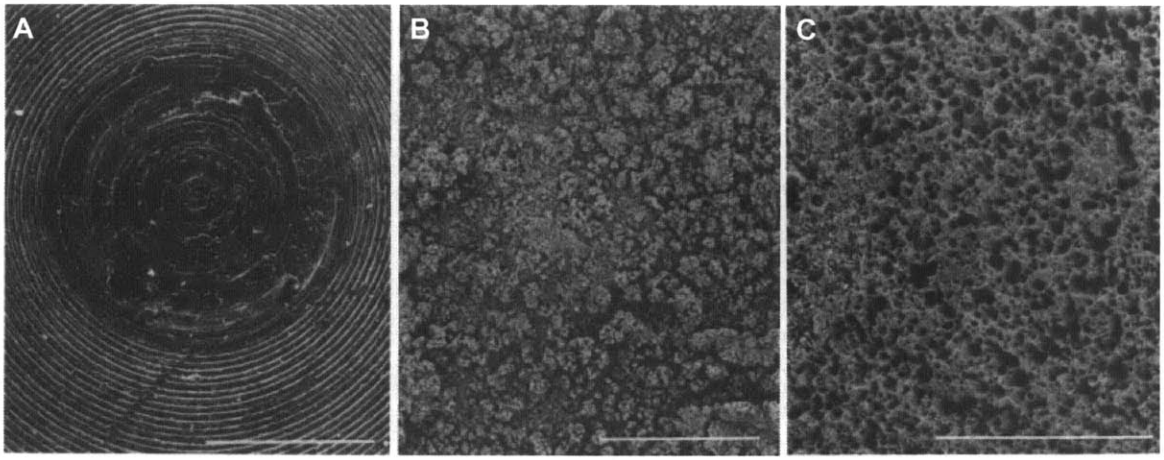

Figure 1-1: Scanning electron microscopy images which demonstrate the growth and pitting damage caused by sulfate-reducing bacteria growth on SAE 1020 steel studs. (A) Control stud showing concentric rings from lathe cutting; scale bar, 500 μm. (B) sulfate-reducing bacterial biofilm deposit after 64 days; scale bar, 500 μm. (C) Corroded stud after biofilm removal revealing severe pitting damage; scale bar, 500 μm [14].

the equivalent chemical environment. For example, sulfate-reducing bacteria (SRB) reduce sulfates for energy as part of their metabolism, generating hydrogen sulfide in the process. King et al. conducted a comparison between an active SRB colony on a metal coupon and an abiotic system to which Na_2S was added periodically to match the sulfide concentration generated by the SRB [15], . These authors found a corrosion rate approximately 8 times greater in the biotic sample than in the abiotic sample.

MIC is also characterized by the presence of a biofilm, an aggregation of microbial cells embedded in a matrix of extracellular polymeric substance (EPS). EPS is a polymeric conglomeration of microbially generated proteins, DNA, and polysaccharides that aid in binding the living cells both to each other and to the material surface [10]. In general, many different species of bacteria and other microorganisms coexist within this biofilm, and their disparate activity creates distinct chemical gradients – both in species consumed and metabolites produced – throughout the film. Most importantly, the consumption of oxygen by aerobic bacteria within the biofilm creates an anaerobic region near the material surface, allowing anaerobic bacteria such as SRB to thrive. These biofilms can be anywhere from micrometers to millimeters in thickness and can develop and mature over the course of hours to months, depending

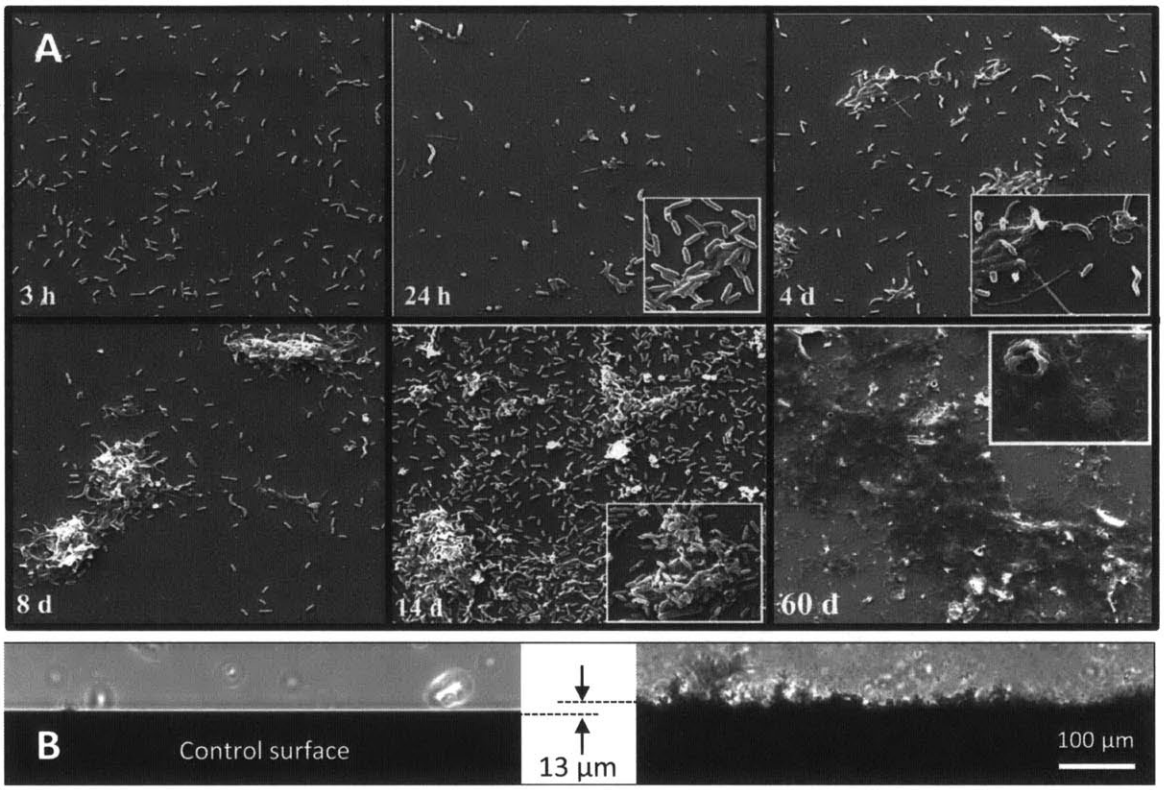

Figure 1-2: (A) Scanning electron microscopy images demonstrating the growth a biofilm over the course of 60 days. All images are at 1000x except for 60 days which is 200x. Inner boxes are at 4000x. [17]. (B) Image demonstrating a cross section of the combined biofilm/corrosion product layer after 2 days of growth of *Desulfovibro vulgaris* on music spring quality steel (ASTM A228) [11].

upon the bacterial species and environment involved [16].

1.2.1 Sulfate reducing bacteria

Though many species of bacteria have been implicated in MIC, the most well studied is the sulfate reducing bacteria (SRB). In fact, the count of SRB cells per milliliter is often used as a measure for MIC risk in industrial applications [1]. SRBs span many genera, with the genus *Desulfrovibrio* commonly found both in nature and as a laboratory model, but all are defined by their ability to reduce sulfates to sulfides as part of their metabolism:

$$SO_4{}^{2-} + CH_3COOH \rightarrow HS^- + 2HCO_3^- + H^+ \quad (1.1)$$

where acetic acid (CH_3COOH) is shown as an example of an electron donating organic energy source; SRBs are capable of metabolizing lactic acid and other organic molecules depending upon the species. Most SRB are considered obligate anaerobes, meaning that the cells cannot metabolize or replicate in the presence of oxygen though many species are able to temporarily tolerate low levels of oxygen [18]. Their involvement at instance of MIC events are marked by deposits of iron sulfide corrosion products and the characteristic "rotten egg" smell of H_2S that is produced as a result of their metabolism, as illustrated by equation 1.1.

1.3 Mitigation Techniques

A number of techniques have been investigated to mitigate the effects of MIC, including the use of corrosion resistant metals, protective coatings, anodic and cathodic protection, biocides, the introduction of competing bacteria, and nutrient addition or removal. Cathodic protection – in which either an active DC current is applied to the protected metal or a sacrificial metal such as zinc is used – works reasonable well, but as an active process it is costly, thus increasing interest into the development of cheaper passive techniques [19]. Moreover, cathodic protection – as an electrochemical technique – does nothing to mitigate the aggregation of biologic material which can potentially cause backup and blockage in a flow environment such as a gas or water pipeline. Since MIC results in pitting corrosion, both the use of anodic protection and passivating metals such as stainless steels are inherently risky. The same is true for other forms of protective coatings – a small localized disruption in the protective layer may lead to highly localized damage.

Attempts to mitigate MIC through biological means have been met with mixed results [19]. The use of biocides targeted toward SRB is standard practice in the gas and oil industries, but such efforts require constant addition of biocides to be efficacious. Studies have shown that upon ceasing the biocide treatment, the population of SRB quickly recovers. Moreover, the elimination of SRB from the environment does not negate the effect of other types of bacteria which can also cause MIC. In fact, the elimination of SRB may introduce an ecological niche into which other corrosive bacteria may proliferate. In [20], the authors found MIC corrosion in a diesel and naptha pipeline in India in which SRBs were eliminated through biocide addition; they concluded that the main culprits in this instance of MIC were the iron oxidizing bacteria that the biocide could not eliminate. It should be noted that the use

of targeted biological techniques such as biocide addition and nutrient modification is greatly dependent upon having previous knowledge on the microbial composition of the environment in question. As such, a standard treatment that applies to all environments cannot be developed.

In recent years, studies have also been conducted to test the effectiveness of introducing a competing bacteria species to the environment. The idea is that these bacteria, selected for their inability to cause MIC, will outcompete the more damaging, naturally occurring species. Figure 1-3 illustrates one such study carried out by Thorstenson et al. In this experiment, nitrate reducing bacteria were made to proliferate at the expense of other species through the addition of nitrates to the environment at an oil production facility in the North Sea [21]. Figure 1-3 shows a marked decrease in the SRB population upon nitrate addition, but this technique does not provide a definitive solution. Like with biocide addition, SRB population rapidly recovers when the nitrate treatment is terminated [22]. Lastly, the addition of chemicals such as biocides or nitrates to the environment may introduce unattractive economic costs not only in the cost of addition but also in the cost of removal.

Currently, constant vigilance remains the best safeguard against MIC. Frequent cleanings prevent bacterial buildup, and frequent inspections allow the discovery of damage before it reaches a critical level.

1.4 The Anatomy of a Corrosion Cell

Before continuing onward to the mechanisms of MIC, it is important to review the fundamentals of corrosion. Figure 1-4 shows a schematic of a corrosion cell on a metal surface. Corrosion is an electrochemical process characterized by the destruction of a material through interaction with its environment. In metals, corrosion is characterized by the dissolution of zero valent metal at an anodic site, yielding the two following half-cell reactions:

$$\text{Anode:} \qquad M^0 \rightarrow M^+ + e^- \tag{1.2}$$

$$\text{Cathode:} \qquad A^+ + e^- \rightarrow A \tag{1.3}$$

where M^0 is the solid phase metal and A^- is an oxidant, the nature of which will vary depending upon the environment. In an aqueous environment, common oxidants may be oxygen molecules, hydrogen cations, or any other electronegative species. The anode and the cathode of a corrosion cell are defined as the locations where reactions 1.2 and 1.3 occur, respectively. In general, the location of the anode and

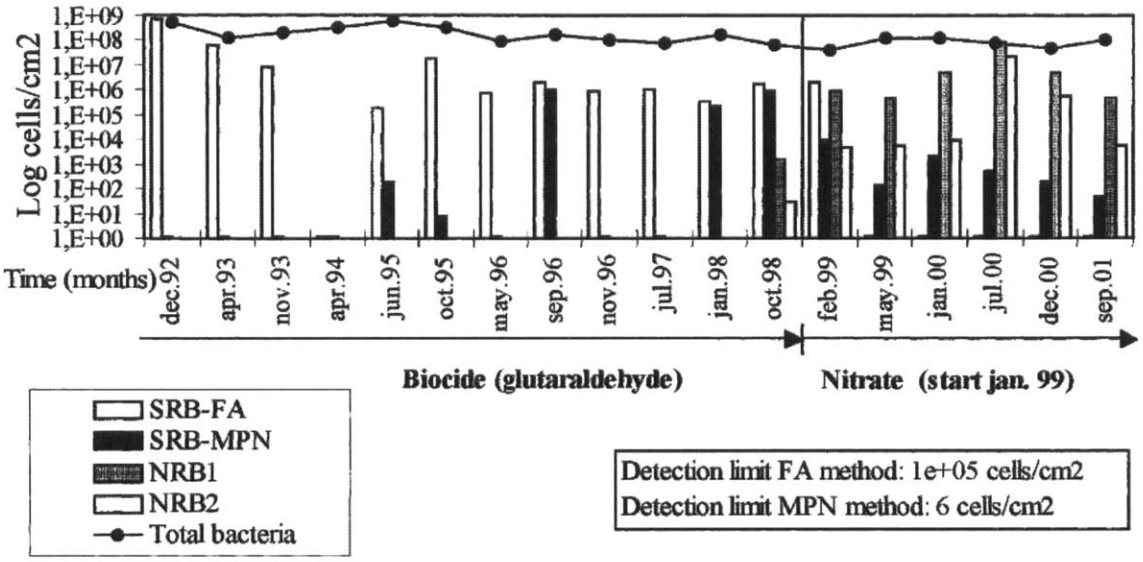

Figure 1-3: Measured data on the bacteria content of a floating unit at Veslefrikk, an oil production facility in the North Sea. Production began in 1989, utilizing a biocide treatment until January 1999 when it was stopped in favor of nitrate injection. A subsequent decrease in sulfate-reducing bacteria (SRB) and increase nitrate-reducing bacteria (NRB) numbers was observed. The population of SRB was characterized using a fluorescent antibody (FA) technique as well as the "most probable number" (MPN) method. Two types of NRB were measured using the MPN method: NRB1 which are facultative anaerobes, and NRB2 which are obligate anaerobes [21].

cathode are not fixed and, for a defect free surface, each location has equal odds of serving as the anode at any given moment. This *wandering anode* behavior leads to a general dissolution of the metal surface in a morphology known as uniform attack. Such types of corrosion are typically easy to detect and to prevent. Defects on the surface or irregularities in the environment, however, may bias a particular location toward anodic behavior, fixing the anode in place, causing localized corrosion. Such types of corrosion are more damaging not only because they are more difficult to detect, but also because the damage to the integrity of corroding material become concentrated in one location. Examples of localized corrosion include inter-granular attack, crevice corrosion, and pitting.

The flow of metal ions out of the anode and of electrons out of the cathode generates an anodic current and a cathodic current, respectively. Figure 1-4 shows the proper orientation of these currents. At equilibrium, these two current must be equal in magnitude for corrosion to be sustained. If the size of the anode and cathode are not comparable, however, the current density may be greatly imbalanced. This is another reason why localized corrosion can be so damaging – a localized anode is typically supported by a much larger cathode, resulting in a very high current density at the anode.

The electrochemical reactions in 1.2 and 1.3 each occur at a standard potential, measured in voltage, that is referenced to the Standard Hydrogen Electrode (SHE) which has a potential of $0V$. The SHE is defined as the reaction $2H^+ + 2e^- \rightarrow H_2(g)$ occuring at unit activity of hydrogen ions and 1 bar pressure of $H_2(g)$. The difference in the standard potentials of reactions 1.2 and 1.3 is the corrosion potential, as can be seen in Figure 1-4. This potential can deviate from the nominal standard value when the environment deviates from standard conditions, e.g. non-unit activities or non-standard temperatures. At equilibrium, this corrosion potential is also known as the open circuit voltage (OCV).

At the cathode, the oxidant, denoted by A^+ in Figure 1-4, can become adsorbed onto the metal surface. Adsorption is a process which occurs during the charge transfer step of the cathodic reaction, but it may become stuck on the surface if the affinity of the reduced species A to the surface is high. Should this happen, this $A_{adsorbed}$ inhibits further cathodic reactions by restricting the metal's access to the environment, causing a negative charge buildup at the cathode, shifting the overall corrosion potential to be more negative. This process is known as cathodic polarization. Likewise, at the anode the corrosion product MB may prevent further metal ions from escaping the metal, causing a buildup of positive charges to cause anodic polarization. Passivation is a special form of the latter process where the corrosion product coats the entire metal surface, restricting the metal's access to

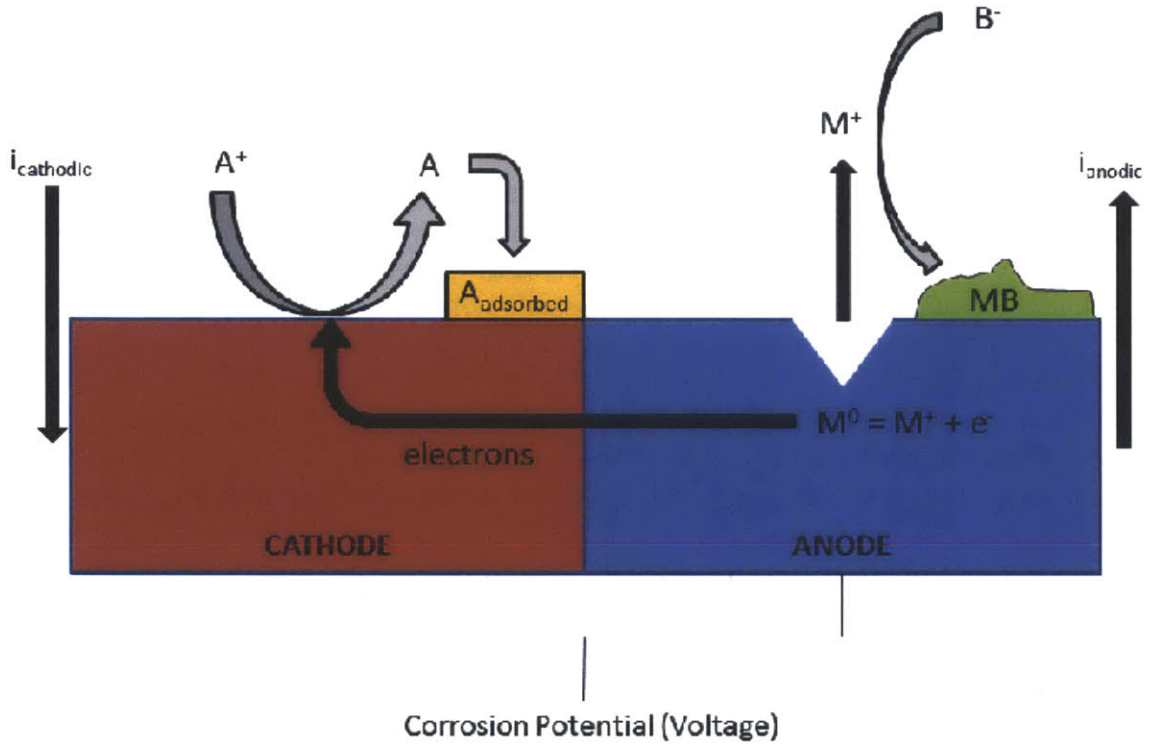

Figure 1-4: At the cathode, an oxidizing species in the electrolyte denoted here by A^+ is reduced by electrons from the metal's surface; this reduced species, A, may then become adsorbed onto the metal's surface. At the anode, the zero valent metal is oxidized into its ion, releasing one or more electrons into the bulk of the metal; this metal ion is released into the electrolyte where it may react with the species present, denoted here by B, to precipitate as a corrosion product MB.

the environment entirely, greatly reducing the rate of reaction. Stainless steel, for example, does not rust as quickly as low-carbon steel because a layer of chromium oxide corrosion product coats the entire surface [23].

1.5 Mechanisms of Microbially Influenced Corrosion

Owing to the complexity of the microbe-metal interaction, the underlying mechanism of MIC remains an open question and subject to much debate. Many possible mechanisms for MIC have been proposed, and it is possible that no predominant mechanism exists. In fact, this seems likely given the incredible diversity of species and conditions in which MIC is observed. It is known that chemical, mechanical and structural factors all play a role, both biotic and abiotic in nature, and these may all work in concert to cause and sustain MIC [24]. Thus, it must be emphasized that evidence for one hypothesis is not necessarily contradictory to another. The given environmental conditions and bacterial species present may dictate the predominant mechanisms.

Among the first proposed mechanisms of MIC, the cathodic depolarization theory – also known as the classical theory – was put forth in 1934 by Kuhr et al. in order to explain the unexpectedly high rate of corrosion failures encountered on buried cast iron pipelines in the Dutch countryside [25]. SRB were identified as the culprit due to the ferrous sulfide corrosion products found in conjunction with these failures. In anaerobic conditions where SRB thrive, hydrogen ions typically serve as the terminal electron acceptor at the cathode in a corrosion reaction. This reduced hydrogen would then adsorb onto the metal surface, polarizing it. According to the classical theory, the role of the SRB was to consume this cathodic hydrogen by means of the enzyme hydrogenase, catalyzing the recombination of the adsorbed hydrogen into hydrogen gas, thus depolarising the cathode.

Though the classical theory was grounded in electrochemistry and found general acceptance for nearly half a century, it was ultimately overturned when new techniques showed that hydrogenase can act only on molecular hydrogen, not atomic hydrogen [26]. In support of this finding, Cord-Ruwisch et al. showed that nitrate-reducing bacteria with an enhanced ability to consume hydrogen failed to cause noticeable corrosion [27]. Despite these findings, however, research continues into the role of hydrogenase in MIC, often with contradictory results. Studies by Bryant et al. [14] and Da Silva et al. [28] showed a positive correlation between the presence of hydrogenase and MIC, while King et al. [15] found no such link.

Following the fall of the classical theory, myriad "alternative theories" have been proposed, often attempting to explain MIC while minimizing the role of the bacteria

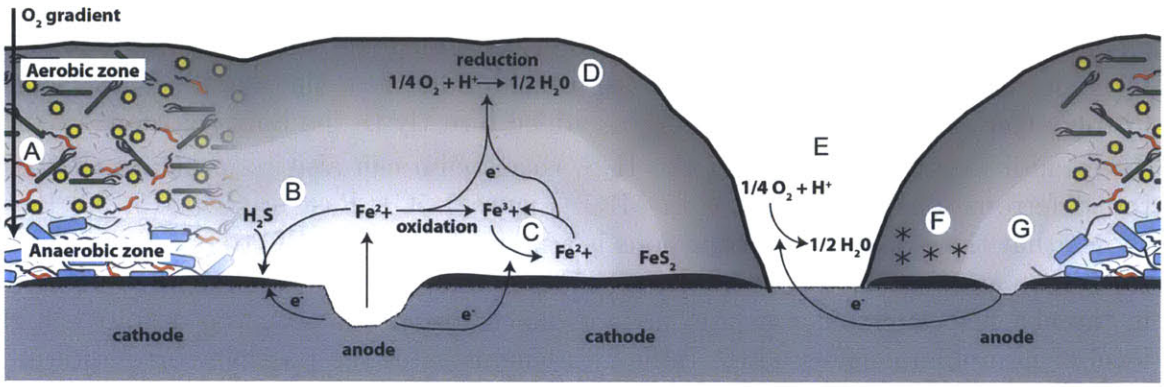

Figure 1-5: Mechanisms by which a biofilm can contribute to corrosion. (A) creation of anaerobic zones; (B) concentration of corrosive chemicals; (C) concentration of ferrous ions; (D) electron conduction away from surface; (E) creation of differential aeration zones; (F) binding of corrosion promoters; (G) disruption of passivating film. [11]

themselves [1]. Such theories include anodic depolarization [29], the presence of a volatile phosphorus compound [30], metal-binding exopolymers [31], sulfide-induced stress corrosion cracking and hydrogen-induced blistering [32]. Here, however, we restrict our focus to the biofilm and its role in MIC. Figure 1-5 illustrates the mechanisms by which a biofilm can contribute to corrosion initiation and accelerated corrosion rates.

1.5.1 The biofilm as a chemical barrier

The existence of a biofilm can impede the diffusion of chemical species – both into and out of the biofilm – producing localized chemical environments that are significantly different from the bulk [10]. These localized environments can, in turn, greatly affect the underlying corrosion in a number of ways (Figure 1-5). In aerobic conditions, the oxygen concentration may differ greatly across the biofilm due both to O_2 diffusion limitations as well as O_2 consumption by aerobic bacteria. Thus, even in an aerated environment, anaerobic regions can develop beneath a biofilm, allowing for the proliferation of SRB and other corrosion-enhancing anaerobes (Figure 1-5A). By inhibiting the diffusion of corrosive chemicals away from the metal surface, the biofilm can effectively act as a concentration multiplier. The H_2S generated by SRB in anaerobic regions is potentially much more potent when encapsulated beneath a biofilm than otherwise (Figure 1-5B). King et al. demonstrated a significant differ-

ence in the rate of corrosion between an SRB colony and a sterile medium to which an equivalent quantity of sulfide was periodically added [15]. In the former case, the biogenic sulfides were produced beneath a biofilm and near the metal surface, while in the latter case the abiotic sulfide was added directly to the bulk solution.

In addition to concentrating the H_2S, the biofilm can also concentrate the corroded ferrous ions, a key factor in MIC (Figure 1-5C). Past studies [15, 33] have shown that the presence of ferrous ions is a major factor for MIC to occur on iron or steel in an aqueous environment. Lee et al. for example, grew a pure culture of SRB in the absence of ferrous ions and little to no corrosion was observed despite a high level of microbial activity [33]. Table 1.1 demonstrates the positive correlation between ferrous ion concentration and corrosion rates. This strong correlation implies that ferrous ions play an integral part in the corrosion mechanism of MIC, at least in the presence of SRB. Two possible roles may be suggested: that the ferrous/ferric ion (Fe^{2+}/Fe^{3+}) redox couple plays a significant role, and/or the ferrous corrosion products do. It should be mentioned that ferrous ions are not known to affect the metabolism of SRB in any manner, though other bacteria are known to use them to cause corrosion on metals other than steel, such as *Acidithiobacillus ferrooxidans* in the industrial process of bioleaching [34].

In a metal/solution interface between iron and aqueous ferrous and ferric ion, a galvanic cell is established and the following two half-cell reactions take place:

$$\text{Cathode:} \quad Fe^{3+} + e^- \rightarrow Fe^{2+} \qquad E^0 = 0.77V \tag{1.4}$$

$$\text{Anode:} \quad Fe^0 \rightarrow Fe^{2+} + 2e^- \qquad E^0 = 0.44V \tag{1.5}$$

$$\text{Overall:} \quad 2Fe^{3+} + Fe^0 \rightarrow 3Fe^{2+} \qquad E^0 = 1.21V \tag{1.6}$$

where the standard electrode potentials are referenced to the standard hydrogen electrode. When bound to functional groups in the biofilm, these potentials may become even more conducive toward corrosion, as previously discussed. Nevertheless, as an oxidant, ferric ions ($E^0 = 0.77V$) are more reducing than hydrogen ($E^0 = 0V$) but less than oxygen ($E^0 = 1.23V$), meaning that at the same ion concentrations, a cathodic reaction involving oxygen would be preferred. However, the strength of ferric ions as an oxidant in the corrosion of iron or steel is a positive feedback loop, as illustrated in Figure 1-5C. Unlike in the oxygen reduction reaction wherein the reactant oxygen molecules are continually consumed – potentially leading to diffusion limiting kinetics – ferrous ions are continually regenerated as this corrosion reaction proceeds. Moreover, each new ferrous ion is generated at the interface, preventing the development of diffusion limited kinetics. These ferrous ions can then be oxidized by

Table 1.1: Relationship between ferrous ion concentration and corrosion rate, adapted from [15].

Source	Ferrous ion concentration, mM	Average corrosion rate, mg/dm^2day	Standard deviation
Booth & Wormwell [35]	0.025	4.04	1.75
Booth, Shinn & Wakerley [36]	0.125	3.0	-
Booth & Wormwell [35]	1.25	9.5	0.3
King, R.A. Ph.D Thesis, Univ. Manchester 1971	5.0	11.0	-
Bunker Report [37]	10.7	17.5	1.5
Booth, Cooper & Wakerley [38]	12.75	20.87	3.39
King, Miller & Wakerley [15]	20	21.2	2.47
King, Miller & Wakerley [15]	38.2	24	-
Booth, Cooper & Cooper [39]	510	95	-

oxygen to restore the ferric ion concentration. For pH > 4.5, the rate of this reaction is known to be very fast and thus does not limit the rate of corrosion [40].

The presence of the biofilm aids this mechanism in two ways: first, it further concentrates the ferric ions near the metal surface, and second it spatially separates the two oxidation reactions [10]. Figure 1-5D illustrates the second point: electrons lost by ferrous ions in the anaerobic zone can travel through the conductive biofilm to be accepted by oxygen in the aerobic zone. By removing the need for either species to diffuse through the biofilm, the rate of the corrosion reaction can thus be greatly increased. This suggests that the presence of the biofilm, rather than the presence of the bacteria that made and stabilized that biofilm, directly increases corrosion rate. Separately, we note that species of iron-oxidizing bacteria, which as part of their metabolism oxidizes Fe^{2+} to Fe^{3+}, have been identified at MIC events, and these have also been implicated as a potential cause for MIC [41].

1.5.2 Physical structure of the biofilm

The physical structure and heterogeneous nature of the biofilm also contribute to the corrosion process. Biofilms are often patchy and of varying thickness at the microscale, creating isolated pockets of oxygen depletion which can instigate localized corrosion through the establishment of differential aeration cells (Figure 1-5E) [42]. Roe et al. have demonstrated this effect [43]. They placed a μm-thick patch of agarose – a biogel with an oxygen diffusivity that is slightly lower than that of water on to a low-carbon steel coupon, and observed localized corrosion beneath the abiotic film. Additionally, it has been proposed that enzymes embedded within the biofilm – such as hydrogenase – or other chemical properties of the biofilm may also enhance corrosion (Figure 1-5F) [10]. The complexation of metal ions by functional groups, for example, is thought to enhance corrosion by altering the redox potential of ferrous ions within the biofilm[10], though Roe et al. found no evidence to support this hypothesis [43].

In the presence of SRB, ferrous ions will also form iron sulfide corrosion products, the exact form and composition of which are difficult to predict. It is known that iron sulfides can transition from unstable, oxygen-reactive phases such as mackinawite to pyrrhotite and to stable pyrite FeS_2 [44], but in practice the conversion is spatially and temporally heterogeneous. Cwalina et al. have noted a difference in the structure of iron sulfides formed biotically versus abiotically, the former referred to as "amorphous precipitates" and the latter as "crystalline sediments" [45]. Regardless, iron sulfides are cathodic toward iron, but this effect may be both protective and destructive [46, 47, 26]. Much like the passive chromium oxide film found on

stainless steel, a stable film of iron sulfide may protect the metal surface from further corrosion, but even a small disruption in this film can lead to a high rate of crevice or pitting corrosion due to the massive size disparity between the iron sulfide cathode and the exposed ferrous (iron or steel) anode. Of the various forms of iron sulfide, pyrite (cubic FeS_2) is known to be the most stable and also the most corrosive at any sites of film disruption [48]; FeS_2 is also known to be susceptible to dissolution in the presence of certain bacteria such as *Acidithiobacillus ferrooxidans* [34].

The effect of a biofilm upon this passive film, however, is subject to much debate. Its presence may stabilize this passive film by acting as a physical binder and a protective coating. On the other hand, biofilm presence could potentially inhibit the formation and of such an inorganic film, or facilitate localized destabilization of such a coating (Figure 1-5G). Intriguingly, experiments by Lee et al. [33] demonstrate both possibilities, differing only in the order of arrival of the biofilm versus the iron sulfide film. Less well-controlled, industrial environments such as oil pipelines include fluid flow and the continual formation and disruption of both iron sulfides and biofilms. In such contexts, the order of arrival for either film on the ferrous alloy, and thus the effect of the biofilm, remain ambiguous.

1.6 Thesis Outline

As can be seen in the preceding sections, MIC is a highly complex problem that spans multiple fields of study and defies easy solutions. Because of its biological nature, the number of variables involved render laboratory models into only approximations of the real world phenomenon. Realizing these limitations, the work in this thesis restricts its focus on to one specific question regarding MIC: does the metal-binding characteristic of bacteria biofilms enhance the rate of corrosion when in the presence of iron sulfide corrosion products?

It had been hypothesized that metal ions bound in the EPS of a biofilm by anionic functional groups (e.g., carboxyl, phosphate, sulfate, glycerate, pyruvate, and succinate groups) can enhace the rate of corrosion of the underlying metal by shifting the standard potentials of the dissolution reaction [10]. Past studies involving abiotic gel analogues, however, have found no evidence for this phenomenon in an aerated solution on mild low-carbon steel [43]. Roe et al. applied agarose (a gel that does not bind metal ions) and calcium alginate (a gel that does bind metal ions) directly onto a mild steel coupon and measured the corrosion underneath the gels. They found no differences between them. I hypothesized, however, that the presence of an intervening iron sulfide film between the steel and gel will cause a difference to appear between the gels. Namely, I hypothesized that the metal-binding calcium

alginate will enhance corrosion while agarose will not. I tested this hypothesis in Chapter 2 using electrochemical techniques.

In Chapter 3, I detail the process of generating and validating the iron sulfide films that were used for the experiments in Chapter 2. Iron sulfides appear in a large variety of forms ranging from mackinawite (FeS_{1-x}) to pyrrhotite ($Fe_{1-x}S$) to pyrite (FeS_2). Each phase has its own crystal structure, chemical stability, and potential effect on corrosion. Iron sulfide films were grown on mild steel coupons and their composition and phase were identified through the use of x-ray diffraction (XRD), energy dispersive x-ray spectroscopy (EDX), and Raman spectroscopy.

In Chapter 4, I make both qualitative and quantitative comparisons between MIC and abiotic iron sulfide corrosion of the sort detailed in Chapter 3. Mild steel coupons were exposed to SRB containing media and allowed to corrode in an anaerobic environment. The corrosion damage to these coupons were then compared to iron sulfide corrosion using scanning electron microscopy (SEM). Additionally, SRB biofilms were grown on electrodes and their effect on corrosion were measured using the electrochemical techniques that were used in Chapter 2.

The last chapter summarizes the results of this work and proposes directions for future work.

Chapter 2

The Effect of Metal-Binding Biopolymer Gels on Corrosion

2.1 Introduction

There is a hypothesis in the literature that the metal-binding characteristic of bacteria biofilms may enhance the rate of corrosion [10]. However, experiments by Roe et al. [43] using abiotic gel analogues in place of biotic biofilms have found no evidence to support this. I seek to modify the approach used by Roe et al. in order to test a new hypothesis: Does the metal-binding characteristic of bacteria biofilms interact with iron sulfides in order to enhance the rate of corrosion?

In certain circumstances, the iron sulfide corrosion product generated in sulfurous environments, such as in the presence of sulfate-reducing bacteria (SRBs), may form a passivating film that protects the underlying steel from further corrosion. I hypothesize that the metal ions bound in the bacteria biofilm act to destabilize this passivating film, thus exposing the bare steel to further corrosion. Moreover, since iron sulfide is cathodic with respect to steel, a small localized disruption in the iron sulfide film may lead to a high rate of pitting corrosion due to the massive size disparity between the iron sulfide cathode and the steel anode. In place of a real biofilm, abiotic gel analogues were used: agarose, which does not bind metal ions, and calcium alginate, which does bind metal ions. Figure 2-1 illustrates this hypothesis.

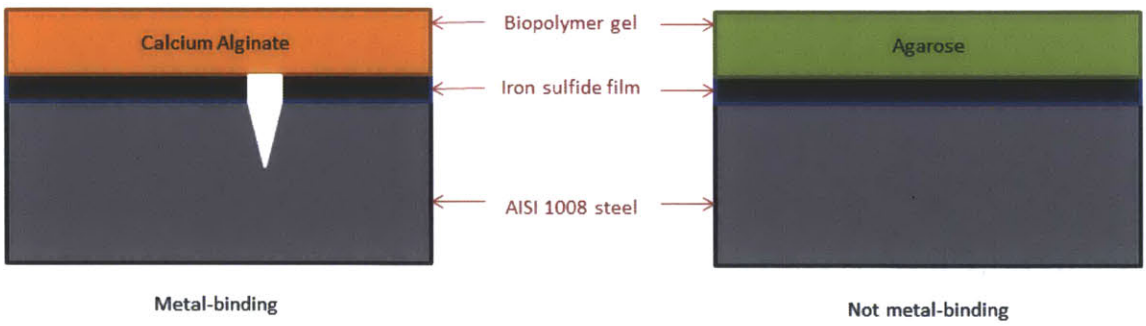

Figure 2-1: Schematic illustrating the effect that a metal-binding gel may have on a passivating iron sulfide film. The non-metal-binding agarose does not interact with the iron sulfide film, but the metal ions bound in the calcium alginate gel act to cause localized disruptions in the passivating iron sulfide film, exposing the underlying metal to the environment and inducing pitting corrosion.

2.2 Materials and Methods

Corrosion can be measured using a variety of techniques, but my preliminary approaches (Appendix A) showed that mass loss – in which the mass of a metal sample is measured before and after corrosion – lacked the precision required for rapid and small scale laboratory experiments. Instead, I opted to use potentiostatic techniques in which the voltage of the electrode is controlled and the resulting current measured. The following sections will cover the theory behind these techniques, the design of the electrochemical cells used, and then the gel corrosion experiments. It should be mentioned that these experiments were made possible due to John Rogosic, PhD candidate in the MIT Department of Materials Science and Engineering, and the Sadoway Group at MIT who generously lent us one of their potentiostats.

2.2.1 A primer on electrochemistry and the Tafel slopes

An electrochemical reaction is a chemical reaction that occurs at the interface of a conductive solid, the electrode, and an ionic solution, the electrolyte. These reactions are characterized by electron transfer between the electrode and the electrolyte; as such, these reactions are parameterized by the electrochemical potential $\bar{\mu}$ instead of the chemical potential μ in a typical chemical reaction. These electrochemical variables are defined below in equations 2.1 through 2.3. The symbols used are defined in Table 2.1.

Table 2.1: Definition of electrochemical variables.

Variable	Definitionl	Unit
$\bar{\mu}$	electrochemical potential	-
μ	chemical potential	-
E	electrostatic potential	volt
z	ionic valency	-
F	Faraday's Constant	Coulomb/mol
G	Gibbs free energy	Joules/mol
i	current	ampere
$\dot{m}$	reaction rate	gram/second
M	molecular mass	gram/mol

$$\bar{\mu} = \mu + zFE \tag{2.1}$$

$$\Delta G = -zFE \tag{2.2}$$

$$\dot{m} = i\,(M/Fz) \tag{2.3}$$

As can be seen in equation 2.2, the voltage of an electrochemical reaction is directly linked to the free energy of the reaction. Thus controlling the voltage an electrode will allow control of the reaction in general. By recording the current passing through the electrode, the rate of the reaction can be obtained through equation 2.3. The rate of a corrosion reaction, however, cannot be directly measured at equilibrium. Equilibrium is defined as the potential at which the anodic current becomes equal in magnitude to the cathodic current, rendering the net current zero (see Figure 1-4). This unmeasurable current is defined as the exchange current, i_0, while the anodic current is the rate at which the metal of the electrode is being corroded. While the exchange current cannot be directly measured, it can be indirectly determined by extrapolating from non-equilibrium reaction rates by manipulating the Butler-Volmer equation, which is defined below:

$$i = i_0 \left[e^{\left(\frac{K\eta}{RT}\right)} - e^{\left(\frac{-K\eta}{RT}\right)} \right] \tag{2.4}$$

where i is the measured current, K is a proportionality constant, R is the ideal gas constant, T is the temperature, and η is the overpotential defined by $E_{applied} - E_{equilibrium}$. The Butler-Volmer equation is the governing equation of electrode kinetics.

As can be seen in equation 2.4, at very high and very low overpotentials, one of the two exponential factors becomes negligible. At such overpotentials, the reaction is said to be in the Tafel regime. By rearranging and simplifying the remaining terms, the Tafel equation can be obtained:

$$\eta = a \pm b \cdot log(i) \tag{2.5}$$

where a and b are constants, with b known as the Tafel slope; in general, these constants will be different for the anodic and cathodic branches. Equation 2.5 indicates that the reaction kinetics in the Tafel regime will be linear in the $log(i)$ vs. η domain. This linearity allows the exchange current to be easily found schematically by following the slopes of the linear regime and extrapolating as demonstrated in Figure 2-2. Real Tafel plots, however, will not appear as neat as the example shown. At high enough overpotentials, the diffusion rate of species to and from the electrode surface will become the rate limiting step, causing the current to plateau. Moreover, the two Tafel slopes, the anodic and the cathodic slopes, will be unequal and may even change as different reactions become rate limiting. Nevertheless, obtaining the Tafel measurements was the simplest and most straightforward method to electrochemically determine the corrosion rate.

2.2.2 Electrochemical cell design

A standard three-electrode cell was used for all the electrochemical experiments. Figure 2-3 is a schematic of the setup. The working electrode (WE) consists of the material being studied, the reference electrode (RE) consists of a material that maintains a constant potential at all times, and the counter electrode (CE) is an inert conductor that is able to support high currents without reacting with the electrolyte. The voltage between the working electrode and the reference electrode is controlled by the potentiostat, and the current between the working electrode and the counter electrode is measured. If voltage and current were not uncoupled in this manner, then an accurate reading cannot be taken. If the reference and counter electrode were combined, then the movement of current though this combined electrode would fuel an electrochemical reaction at this electrode, altering its potential.

The working electrode (Figure 2-4A) used consists of mild steel wires coated with PVC and encased in epoxy on one end. The steel wire used was 0.062 inch diameter AISI 1008 carbon steel, soft tempered and PVC coated (McMaster-Carr). AISI 1008 is a carbon steel that is used for bulk structural applications due to its availability and its low cost. As such, it was chosen to be the representative material upon which MIC was tested. Table 2.2 lists the elemental composition of AISI 1008.

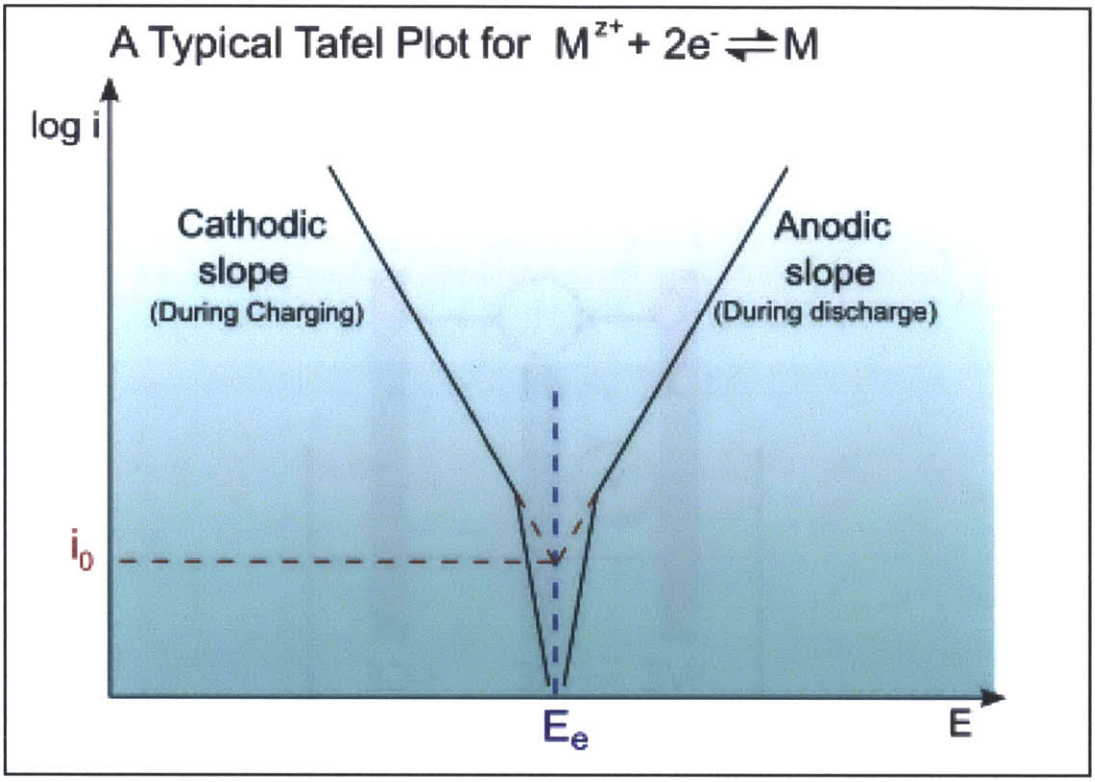

Figure 2-2: An example of a typical Tafel plot. The exchange current i_0 can be found at the intersection of the two linear regimes. Image is from [49]

.

Table 2.2: Composition of AISI 1008 carbon steel [50].

Element	**Composition (wt%)**
Carbon (C)	0.10 (max)
Manganese (Mn)	0.30-0.50
Phosphorus (P)	0.04 (max)
Sulfur (S)	0.05 (max)
Iron (Fe)	balance

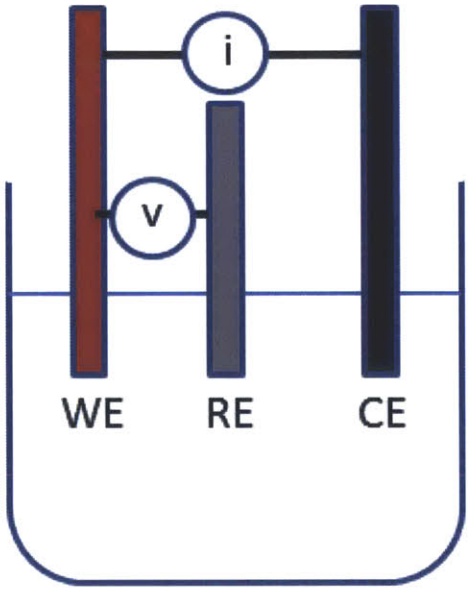

Figure 2-3: A schematic of a standard three electrode cell. The working electrode (WE) is the material being studied, the reference electrode (RE) is a material that maintains a constant potential at all times, and the counter electrode (CE) is an inert conductor that is able to support high current without reacting with the electrolyte. In this work, the WE was AISI 1008 carbon steel, the RE was 99.9% pure hardened silver, and the CE was graphite.

To make a single working electrode, an approximate 8 inch section of wire was cut from a larger wire spool of 245 foot length. This wire was then placed, end first, into a 1.8 mL Corning cryogenic vial. Buehler EpoKwick epoxy was then mixed according to the included instructions: 20 mL resin and 4 mL hardener were mixed together and stirred for at least 1 minute. Approximately 1 mL of epoxy was placed into the cryogenic vial with the wire. Typically, these electrodes would be made in batches of 24 replicates to make the most use of a single mixture of the epoxy. The epoxy was allowed to harden for 24 hours, after which the electrodes were brought to the machine shop. Using a band saw, the bottom of the cryogenic vial was cut off at a height of approximately 1 cm. This cut exposed a cross section of the metal wire. This cut end is then polished on a grinding wheel using a succession of 120, 300, and 500 grit abrasive discs. When done, the newly polished electrode faces were cleaned using ethanol and Kimwipes. These electrodes were then stored in a plastic bag exposed to air for future use.

Instead of a reference electrode, a pseudo-reference electrode in the form of silver wire was used. Unlike a reference electrode, a pseudo-reference electrode is not guaranteed to maintain a known potential in all environments. However, in a given environment it will maintain a constant potential that may be determined if measured against a real reference electrode. A pseudo-reference electrode was chosen because of its low cost and low maintenance in contrast to a reference electrode, a single one of which may cost several hundred dollars. For our experiments, 1 mm diameter 99.9% pure hardened silver wire (Alfa Aesar) was used. For each experiment, approximately 10 cm was cut off and used without further treatment.

The counter electrode used was a carbon brush (McMaster-Carr). This brush consists of a block of graphite measuring 1 inch in height by 0.75 inches wide by 0.25 inches thick. A 2 inch long copper shunt with a steel terminal came preinstalled in the brush. This terminal was trimmed off and the copper shunt lengthened by twining the existing shunt with an 8 inch long length of copper wire. The copper wire was joined to the copper shunt using the EpoKwick epoxy. Each counter electrode was used for a single experiment each. Typically, a coil of platinum wire would be the preferred counter electrode, but such a tool was cost prohibitive; graphite serves as a lower cost alternative.

These three electrodes were combined by passing them through a size 10 $^{1}/_{2}$ black butyl rubber stopper (VWR) as can be seen in Figure 2-4B. Three 61 gauge (0.991 mm) diameter holes were drilled through this butyl rubber stopper for the electrodes to pass through. These holes were coated with vacuum grease to both enable easy pass though of the larger electrode wires and to ensure as good an airtight seal as possible. Immediately before passing through the working electrode,

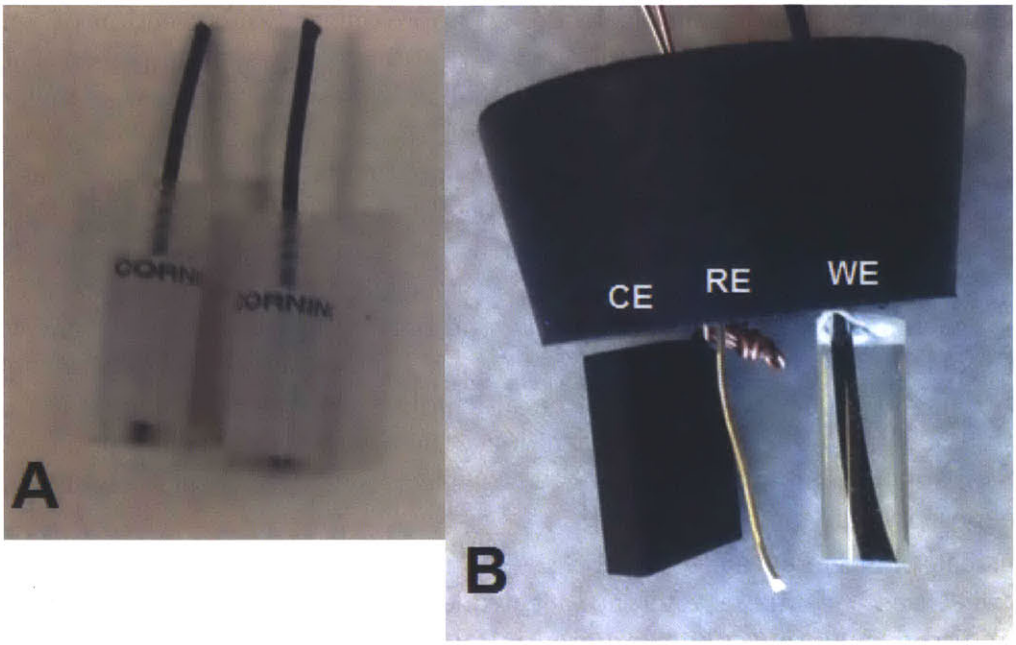

Figure 2-4: The three electrodes used in the experiments. A) The working electrodes. B) The three electrodes were assembled by passing them through a butyl rubber stopper.

the polished metal face was polished using 1500 grit sandpaper and cleaned with ethanol to remove any oxide films that may have grown while it was in storage. It often required use of pliers to force the electrode wires through the rubber stopper. Both the working and counter electrodes were raised as far as possible. The reference electrode was placed such that it extended as far as the other two electrodes. On the top of the rubber stopper, excess steel wire and copper wire was trimmed off to allow easy handling. Approximately 5 cm lengths of each wire were left to connect the potentiostat's leads. The PVC was stripped from the last half inch length of the working electrode's steel wire using a wire stripper. These stoppers were assembled only immediately before conducting an experiment.

The electrolyte in all experiments consisted of deoxygenated deionized water containing 1 M sodium sulfate adjusted to a pH of 3 using sulfuric acid. See Section 3.2 for more details. The electrolyte was made in 500 mL batches. For each batch, 71 grams (0.5 mol) of sodium sulfate was added to 500 mL of deionized water in a glass bottle and vigorously stirred using a magnetic stir bar until the solution turned clear and no solids could be seen. To this, 26.8 μL of pure sulfuric acid was added to

Table 2.3: Conditions which were investigated in the electrochemical experiments

Condition	Predicted Corrosion Behavior
bare steel	control
agarose	same as or slightly less corrosive than control
calcium alginate	same as or slightly less corrosive than control
iron sulfide	less corrosive than control
iron sulfide + agarose	less corrosive than control
iron sulfide + calcium alginate	more corrosive than control

reduce the pH to 3. The solution was deoxygenated by bubbling nitrogen though it. A clean rubber hose was connected to a nitrogen source and the other end inserted into the solution; the opening of the bottle was sealed loosely with aluminum foil to allow displaced oxygen to vent. After 1 hour of nitrogen bubbling, the bottle was quickly capped and transferred to a Shel Lab BacBASIC anaerobic glovebox. Once inside the glovebox, the cap on the bottle was loosened and the solution allowed to sit for 24 hours to let any remaining oxygen in solution to diffuse out. The atmosphere inside the glovebox consisted of 5% carbon dioxide, 5% hydrogen, and 90% nitrogen.

To construct a completed cell, the butyl rubber stopper containing the electrodes and a 4 oz widemouth bottle (VWR), 58 mm cap size, was passed into the glovebox. Prior to this, the working electrode on these stoppers would have already been functionalized by the appropriate gel and/or iron sulfide as needed. Refer to Section 2.2.3 for the procedure for functionalizing the working electrode. For each cell, 80 mL of the electrolyte solution was poured into the 4 oz glass jar. The rubber stopper was then inserted into the jar and pressed tightly to ensure a good fit. Two rubber bands were used to hold the stopper down to ensure the stopper stayed plugged into the jar at all times. This sealed jar was then passed out of the glovebox and brought to the potentiostat to begin the experiment. This portion of the experiment is described in Section 2.2.4.

2.2.3 The addition of gels and/or iron sulfide

Table 2.3 summarizes the conditions that were tested and the predicted behavior. Experiments involving only the bare steel required no further preparation beyond those described above, but all other cases required the addition of either iron sulfide and/or a biopolymer gel.

In order to develop the iron sulfide film, a sulfide solution was prepared by adding, inside the glovebox, 134 mg of sodium sulfide nonahydrate to 100 mL of

the electrolyte solution described in Section 2.2.2. This quantity of sodium sulfide nonahydrate and electrolyte solution corresponded to a sulfide concentration of approximately 100 ppm. 80 mL of this 100 ppm sulfide solution was then added to the 4 oz glass jar and a rubber stopper containing the electrodes, prepared as described in Section 2.2.2, was inserted. This assembled cell was then brought to the potentiostat and subjected to a single pass of the anodic polarization as described in Section 2.2.4. The sort of polarization effectively plates the working electrode's surface with a black iron sulfide film. Following this polarization, the entire cell was brought back into the glovebox. While inside the glovebox, the working electrode was extracted and washed using the electrolyte solution. A gel would then be added, if needed. This electrode was then inserted into a new rubber stopper assembly and the procedure follows that as described in the previous section.

To prepare the agarose gel films, 1.5 g of agarose powder was added to 50 mL of deionized water inside a glass 100 mL beaker. This corresponds to a 3 wt% agarose gel. This solution was then heated inside a microwave in 10 second increments until the solution turned clear. Approximately 1 mL of this agarose solution was then added to the working electrode and allowed to cool until the gel hardened. The gel would harden into a hemisphere approximately 4 mm thick at the thickest point. If no iron sulfide was required, then this gel would have been added directly to a fresh working electrode. If iron sulfide was required, then the procedure in the previous paragraph was followed first. The excess agarose was left to harden and then disposed of, since reheating it may change its water content and thus its density.

To prepare the calcium alginate film, 1.5 g of sodium alginate powder was added to 50 mL of deionized water inside a glass 100 mL bottle. This corresponds to a 3 wt% sodium alginate gel. This solution was then stirred using a magnetic stir bar until the solution turned viscous and uniform in color. The solution appeared slightly tan to light brown. This sodium alginate solution does not degrade with time and thus can be stored at room temperature, unlike the agarose gel. When needed, this sodium alginate solution was heated to 50°C. Approximately 1 mL of this heated sodium alginate solution was then added to the working electrode. Following this, an excess amount of 1 M calcium chloride solution was added to the sodium alginate to convert it to calcium alginate. The gel was then allowed to cool. The shrinkage caused by the cooling allowed the gel to grip onto the edges of the working electrode, enhancing the gel's adhesion. In the absence of this effect, calcium alginate lacked the adhesion to attach strongly to the electrode's surface. If no iron sulfide was required, then this gel would have been added directly to a fresh working electrode. If iron sulfide was required, then the procedure described above must be followed first. The excess sodium alginate solution was capped and stored at room temperature for future use.

2.2.4 Electrochemical measurements

A PARSTAT 2273 (Princeton Applied Research) potentiostat was used for all the electrochemical experiments. Electrochemistry PowerSuite (Princeton Applied Research) was the software used. These were generously loaned to me by John Rogosic, PhD candidate in DMSE, and the Sadoway lab. The potentiostat has three alligator clamp leads clearly marked as WE, RE, and CE for the working electrode, reference electrode, and the counter electrode, respectively. Once connected to the potentiostat, all cells were subjected to the same polarization program:

start loop
wait 5 minutes
cathodic polarization
wait 5 minutes
anodic polarization
end loop after 10 interations

For cathodic polarization, the voltage was decreased from 0 to -250 mV vs the open circuit voltage (OCV) at a rate of 0.1 mV/second. Such a slow ramp rate was used to ensure that the working electrode was at pseudo-equilibrium conditions at all times. For anodic polarization, the voltage was increased from 0 to +250 mV vs OCV at a rate of 0.1 mV/second. The 5 minute delays between scans was to ensure that the effects of one polarization did not substantially affect the next. The device measured the current that passed through the circuit formed by the working and counter electrodes, while the applied voltage was between the working and reference electrodes. All data were automatically recorded in text files and analyzed using Matlab.

2.2.5 Data analysis

For a given working electrode, 10 separate sets of measurements were made using the program shown in Section 2.2.4. The first set of of measurements, i.e., the first cathodic polarization and the first anodic polarization data, were uniformly neglected. These measurements were often vastly different than the rest of the data (see Appendix B). This difference was attributed to the electronics and the electrochemical cell acclimatizing itself. The rest of the data was analyzed and is discussed next.

For a single set of data, either cathodic or anodic, the measured voltage and current were imported into Matlab as two separate vectors containing 2500 data points each. The first 10%, or 250, data points were omitted from further analysis

Table 2.4: Electrochemical experimental results (error is ± one standard deviation).

Condition	Number of Experiments	Mean Exchange Current Density ($\mu A/cm^2$)
bare steel	5	37.62 ± 3.08
agarose	4	13.67 ± 2.53
calcium alginate	4	49.03 ± 2.18
iron sulfide	2	45.55 ± 3.42
iron sulfide with agarose	3	14.98 ± 1.87
iron sulfide with calcium alginate	2	59.28 ± 2.73

since these data points are near the OCV and thus not part of the Tafel regime. The recorded current data, i, was converted to $log_{10}(abs(i))$ to fit the form of the Tafel equation 2.5. This $log_{10}(abs(i))$ was plotted against the applied voltage. A window of 500 data points was scanned across this graph; within this window, least square regression was used to find the best fit slope. This slope has the form of $\frac{log_{10}(abs(i))}{E}$. This slope was recorded to a vector; with a window size of 500 data points and 2250 remaining data points, 1750 best fit slopes were recorded in this vector. These slopes were then rounded to the nearest integer, and the most common slope was used to represent the Tafel slope of the measured data as a whole. This process was done for both the cathodic polarization and the anodic polarization data. Lines using the calculated Tafel slopes were then fit using least square error to the region containing the most common slope in their respective data, and the intersection of these two Tafel lines gave the magnitude of the exchange current. Figure 2-5 is a graphical example of this algorithm.

2.3 Results and Discussion

Table 2.4 and Figure 2-6 displays the compliation of all the electrochemical data that was measured from these experiments. For each working electrode that was made, 10 replicate measurements were made and 9 of these were used. The first measurement on each working electrode was discarded, as previously discussed. The "number of experiments" column in Table 2.4 refers to the total number of electrodes that were made. Of course, more electrodes were made for earlier iterations of this experiments, but only those that conform to the procedures outlined in this thesis are shown. Table 2.5 shows the statistical tests for significance conducted on this

Table 2.5: Statistical signficance for the measured corrosion rates was tested for using t-tests with $\alpha = 0.05$. Entries are the p-values obtained from a two-tailed t-test comparing the measured mean corrosion rates. These means are for all experiments of the same type. Italicized entries indicate no statistically significant differences between measured corrosion rates. All other entries indicate statistically significant differences among experiments.

	Agarose	**Calcium Alginate**	**Iron Sulfide**	**Iron Sulfide + Agarose**	**Iron Sulfide + Calcium Alginate**
Steel	0.00195	0.01503	0.03485	0.00021	0.00065
Agarose	-	0.00133	0.00314	*0.67512*	0.00112
Calcium Alginate	-	-	*0.32226*	0.00004	0.00249
Iron Sulfide	-	-	-	0.00016	0.02043
Iron Sulfide + Agarose	-	-	-	-	0.00002

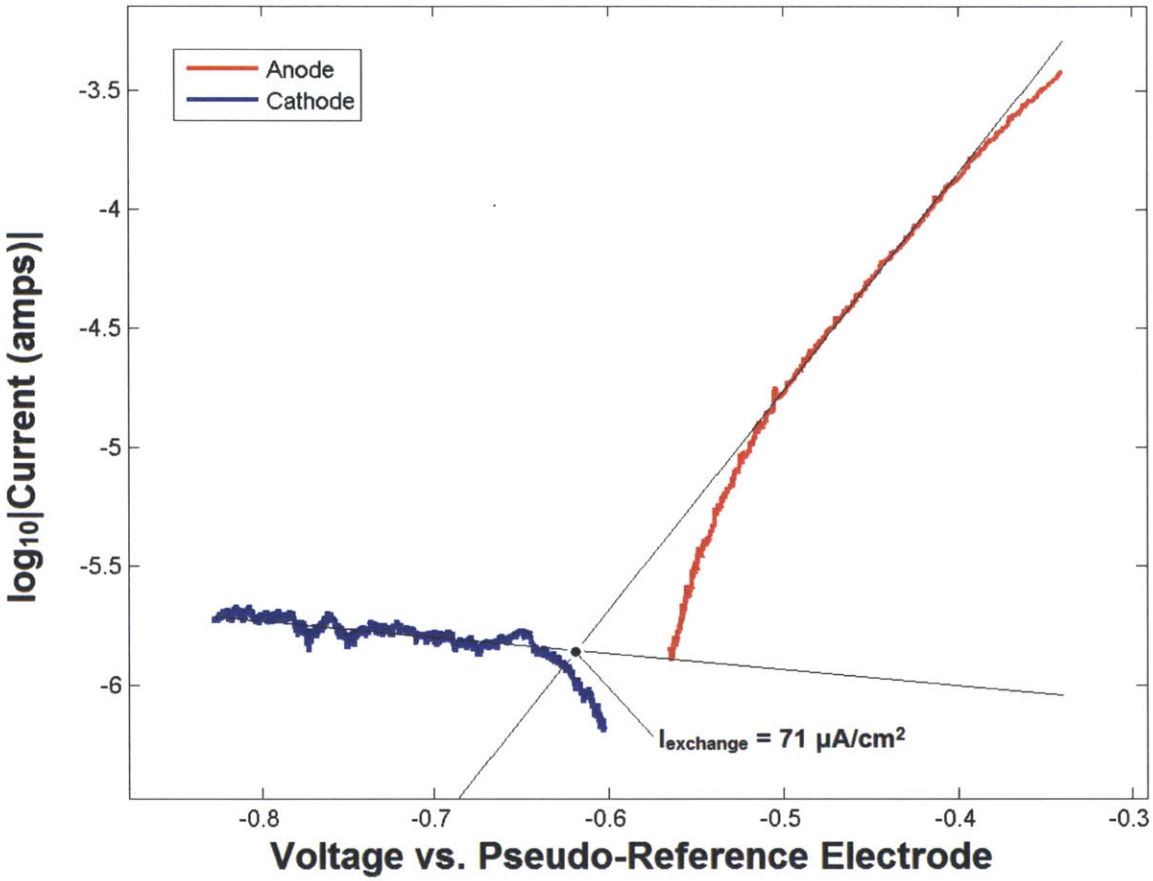

Figure 2-5: Example electrochemical response measured for bare steel corroding at neutral pH in oxygenated 3.5wt% NaCl. The exchange current is found where the two fitted slope lines intersect; in this case, it corresponds to an exchange current of 71.01 $\mu A/cm^2$. The literature value for the exchange current in these conditions is approximately 75 $\mu A/cm^2$ [51].

data.

2.3.1 Agarose vs. Calcium alginate

As can be seen from Figure 2-7 and Table 2.5, the corrosion rates of the agarose and the calcium alginate electrodes are not equal. Calcium alginate clearly enhanced the corrosion rate, and agarose decreased it. This is contrary to my predictions in Table 2.3 and to the results of Roe et al. in [43]. This does, however, support the hypothesis

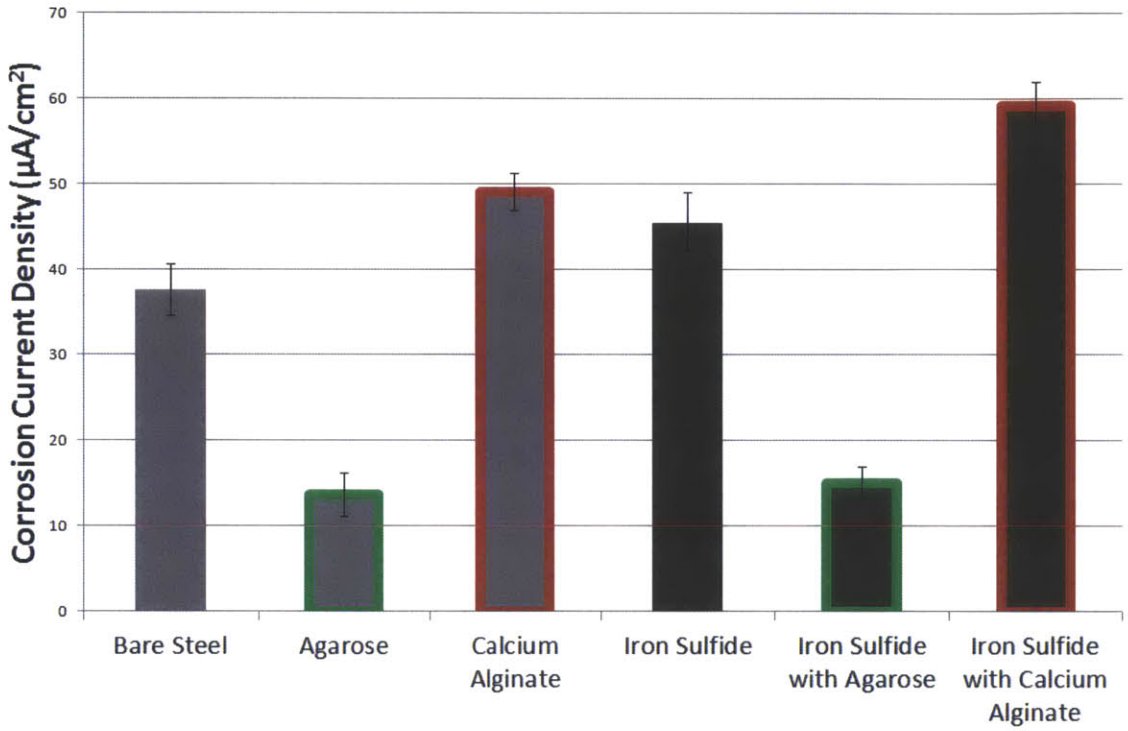

Figure 2-6: Compiled data for the electrochemical experiments. Error bars shown are ± one standard deviation. Each bar has been colored coded for convenience: grey fill color indicates a steel substrate; bronze fill color indicates an iron sulfide film substrate; green outline color indicates an agarose gel coating; red outline color indicates a calcium alginate gel coating; and no outline color indicates no gel coating.

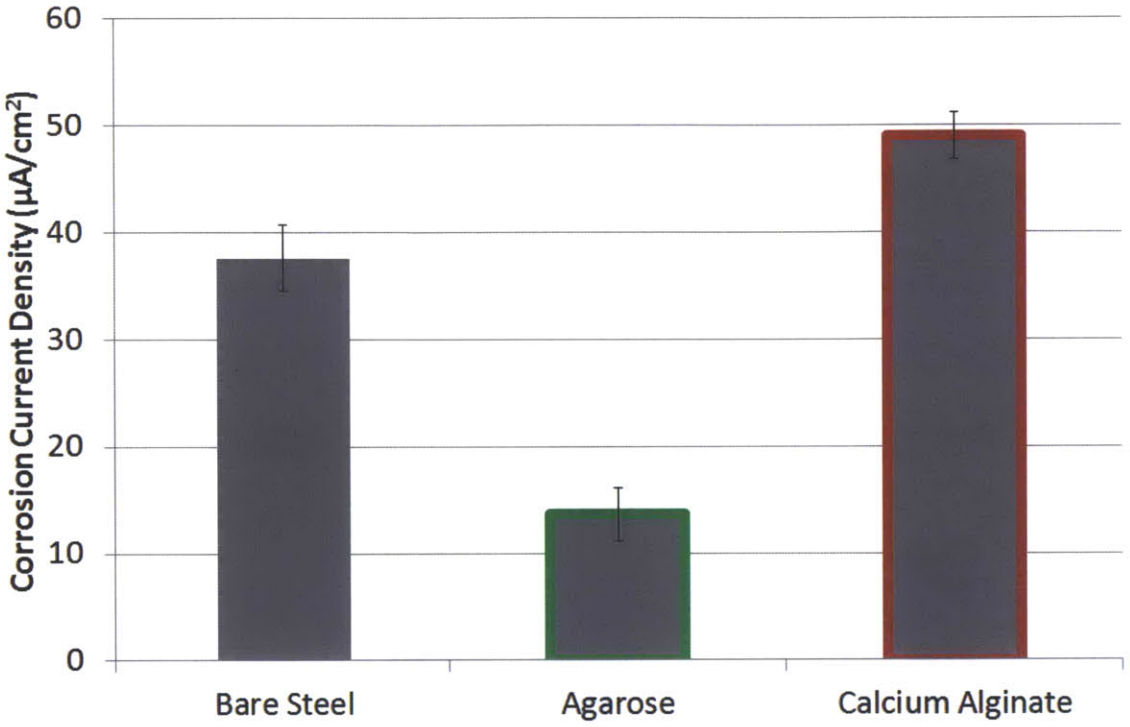

Figure 2-7: This is a subsection of Figure 2-6 shown here for convenience.

of Beech et al. in [10] that metal binding biofilms enhance the rate of corrosion. This discrepency with Roe's work may be explained by the differences between our experimental setup. In Roe's experiments, spots of calcium alginate and agarose were placed onto a small section of a larger metal surface, and the current density under the gel was directly measured using a scanning vibrating electrode. This surface was submerged in an oxygenated salt solution. The corrosion reaction was allowed to occur naturally at an equilibrium rate. In contrast, my system was deoxygenated and the electrode to which the gel was attached was externally controlled by the potentiostat.

Therefore it is quite possible that Roe et al. did not detect any difference between either gel because the rate of their corrosion reaction was being limited by some other reaction, namely the rate of oxygen reduction on the rest of the exposed metal surface. Since the anodic current must equal the cathodic current at equilibrium, a slow cathodic reaction will limit the rate of corrosion at the anode under the gel. This is further supported by Roe et al. not finding any differences in the rate of corrosion between different densities of gels as well – not even an order of magnitude

decrease in gel density, from 30 g/m^2 to 3 g/m^2, caused a noticeable change in their measured rate of corrosion.

The experiment setup used in this thesis faced no such limitations. Since the working electrode was externally controlled by the potentiostat, it could be made to perform as purely an anode or a cathode in isolation from the other half of the corrosion reaction. When the working electrode was anodically polarized, the cathodic reaction took place solely on the counter electrode. The same is true in the reverse case: when cathodically polarized, the working electrode acted as an anode. In either case, the counter electrode was guaranteed to not be the rate limiting factor due to its large size relative to the working electrode. The steel wire embedded in the working electrode has a diameter of only 1.575 mm, while the graphite brush had at least 645 mm^2 of surface area submerged in all cases – likely more than that due to the surface roughness and porosity of the graphite. In short, the counter electrode, and therefore the cathodic reaction, could not be the rate limiting factor in the setup used here during anodic polarization.

Roe et al. offered two possible mechanisms for calcium alginate's corrosion rate enhancing effect. First, it may be that bound ferrous ions could be oxidized more rapidly than the soluble hydrated ions, allowing the gel to act as a catalyst. Second, it may be that by binding metal ions the gel is removing a reaction product and, by the law of mass action, promoting further corrosion. Beech et al. suggested that metal-binding biofilms – and by extension the gels that mimic them – may have affinity for ions in oxidation states that would not occur normally, such as Fe^{3+} in non-acidic conditions [10]. By stabilizing and promoting the existence of these ions, the equilibrium potential of the corrosion reaction can be substantially shifted. Unfortunately, the alginic acid functional group in calcium alginate has affinity for divalent ions, which is the normal oxidation state for iron in most conditions, rendering Beech's hypothesis invalid.

Another possible mechanism that has not been suggested is that the buildup of the positive charges within the calcium alginate gel may aid in destabilizing the electrical double layer that naturally forms on an electrode. Since the working electrode is anodically polarized during corrosion, electrons are actively being removed by the applied voltage of the potentiostat. This causes a buildup of positive charges directly below the metal surface; this positive charge, in turn, causes negative ions to become strongly bound to the metal surface in what is known as the Stern or Helmholtz layer. This layer is typically no thicker than a single atom. This double layer of charges create a capacitance that creates impedance in the circuit – since voltage is controlled and constant, higher impedance results in lower current which through equation 2.3 means a lower corrosion rate. The presence of positive charges in the calcium alginate

may destabilize this double layer by providing electrostatic attraction away from the metal surface for the bound negative ions. This is a personal hypothesis – it may already exist in the literature, but I am not aware of it. In order to test for this effect, electrochemical impedance spectroscopy (EIS) would be required. EIS applies a sinusoidal voltage to the working electrode and records both the magnitude and phase of the resulting current; by sweeping across a wide range of frequencies, insight into the capacitive nature of the electrical double layer can be obtained.

Unlike the case of calcium alginate, there is a decrease in the corrosion rate when agarose is applied to the working electrode. This is likely due to diffusion-limiting effects, since the gel presents a physical barrier to all chemical species without presenting any other effects like calcium alginate does. Again, EIS could provide further insight into this mechanism.

2.3.2 Corrosion with iron sulfide

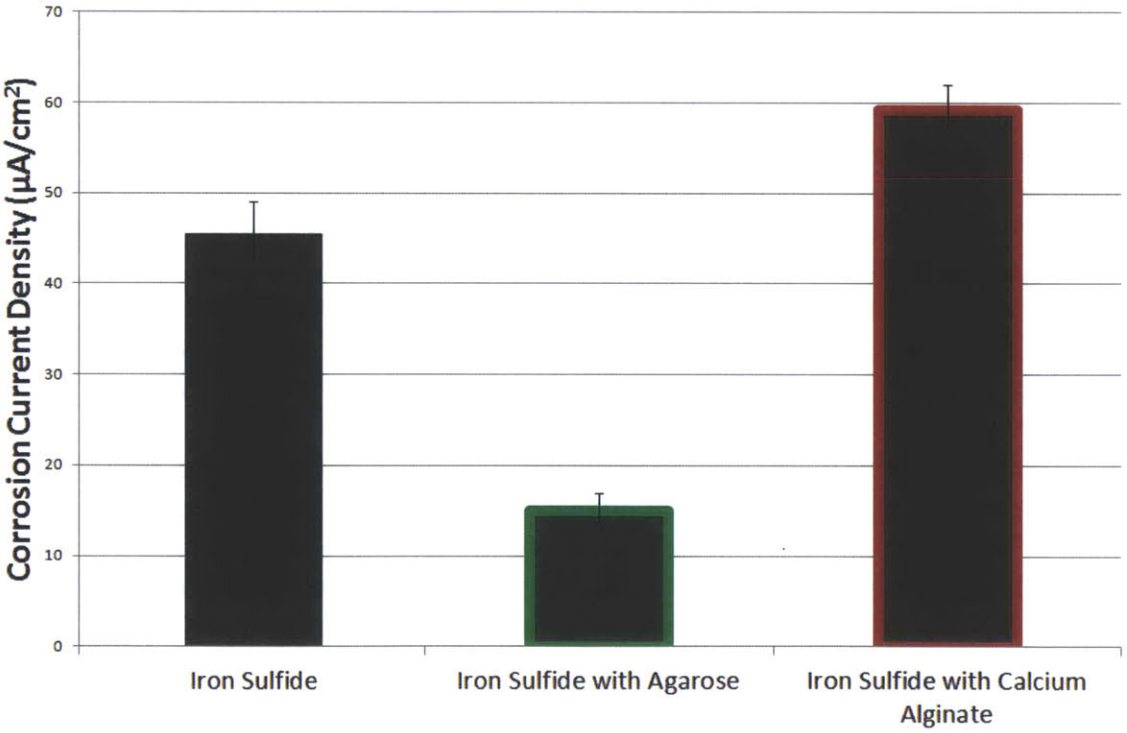

Figure 2-8: This is a subsection of Figure 2-6 shown here for convenience.

The original hypothesis posits that an iron sulfide film would be protective of the

underlying steel by passivating the surface. However, the data presented in Figure 2-6 indicate otherwise. It is possible that the form of iron sulfide generated in this experiment was not the protective kind. To be protective, the generated iron sulfide would need to be both stable and to provide total coverage of the steel surface – at least one of these two conditions were not met in this case. This shortcoming in experimental design was due to a last minute change in the procedures. Despite stable films being formed with ease on mild steel coupons as described in Chapter 3, these same films failed to develop on the working electrodes. It is most likely due to the size difference between the exposed steel on the working electrodes and the steel coupons. When more of the wire was stripped off the tail of the working electrode, that area formed a sulfide film. Because of this limitation, the iron sulfides on the working electrodes were made by actively polarizing the electrode in a 100 ppm sulfide solution. Since 100 ppm formed a stable film on the coupons, it was chosen as the concentration to use here. However, the results indicate that the formed iron sulfide was not passivating; rather it enhanced corrosion. Since iron sulfide is cathodic toward steel, this is to be expected (see Figure 3-1).

The combination of iron sulfide and calcium alginate may be a linear combination of each element's ability to enhance corrosion and not due to an interplay between these two elements as originally hypothesized, but there is little evidence for or against this. The relative increase in corrosion rate caused by the addition of calcium alginate in both cases (on the steel substrate and on the iron sulfide film substrate) was approximately 1.30. This suggests, although weakly, that calcium alginate plays a similar role in both cases and that it is not accessing a unique interaction with the iron sulfide.

The combination between iron sulfide and agarose, however, is more interesting. It seems that agarose's ability to lower the corrosion rate overwhelmed the iron sulfide's ability to enhance it. It has been suggested in the literature that bacteria biofilms may aid in corrosion prevention by helping stabilize a passivating iron sulfide film. It is possible that this is the effect being seen here. Future experiments that could explore this proposed mechanism are discussed in Section 5.3.

2.4 Summary

Electrochemical experiments were conducted on AISI 1008 carbon steel wire working electrodes funtionalized with an iron sulfide film and/or an artificial biogel coating in order to investigate the effect that these elements have on the corrosion rate of steel. Calcium alginate gel was used to simulate the metal-binding characteristic of microbial biofilms, and agarose was used as a control gel which does not bind metal

ions.

Calcium alginate was found to enhance the corrosion rate, and agarose decreased it. This finding is contradictory to existing literature. This discrepency could be explained by a difference in experimental design. Additionally, iron sulfide was found to enhance the rate of corrosion. Neither gel appeared to interact strongly with an underlying iron sulfide film.

Chapter 3

Iron Sulfide Film Development and Validation

3.1 Introduction

In an MIC event involving SRB, various iron sulfide corrosion products may form. The exact composition and distribution of these corrosion products can be difficult to predict, since it is highly dependent upon the specific environmental conditions present. Table 3.1 lists the common iron sulfide corrosion products that can be found at sites of MIC corrosion. Each of these products have a different implication on the rate of corrosion. In [48], King et al. formed the various iron sulfide corrosion products as aqueous precipitates by reacting various sulfide and iron containing chemicals to form a corrosive solution. Samples of mild steel were then placed in these corrosive solutions and allowed to corrode (Figure 3-1).

The iron sulfides produced by King et al. were aqueous precipitate that were initially suspended in solution and allowed to settle on the mild steel samples. The results of that experiment, then, would not apply to an iron sulfide film that was grown on the steel sample itself. A film, in contrast to loose precipitate, would be

Table 3.1: Common iron sulfide corrosion products [48].

Product	Mackinawite	Greigite	Smythite	Pyrrhotite	Pyrite	Marcasite
Chemical Formula	FeS_{1-x}	Fe_3S_4	Fe_3S_4	$Fe_{1-x}S$	FeS_2	FeS_2
Crystal Structure	Tetragonal	Cubic	Hexagonal	Variable	Cubic	Orthorhombric

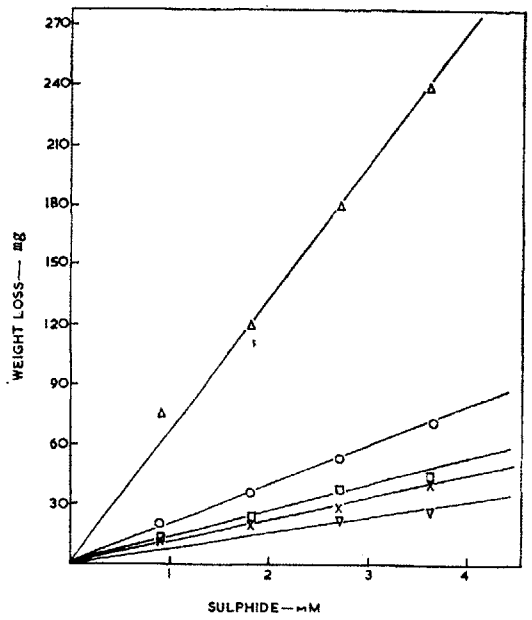

Figure 3-1: Comparison of the effect of various iron sulfide precipitates on the rate of corrosion. Iron sulfides were formed as aqueous precipitates by reacting various sulfide and iron containing chemicals [48].

chemically bonded to the underlying steel and may form a passivating film, preventing further corrosion from occurring. Regardless, an iron sulfide film is an integral element of the hypothesis that was tested in Chapter 2. This chapter will focus on the development of these iron sulfide films on mild steel coupons and the subsequent validation conducted to determine their phase and composition.

3.2 Methods and Materials

All iron sulfide films were grown on mild steel coupons. AISI 1008 mild carbon steel bars were obtained from McMaster-Carr (see Table 2.2 for the elemental composition of AISI 1008 steel). These bars measured 1.5875 mm thick by 1 cm wide by 1.83 m long (1/16" thick by 1" wide by 6' long) and were cold rolled. Using a bandsaw, these bars were cut into 15 mm sections. These mild steel coupons measured 1.5875mm (1/16") thick by 25.4mm (1") wide by 15 mm long. The cut edges were filed down to remove the burrs, and both faces were hand polished using a succession of 120, 300, and 500 grit sandpaper. Immediately prior to use, these coupons were rinsed in ethanol and dried using kimwipes. Excess coupons were stored in a plastic bag at room temperature exposed to air; no special precautions were taken in their storage.

Following several failed attempts to develop an iron sulfide film using only an aqueous sodium sulfide nonahydrate ($Na_2S \cdot 9H_2O$) solution, even at concentrations of 1 M, the solution used by Davoodi et al. was adopted [52]. The sulfide solution consisted of 1 M sodium sulfate adjusted to a pH of 3 using pure sulfuric acid. The full procedure for making this solution was detailed in 2.2.2, but it will be replicated here for convenience. The solution was made in 500 mL batches. For each batch, 71 grams (0.5 mol) of sodium sulfate was added to 500 mL of deionized water in a glass bottle and vigorously stirred using a magnetic stir bar until the solution turned clear and no solids could be seen. To this, 26.8 μL of pure sulfuric acid was added to reduce the pH to 3. The solution was deoxygenated by bubbling nitrogen though it. A clean rubber hose was connected to a nitrogen source and the other end inserted into the solution; the opening of the bottle was sealed loosely with aluminum foil to allow displaced oxygen to vent. After 1 hour of nitrogen bubbling, the bottle was quickly capped and transferred to a Shel Lab BacBASIC anaerobic glovebox. Once inside the glovebox, the cap on the bottle was loosened and the solution allowed to sit for 24 hours to let any remaining oxygen in solution to diffuse out. The atmosphere inside the glovebox consisted of 5% carbon dioxide, 5% hydrogen, and 90% nitrogen.

All the following procedures were conducted inside the anaerobic glovebox unless otherwise stated. The glovebox was needed in order to both contain the noxious hydrogen sulfide gas that formed when sodium sulfide and water reacted, and to

Table 3.2: Conditions and results of the effect that various sulfide concentrations have on mild steel.

Concentration	Amount of $Na_2S \cdot 9H_2O$ per 100mL of the sulfate solution	Appearance after 24 hours
0 ppm (control)	0 mg	silvery in color, appears unchanged
10 ppm	13.4 mg	black corrosion product, patchy, parts of the metal is still exposed
50 ppm	67 mg	black corrosion product, total coverage of the metal
100 ppm	134 mg	gold corrosion product, shiny, total coverage of the metal
500 ppm	670 mg	silvery in color, appears unchanged
1000 ppm	1340 mg	silvery in color, appears unchanged
5000 ppm	6700 mg	silvery in color, appears unchanged

protect the corroding steel coupons from oxidizing and forming corrosion products that were not iron sulfides. This sulfate solution was divided into 100 mL quantities, and a varying amount of sodium sulfide nonahydrate was added to created a range of sulfide concentrations. Table 3.2 lists the amounts used and the corrosion products observed. 10 mL of these sulfide solutions were placed in 20 mL scintillation vials along with a single polished coupon. These vials were then capped and stored on their sides so as to minimize any effect a gravity induced concentration gradient would have. Additionally, when stored on their sides the steel coupons made contact with the vial only along the edge of the coupon, allowing both faces of the coupon to be exposed.

As can be seen from Figure 3-2, some form of corrosion product formed on these steel coupons within 24 hours. Although no visible corrosion products formed in the 500 ppm, 1000 ppm, and 5000 ppm sulfide solutions, these coupons did turn gold after 7 days, as can be seen in Figure 3-4. There appeared to be some sort of phase transition which occurs around the 100 ppm concentration, with lower concentrations creating a black corrosion product while higher concentrations creating a golden product. Moreover, the black corrosion product was loosely bound to the steel and

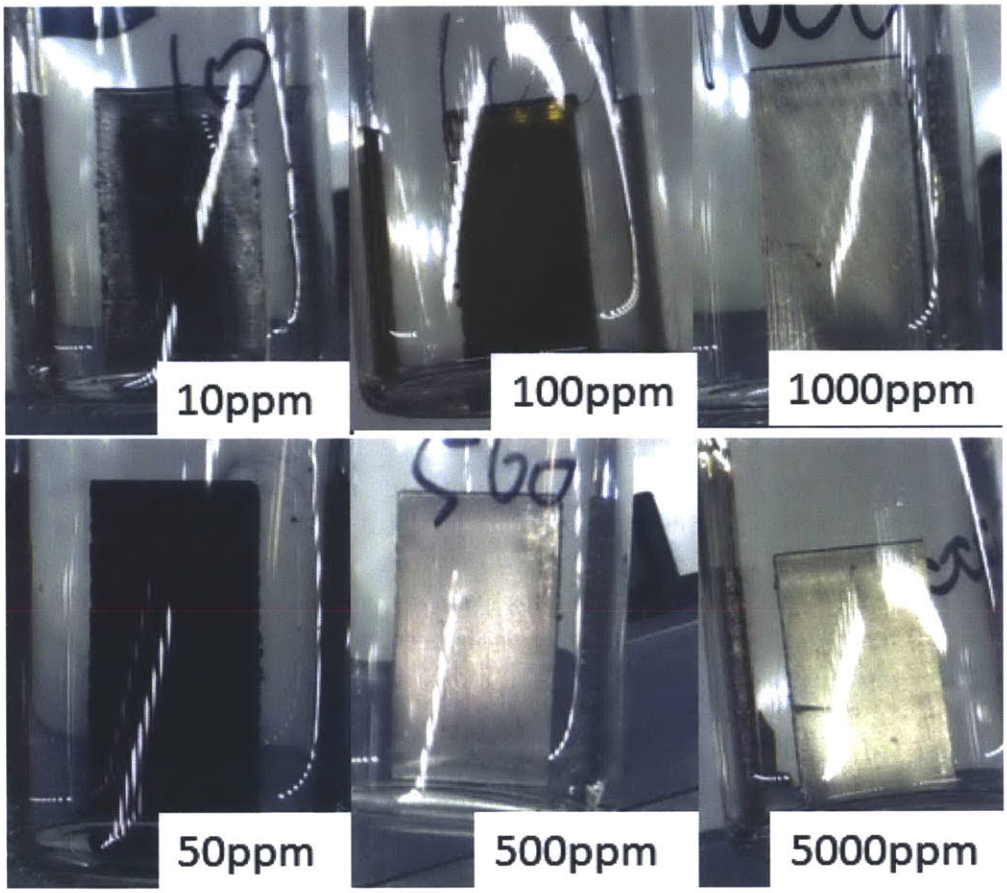

Figure 3-2: These coupons had been submerged in the sulfide solution for 24 hours at the time these images were taken. The 10 ppm coupon exhibits a patchy, black corrosion product. The 50 ppm exhibits a total coverage by the black corrosion product. The 100 ppm exhibits a deep gold corrosion product. The 500 ppm, 1000 ppm, and 5000 ppm exhibited no visible corrosion products.

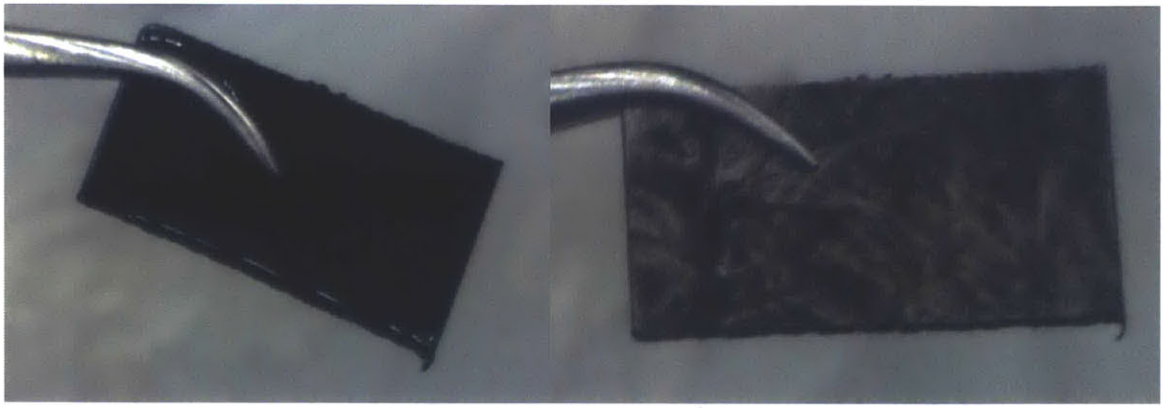

Figure 3-3: The coupon shown here is from the 50 ppm sulfide solution. The black corrosion product is loose and can be easily removed.

could be easily wiped off (Figure 3-3), while the golden corrosion product could not be removed. Figure 3-5 is an image of untreated steel, the 50 ppm coupon, and the 100 ppm coupon taken at 90x magnification using differential interference contrast (Normarski microscopy) which uses polarized light to enhance the contrast of the image. As such, these images in Figure 3-5 are not necessarily shown with their true colors. To prepare these coupons for these images, the procedure in section 3.2.1 was followed. Refer to Appendix C for images of these samples at a higher magnification.

From the results seen in Figure 3-2, focus was placed on the 50 ppm and the 100 ppm samples. These products formed quickly, thus allowing for rapid laboratory testing, and appeared to consitute two different corrosion products. Based on the their coloring, the black corrosion product was assumed to be mackinawite or pyrrhotite and the gold corrosion product to be pyrite. However, that remained to be proven. A variety of techniques including x-ray diffraction spectroscopy, Raman spectroscopy, and energy dispersive x-ray spectroscopy were used to validate these samples.

3.2.1 Washing and drying the coupons in preparation for testing

To prepare a coupon for any sort of testing, it must be first thoroughly washed and dried. Since these coupons were corroded inside a 1 M sodium sulfate salt solution, failure to adequately wash and dry these coupons would cause a large quantity of salt to crystallize on top of the sulfide films, potentially contaminating any data obtained. This following procedures outline the method for drying the coupon that was uniformly used for all types of testing: The coupon was removed from the sulfide

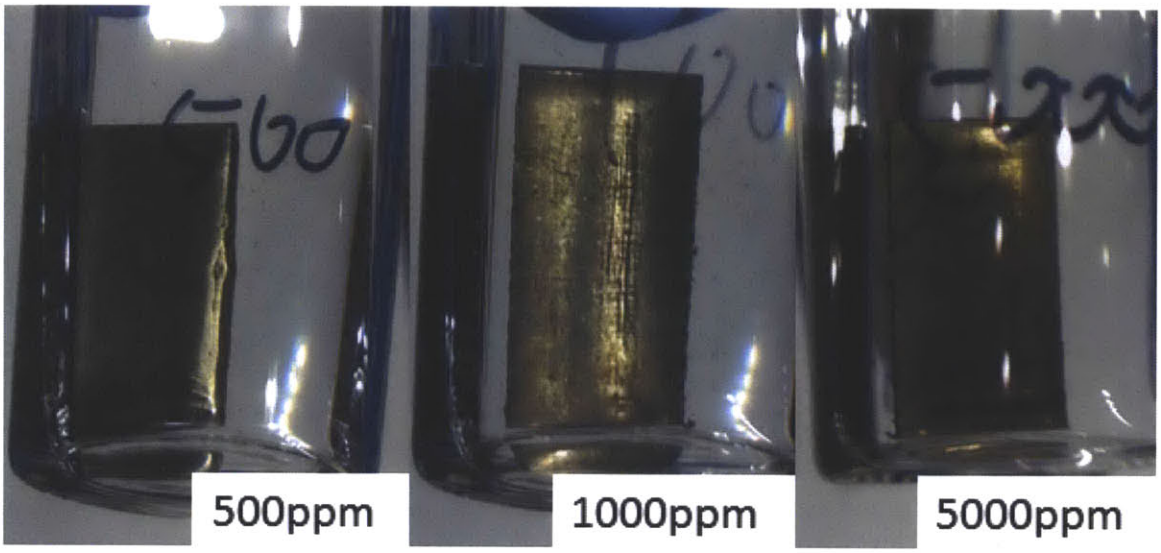

Figure 3-4: These coupons had been submerged in the sulfide solution for 7 days at the time these images were taken. These samples remained the color of steel for several days after initial submersion, but eventually turned golden as well.

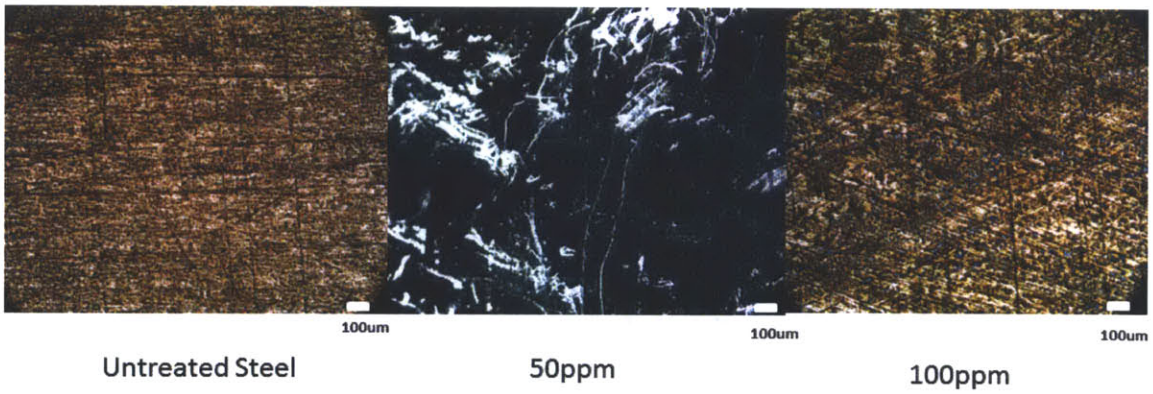

Figure 3-5: These images were taken using differential interference contrast (DIC) and are not necessarily real colored. Images were taken at 90x magnification; scale bars are 100 μm.

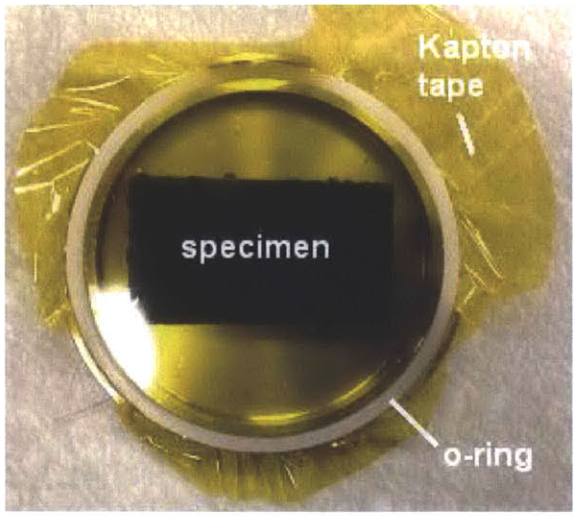

Figure 3-6: Specimen holders of the type shown was used for XRD. These holders are made airtight by an o-ring that clamps a piece of Kapton tape (an x-ray insensitive polyimide film) over the face of the holder.

solution and washed by dipping it into deoxygenated and deionized water at neutral pH while inside the anaerobic glovebox. A kimwipe was used to wick away most of the moisture. The coupon was then left to air dry inside a Petri dish for 1 hour in the glovebox.

3.2.2 X-ray diffraction

In order to determine the chemical composition and structure of the 50 ppm and 100 ppm iron sulfide corrosion products, X-ray diffraction (XRD) was used. Since these iron sulfide corrosion products are sensitive to oxygen, special care had to be taken in preparing these samples for XRD. Special airtight specimen holders were used, an example of which can be seen in Figure 3-6. These holders were made of stainless steel and were borrowed from Dr. Scott Speakman of the x-ray diffraction lab in CMSE. These holders are made airtight by a plastic o-ring (not shown) which clamps a piece of Kapton tape (an x-ray insensitive polyimide film) over the face of the holder.

Both the 50 ppm and 100 ppm coupons were tested using XRD. The coupons were prepared and dried according to the procedure in section 3.2.1. The specimen holders were passed into the glovebox. A small piece of molding clay was applied to the center of the specimen holder in order to adhere to the coupon. The coupon was

placed on this piece of clay and a glass slide was used to press down on the coupon, making it flush with the raised edges of the specimen holder. A piece of Kapton tape was then clamped into the holder by means of a plastic o-ring. Because the coupon was made flush with the edge of the specimen holder, the Kapton tape was taut and in contact with the top face of the coupon. The specimen holder was then passed out of the glovebox and taken to the x-ray diffraction facility in the Center for Materials Science and Engineering (CMSE) at MIT.

A PANalytical X'Pert Pro Multipurpose Diffractometer was used to take the XRD data. A Soller slit of 0.004 rad was used. The divergence slit was set to automatic mode with an illuminated length of 6 mm and a slit size of 2 degrees. The sample was scanned using the Bragg-Brentano configuration from 25 to 70 degrees over 3 hours using Cu alpha1 radiation from a generator set at 40 kV tension and 40 mA current. Other devices, such as a Rigaku Smartlab, and other configurations such as grazing incidence x-ray diffraction were attempted, but those yield no viable results. In these cases, no peaks aside from the iron of the coupon substrate were detected. The measured XRD spectra were analyzed using PANalytical's HighScore Plus program.

3.2.3 Raman spectroscopy

In addition to x-ray diffraction, Raman spectroscopy was also attempted on both the 50 ppm and 100 ppm samples. X-ray diffraction would only identify phases that contain a well defined crystal structure, but Raman spectroscopy is capable of detecting amorphous phases as well. After drying the coupons in accordance with section 3.2.1, they were brought to the Grossman Lab at MIT where Dr. Nicola Ferralis provided aid in obtaining the Raman spectra for each sample. Additionally, Raman spectroscopy was also conducted on an iron sulfide desposited electrode as described in Section 2.2.3.

A 633 nm laser beam with a maximum intensity of 10mW was used with a 100x objective with a numerical aperature of 0.8. The spot size of this beam was approximately 965 nm. A Horiba LabRam 800HR spectrometer was used to record the Raman shifts.

Since some of the measured Raman spectra did not match any literature spectra precisely, it was hypothesized that the corrosion product on these coupons consisted of several phases simultaneously. In pursuit of this idea, a Raman peak matching program was written in Matlab to combine several spectra from literature (see Appendix D) and then to compare this to the measured data.

Complicating the development of the Raman peak matching program was the

fact that intensity, and thus the shape of each peak, contains no information regarding the chemical composition of the material measured. Rather, the intensity contains information regarding the fractional quantity of material present in addition to other information about the mechanical state of the detected phases. It is only the peak positions which matter when using Raman spectroscopy to identify unknown materials.

The program that was written first normalized the literature data to fit within an intensity range of 0-1. It then smoothed the literature data using a 3-point moving average, iterated until the maximum change between each smooth operation caused less than 0.0001 change in the intensity at the most. Then, using a nested for loop, the 7 literature spectra were linearly combined using a variety of weights ranging from 0 to 1 in steps of 0.2. For each combination of the literature data, the combined spectra was first normalized, then the peaks were found by detecting the points where the derivative changed signs from positive to negative. These detected peaks were then filtered to only include the ones that are at least 1% higher in intensity than the minimum intensity within 10 wavenumber – this would only find peaks that rose a significant amount (1% of the the total range) from its immediate surroundings. These significant peaks and the weights used to generate it were then saved in a library of literature spectra combinations. Generating this library took approximately 3 days for 7 literature spectra.

The measured data from the coupons was then normalized, smoothed, and their peaks found using the exact same procedure as for the literature spectra. The peaks from the measured data was then compared to the peaks saved in the already generated library of literature spectra combinations in order to find the best match. Each peak in the measured spectra was matched to the closest peak within 20 wavenumber in the literature spectra, if able, and this difference recorded in an error vector. Thus, the maximum error for a matched peak is 20. For every unmatched peak, either in the measured spectra or in the literature spectra, an error of 100 was added to the error vector. Not penalizing these missed peaks would bias the program toward spectra with the most peaks since these have the greatest probability of making matches.

Each element in the error vector was then squared, and these values were summed to create a scalar score that represented the goodness of the fit between the measured spectra and the literature spectra combination. A lower score indicated better matches. The top 50 unique matches with the lowest scores were then examined manually to ensure that the proposed best matches remained consistent with each other. It should be noted that the best matched spectra's composition is only an approximation because of the low granularity of the weights used. Moreover, small changes

in weights may not appreciably change the combined literature spectra enough to cause the creation, deletion, or shift of a peak. As a consequence, what may appear to be trace elements can also be attributed instead to this inherent noise in the program. Thus, by examining the top 50 best matches outputted this program I could filter this noise out by only focusing on consistent patterns which appear in all the best matched spectra.

3.2.4 X-ray photoelectron spectroscopy

X-ray photoelectron spectroscopy (XPS) is a technique which is used to determine the both the elemental composition of a material and the electronic states of these elements. It does not give direct information regarding the strucuture of the material, but this may be inferred from the electronic states of the elements involved. XPS was conducted with the aid of Will Herbert, DMSE PhD candidate in both the Van Vliet and Gradecak groups. Due to time constraints, only the 100 ppm gold corrosion product was tested. To accomodate the size constraint of the XPS device, the steel coupon was cut down to a 1 cm x 1 cm size (1.5875 mm thick) instead of the normal size. These smaller coupons were grown in a 100 ppm sulfide solution as outlined earlier in the Section. These coupons were dried according to the procedures in Section 3.2.1. Once dried, these coupons were seal tightly in a 20 mL scintillation vial and brought to the Gradecak Lab in building NW13 where it was turned over to William Herbert.

3.2.5 Energy dispersive x-ray spectroscopy

Like XPS, energy dispersive x-ray spectroscopy (EDX) is a technique which is used to determine the elemental composition of a material but cannot give information regarding morphology or structure. In addition, EDX lacks the ability of XPS to determine the electronic state of the elements. The 50 ppm and 100 ppm coupons were dried according to the procedures in Section 3.2.1. Once dried, these coupons were brought to the Jeol 6610LV scanning electron microscope (SEM) in the DMSE department (Room 4-131); this SEM is capable of taking EDX data in addition to the usual imaging. These coupons were attached to the provided sample holder using carbon tape. Copper tape was also used to connect the coupons to the stainless steel sample holder in order to prevent the coupon from charging. The coupon were then placed inside the SEM which was pumped down to a high vacuum. Using a beam voltage of 20 kV, EDX spectra were acquired for both samples.

The acquired EDX spectra showed a very large percentage of iron content, greater

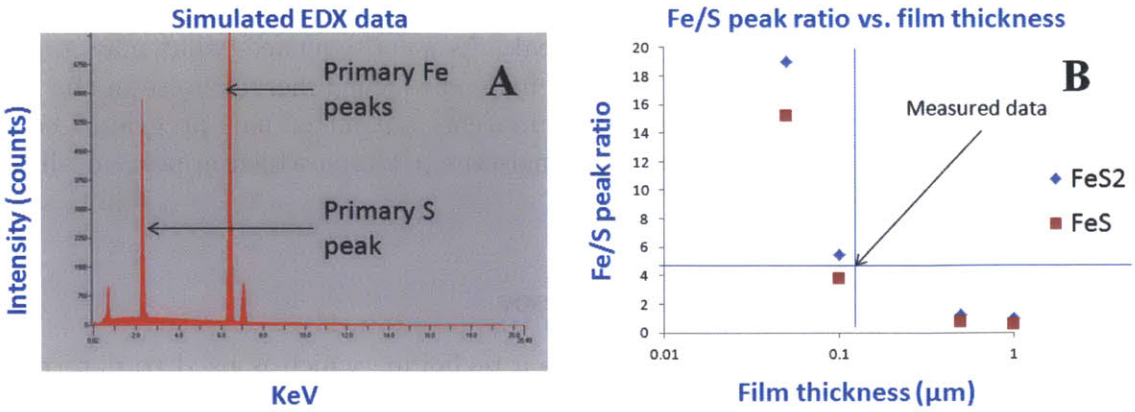

Figure 3-7: A) This is an example of a simulated EDX spectra for a pyrite (FeS_2) thin film with an iron substrate. By varying the film thickness within the simulation, the primary iron and sulfur peaks will change in relative intesity with respect to each other. B) By correlating the Fe/S intensity ratio to film thickness, a calibration curve can be generated. Shown on this graph is also the Fe/S ratio for an EDX spectra measured on the gold colored corrosion product.

than could be contained by an iron sulfide phase. This observation lead to the hypothesis that the iron sulfide corrosion product was thin, possibly on the order of a few micrometers. If the corrosion product were this thin, the excitation volume of the electron beam would penetrate through the film and into the un-corroded steel substrate underneath, subsequently causing the iron signal in the EDX spectra to be overrepresented. To compensate for this, Monte Carlo simulations were conducted using Small World's Electron Flight Simulator software to model the penetration depth of the electron beam. By assume a chemical composition (FeS_2 for pyrite and FeS for mackinawite), simulated EDX spectra can be acquired for a variety of film thicknesses. The simulated EDX spectra can then be correlated to film thickness by using the magnitude ratio between the largest iron peak and the largest sulfur peak as a fitting parameter. This ratio from a real sample can then be used to give information about the iron sulfide's film thickness. Figure 3-7 shows the results of this calculation.

3.2.6 Atomic force microscopy

Because the composition of the iron sulfide film had to be assumed for the EDX Monte Carlo simulations to work, independent verification of the film thickness was

required. For this, atomic force microscopy was used. The coupons used for these measurements were modified from the ones that have been used in previous tests.

Two methods to obtain the iron sulfide film thickness were attempted: a partial film was grown by masking part of the steel coupons with scotch tape, and existing iron sulfide films were scratched using a razor blade or a copper wire. For the latter case, iron sulfide films were grown as detailed earlier in this Section. Afterwards and immediately before profiling using the AFM, the iron sulfide film was scratched. A razor blade was originally used, but it tended to scratch the underlying steel coupon, resulting in the use of a copper wire instead. Since copper is softer than steel, it could scratch off the iron sulfide film without damaging the underlying steel.

An MFP-3D atomic force microscope (Asylum Research) was used. The cantilever (Veeco) had a nominal spring constant of 0.01 N/m. A scan size of 40 x 40 μm with a rate of 0.05 Hz was used. The set point was 1 V. The cantilever tip was aligned to the edge of the iron sulfide film (either the edge was caused by masking with scotch tape or by scratching the film with a copper wire) using the microscope's built in CCTV and through repeated scans using the AFM itself. The cantilever was considered properly aligned when initial line scans showed a sudden change in sample height to correspond to the edge of the film.

3.2.7 Profilometry

In addition to using atomic force microscopy to measure iron sulfide film thickness, profilometry was also used. A Tencor P-16 surface profilometer in CMSE (Room 4111) was used with the aid of Tim McClure, project technician. Samples were prepared in the usual manner, and the resulting iron sulfide films were scratched using a copper wire. Mr. Tim McClure operated the device, directing its 2 μm radius diamond tipped stylus to conduct a line scan across the scratch. The device applied 19 mg of force (cannot be changed) to the stylus and had a nominal maximum height resolution of 20 Angstroms.

3.3 Results and Discussion

3.3.1 Iron sulfide film growth

Table 3.2 shows that at least two different iron sulfide corrosion products formed on the steel coupons. When the sulfide concentration was below 100 ppm, a loose black product formed. When the sulfide concentration was 100 ppm or higher, a gold film formed. Moreover, the higher the sulfide concentration, the longer it took for the

gold coloring to appear. At 100 ppm, the gold coloring appeared after 24 hours. At 500 ppm and above, it appeared some time between 3 and 7 days after initial submersion. This could be explained, in part, by the aging of the sulfide solution as it became less potent with time. When the sodium sulfide nonahydrate was added to the 1 M sodium sulfate solution, the pH of the solution went up dramatically. The sulfate solution began at a pH of 3, but immediately after adding the sodium sulfide it went above pH 6. This was measured using pH paper, so more accurate reading could not have been taken. Over time, however, the pH of the sulfide solution dropped until it approached 3. The effect was likely caused by the recombination of the sulfide anion S^{2-}, a base, with hydrogen ions to form H_2S, hydrogen sulfide gas, which would subsequently leave the solution. This process can be confirmed by the strong characteristic "rotten egg" smell of hydrogen sulfide that these solutions constantly emit.

Thus, it is likely that the higher concentration of sulfides do not produce the gold colored corrosion product directly, but rather those solutions would eventually degrade to a regime where such products would form. Nevertheless, there is some sort of phase change which occurs around the 100 ppm mark that separates the black corrosion product from the gold corrosion product. This effect may be due to a stoichiometric balance between the amount of exposed iron atoms to the amount of sulfide in solution. In support of this hypothesis, experiments using smaller sized coupons required, in general, less sulfide concentration to achieve the same coloring of corrosion products. In the extreme case, no corrosion products were formed on the small amount of exposed steel on the working electrodes that were used in Chapter 2.

However, Rickard showed through experiments that two competing mechanisms exist for the reaction between ferrous ions and hydrogen sulfide [53]. At high neutral to alkaline pH with sulfide concentrations at parts-per-million level and above, the Fe^{2-} reacts with HS^- (the stable form of hydrogen sulfide at basic pH) to form an $Fe(HS)_2$ intermediate – the conversion of this ferrous bisulfide to an iron sulfide such as mackinawite is relatively slow kinetically. At acidic pH with sulfide concentrations below the parts-per-million level, the Fe^{2-} reacts with dissolved H_2S to form iron sulfide directly through a fast mechanism. This mechanistic dependence on pH may somehow account for the two different colored corrosion products that were observed. My experiments, however, were concerned with sulfide concentrations well within the parts-per-million regime.

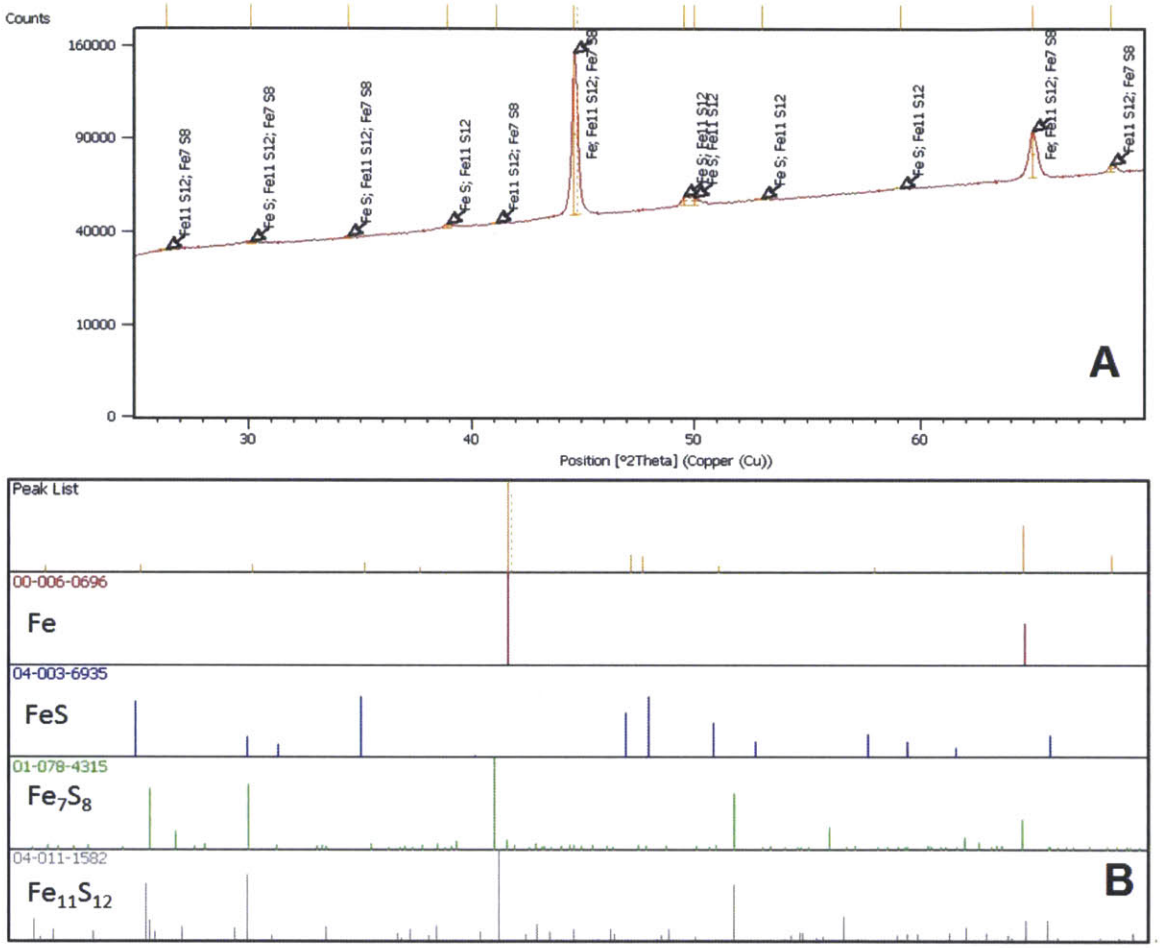

Figure 3-8: The measured XRD spectra for the 50 ppm coupon (black colored corrosion product). A) The measured spectra. B) A stick diagram to aid in matching peaks.

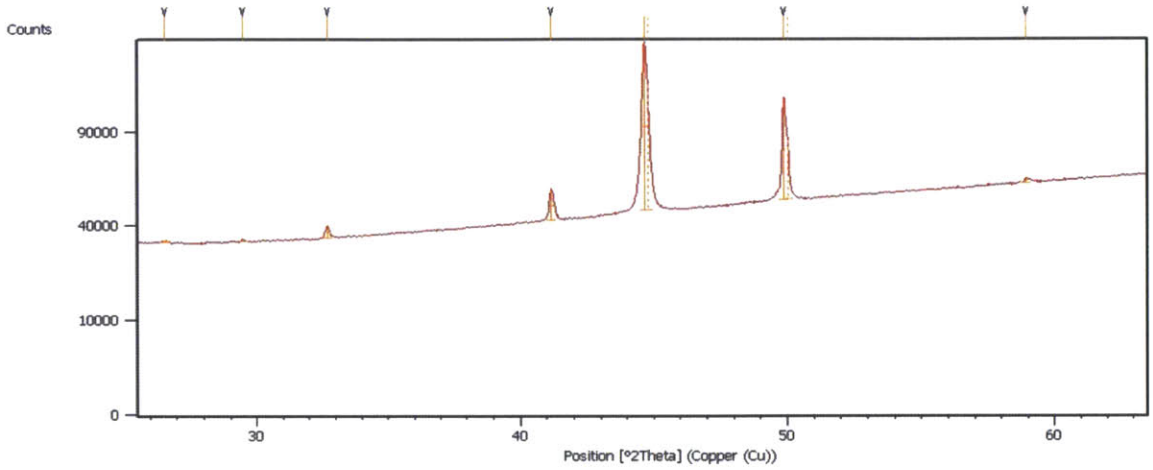

Figure 3-9: The measured XRD spectra for the 100 ppm coupon (gold colored corrosion product). No strong matches were found in the database.

3.3.2 X-ray diffraction results

As can be seen in Figure 3-8, XRD shows that the black colored iron sulfide corrosion product consists of a mixture of mackinawite (FeS) and two forms of pyrrhotite (Fe_7S_8 and Fe_11S_12). These results were within my expectations. However, the XRD data for the gold colored iron sulfide corrosion product (Figure 3-9) showed a pattern that was not recognized by the peak matching software. The coloring of the corrosion product would indicate that it was pyrite, but pyrite peaks were not detected. The single strong peak at 45^o is most likely iron, but the other three peaks were not matched with a specific element. There was not enough data present to definitively match these peaks.

3.3.3 Raman spectroscopy

Since XRD failed to identify the 100 ppm corrosion product, Raman spectroscopy was attempted. Its benefits are that it can detect non-crystalline phases and that the laser beam used would excite less volume than the x-ray source in XRD. Additionally, the symmetric Fe-Fe bonds in iron do not have a Raman spectrum and would not appear in a reading. This eliminates one of the variables that confounded the XRD and EDX data. In fact, the signal for iron is the strongest one in the measured XRD spectra such as Figure 3-8.

Both the black iron sulfide corrosion product on the steel coupon and the one

that was electrochemically deposited onto the working electrode exhibited the same Raman response and thus will be discussed together. The measured Raman spectra changed irreversibly with the intensity of the laser beam used (Figure 3-10). At low laser power of 1 mW (Figure 3-10A), an approximate 1:1 ratio mixture of greigite and marcasite was detected (see Table 3.1). When the laser intensity was increased to 2.5 mW (Figure 3-10B), an approximate 1:1:1 ratio of marcasite, pyrite, and pyrrhotite was detected. When the intesity was raised to the maximum power of 10 mW (Figure 3-10C), the measured spectra became purely mackinawite. All of these phase transformations appeared to be irreversible as lowering the power did not undo the transformation. Figure 3-10D shows a measurement taken at 2.5 mW after a full powered measurement – rather than recovering the spectra previously measured at this intensity, the spectra remained that of mackinawite. The output of the peak matching program can be seen in Figures 3-11 through 3-13. It should be noted that all the quoted composition ratios are approximate since the resolution of the weighting function used was low.

The transformations observed in this experiment are contradictory to existing knowledge with respect to iron sulfide stability [44]. Mackinawite is a metastable phase that is often used in laboratory experiments to form the other iron sulfide phases, whereas the other phases should be thermodynamically more stable. I can surmise two possible explanations for this phenomenon. According to measurements taken by Dr. Nicola Ferralis, the atomic bond temperature of the material illuminated by the Raman laser exceeded 600^{o} C – such a high temperature may be sufficient to convert the material back into a higher energy state such as mackinawite. Alternatively, new mackinawite may have been formed as a side effect of this elevated temperature. Although the sample was dry on a macroscopic sense, pockets of moisture may have been trapped within the corrosion product. The application of the laser beam may have dried the material further. The formation of mackinawite from solution is greatly accelerated during the drying process [54]. Thus, it could be that new mackinawite was formed as a response to the applied laser, obscuring the pre-existing phases. The higher intensity in the Raman spectra for mackinawite in Figure 3-10D relative to the other spectra lends some support to this idea.

Unfortunately, the Raman spectra for the golden-colored corrosion product could once again not be matched. Figure 3-14 shows the best matched literature spectra as obtained by the program. Nominally, the best matched spectra consisted mostly of mackinawite plus a large amount of the other phases. The presence of these other phases, however, served only to blunt the peaks at 500 cm^{-1} and above to below the program's peak detection limit. Since the program applies a large penalty against unmatched peaks, the presence of the other phases in the best match can only be

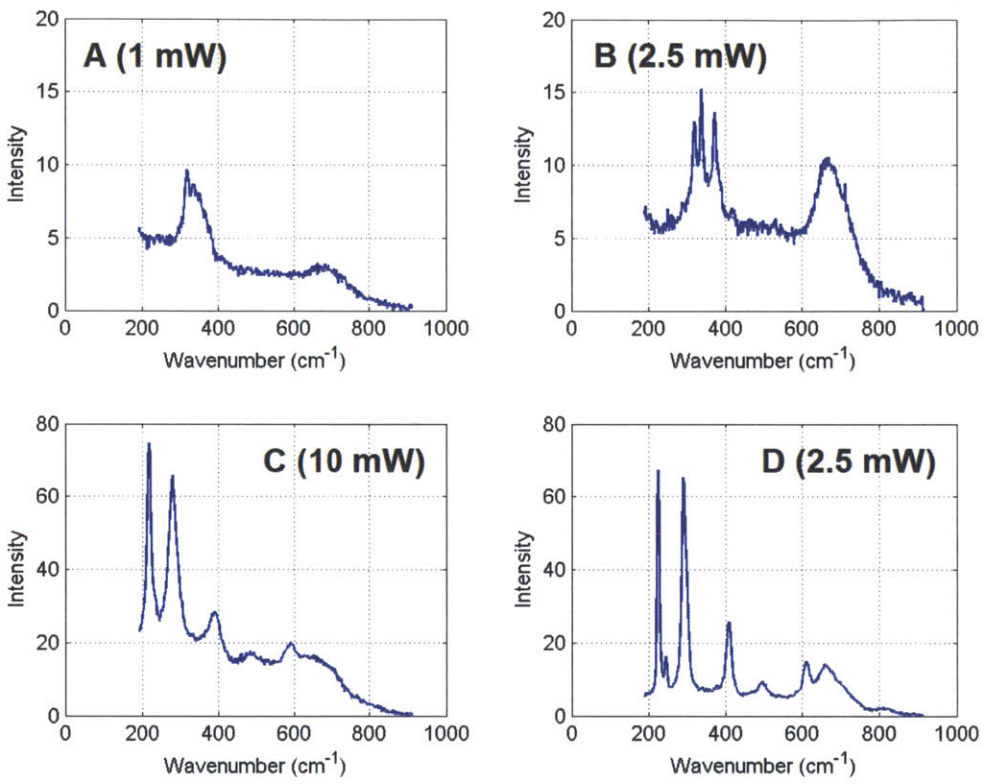

Figure 3-10: The measured Raman spectra for the black corrosion product that was developed on the steel coupon and on the working electrode. All measurements shown here were made at the same location in chronological order. A) Initial spectra measured at 1 mW laser power. B) Spectra measured at 2.5 mW. C) Spectra measured at 10mW (full power). D) Spectra measured at 2.5mW.

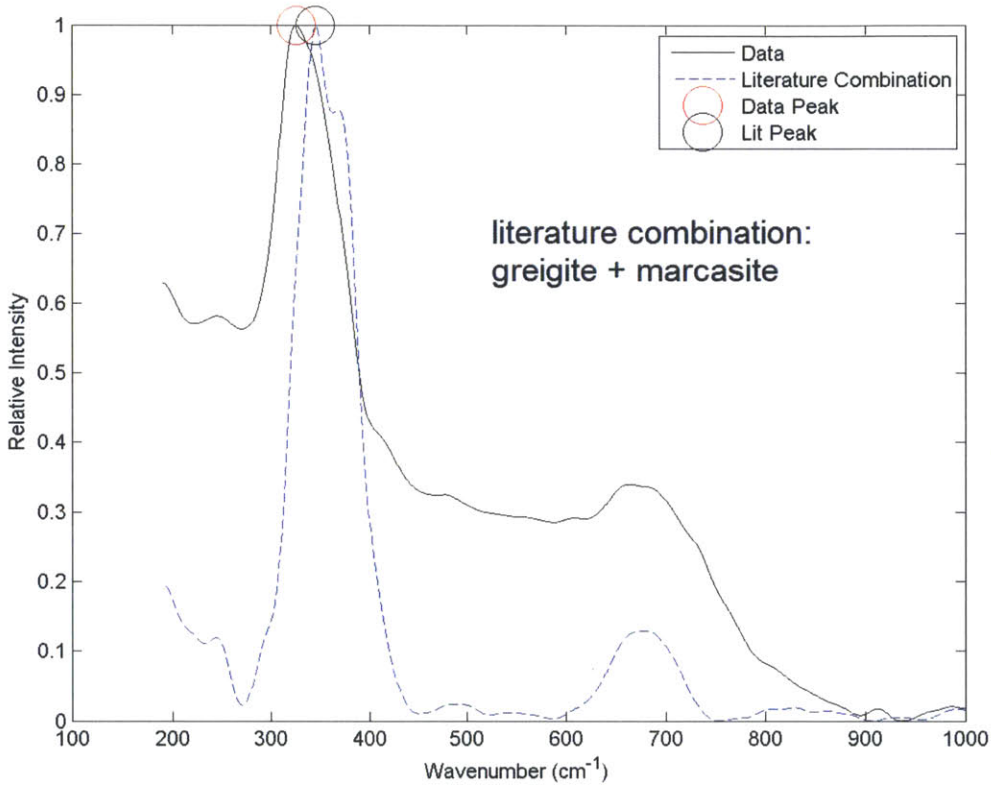

Figure 3-11: Peak matching for the 1 mW spectra on the black iron sulfide corrosion product: the combination of literature spectra that best matched the measured spectra consisted of an approximate 1:1 ratio of greigite and marcasite.

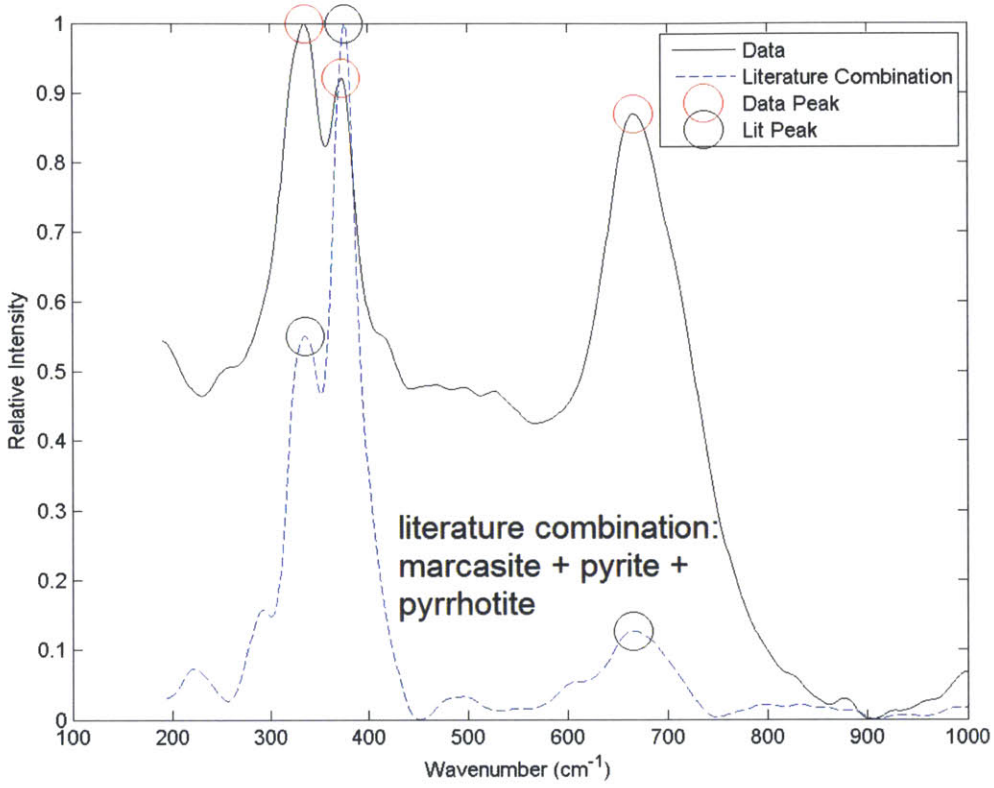

Figure 3-12: Peak matching for the 2.5 mW spectra on the black iron sulfide corrosion product: the combination of literature spectra that best matched the measured spectra consisted of an approximate 1:1:1 ratio of marcasite, pyrite, and pyrrhotite.

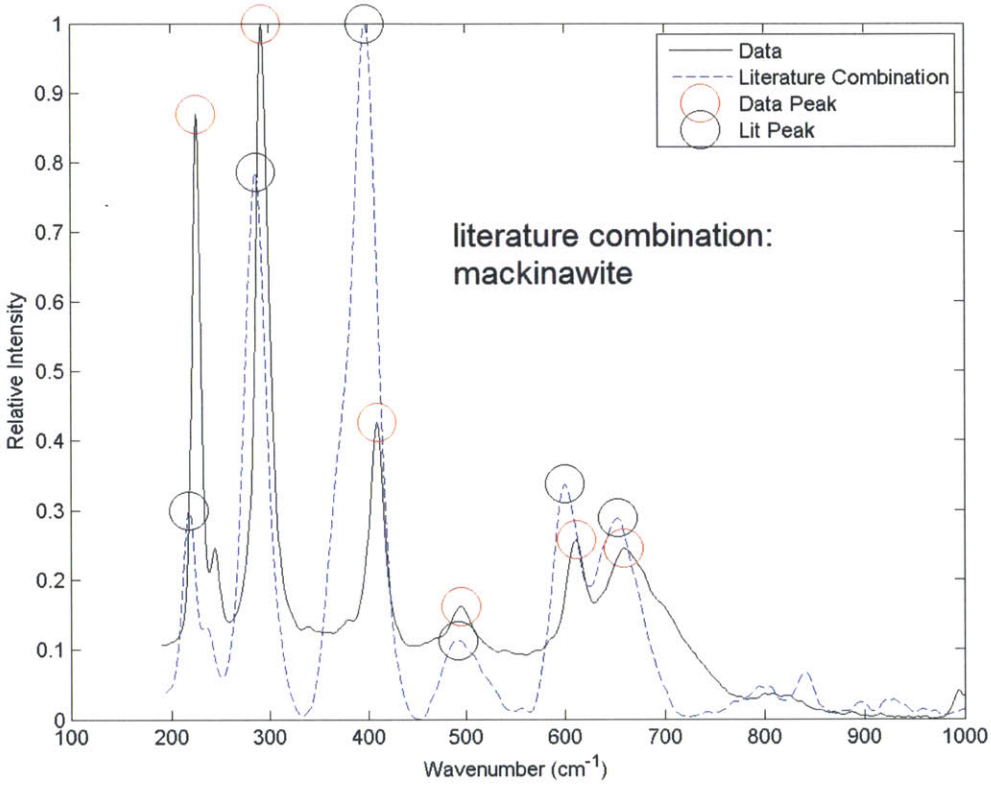

Figure 3-13: Peak matching for the 2.5 mW spectra on the black iron sulfide corrosion product after a 10 mW reading: the combination of literature spectra that best matched the measured spectra consisted solely of mackinawite.

described as a result of a bug in the program. By allowing a large degree of freedom in terms of literature spectra combinations (6^7 combinations were considered in total), exploitation of arbitrary programming restraints such as a peak detection cutoff is inevitable.

Nevertheless, it can be concluded that the golden-colored corrosion product cannot be adequately described by any combination of the 7 literature spectra used (Appendix D). These 7 literature spectra were chosen to represent the most common iron sulfide corrosion products, but it is quite possible that this gold colored material may not be an iron sulfide at all. A cursory search through the database (the RRUFF Project) of Raman spectra showed that all of the iron sulfides contain a pronounced peak at approximately 400 cm^{-1} which the golden-colored corrosion product clearly lacks. It may be possible that this gold colored material resulted from a reaction between other elements within the system, namely the sulfate that was in the solution. The measured Raman spectra, however, does not match that of either Na_2SO_4 or $FeSO_4$. The black corrosion product, however, was identified precisely through the use of Raman spectroscopy.

3.3.4 X-ray photoelectron spectroscopy results

Figure 3-15 shows the XPS spectra measured from the 100 ppm golden-colored corrosion product. Since the coupon had to be exposed to oxygen in order to both transport and load the sample into the device, it unexpectedly oxidized, causing the displayed oxygen peaks. According to Will Herbert's analysis:

> The film contains sulfur, mostly S^{2-} (monosulfide), although there is some disulfide present also. The iron peak is hard to fit but to me looks like it contains a mixture of Fe^{2+} and Fe^{3+}. There is considerable oxygen which can either be absorbed on the surface but is more likely contained in the film as an oxide, and hence the reason for detectable Fe^{3+}.

The presence of both monosulfide S^{2-} corresponds to the presence of mackinawite or pyrrhotite while the disulfide S_2^{2-} corresponds to marcasite or pyrite. Since most of the detected sulfur was in the monosulfide form, it can be put forth that the golden-colored corrosion product is either mackinawite or pyrrhotite. Some amount of pyrite or marcasite may also be present. However, it is possible that the golden-colored corrosion product is not a pure iron sulfide at all. From Figure 3-15, the only elements present on the coupon were iron, sulfur, oxygen, and sodium; the detected carbon likely came from the carbon tape used to hold the coupon down, but some traces from the steel could also have been detected. Tantalum was also detected, but

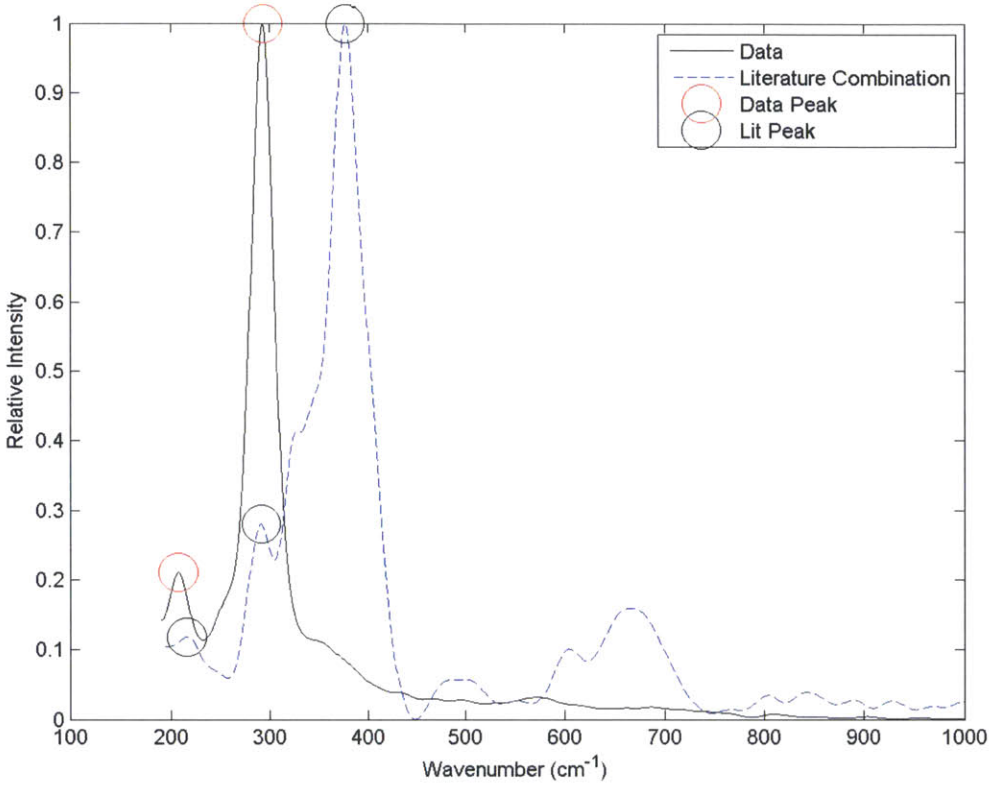

Figure 3-14: Peak matching for the golden-colored corrosion product: the combination of literature spectra that best matched the measured spectra consisted of mackinawite plus a large amount of the other phases. The other phases muddled the mackinawite spectra enough that the peaks at 500 cm^{-1} and above fell below the peak detection limit for the program.

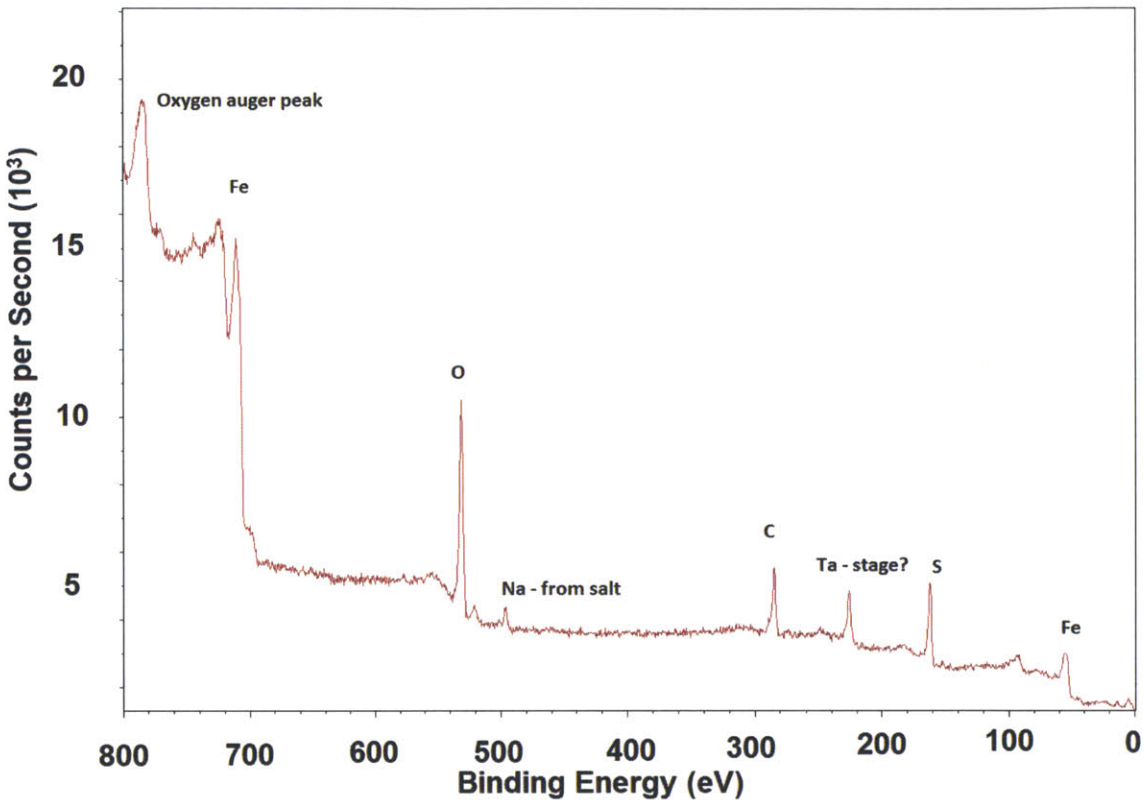

Figure 3-15: The measured XPS spectra for the 100 ppm golden-colored corrosion product.

that most likely came from the XPS stage since there is no other reason for it to be present. Nevertheless, the golden-colored corrosion product that formed may contain within it some amount of sodium or oxygen – such components would significantly alter the XRD and Raman spectra but would be indistinguishable from residual salt and oxide impurities in XPS.

3.3.5 Energy dispersive x-ray spectroscopy and film thickness measurement results

From the calculations done in Figure 3-7 B using the Monte Carlo simulations for the EDX spectra, the predicted film thickness for the black and gold corrosion products are between 0.1 and 1 μm. Unfortunately, the AFM measurements taken could not provide evidence for or against these predictions. Despite several attempts to create a sharp profile where the iron sulfide film is disrupted, the best AFM images taken all showed a sloped surface instead. This sloped surface was caused by a gradual decrease in film thickness near the disruption. These measurements were further complicated by the fact that the AFM's cantilever tip showed considerable attraction to the iron sulfide film. This attraction may have been caused by electrostatic interactions between the tip and the film. These complications were true for both the golden-colored and black colored iron sulfide corrosion products.

The profilometry was met with similar results. In this case, the stylus of the profilometer scratched through the iron sulfide film, measuring only the underlying steel. The was most likely due to the 19 mg of force that the device applied to the stylus, a setting that could not be changed.

3.4 Summary

Iron sulfide films were grown on AISI 1008 carbon steel coupons by submerging them in an acidic sulfide solution. At sulfide concentrations below 100 ppm, a loose black corrosion product formed. At sulfide concentrations above 100 ppm, an adherent golden-colored corrosion product formed. Additionally, an iron sulfide film was grown electrochemically on the working electrodes used in Chapter 2.

A variety of techniques were used in order to determine the composition and phase of these corrosion products. X-ray diffraction determined that the black corrosion product consisted of a mixture of mackinawite and pyrrhotite, but could not identify the golden-colored corrosion product. Raman spectroscopy recorded a different mixture of phases on the black corrosion product and on the electrodes that

depended upon the power of the laser beam applied: at low powers, a mixture of greigite and marcasite was found; at intermediate powers, a mixture of marcasite, pyrite, and pyrrhotite was found; and at high power, mackinawite was found. Such a transformation is counterintuitive to existing knowledge regarding iron sulfide phase transformation. Raman spectroscopy could not identify the golden-colored corrosion product. X-ray photoelectron spectroscopy found that the golden-colored corrosion product consisted mostly of monosulfide S^{2-} which corresponds to mackinawite or phyrrhotite.

Chapter 4

Comparison Between MIC and Abiotic Sulfide Corrosion

4.1 Introduction

The work presented in Chapters 2 and 3 touched upon purely abiotic forms of corrosion. In this chapter, I present both qualitative and quantitative comparisons between MIC and abiotic iron sulfide corrosion of the sort that was discussed in Chapter 3.

4.2 Methods and Materials

4.2.1 Growing the sulfate reducing bacteria

A freeze-dried stock of a sulfate-reducing bacteria (SRB), *Desulfovibrio vulgaris* (ATCC number 29579), was obtained from the American Type Culture Collection (ATCC). This initial stock was expanded by Dr. Matthew Whitfield, postdoctoral researcher in the Van Vliet Group, and frozen back down, after centrifuging, in order to create several vials of frozen bacterial stock.

Modified Baar's media for sulfate reducers (ATCC number 1249) was prepared according to the procedures outlined in Appendix E. Each batch made 500 mL of media. This media was divided into several 50 mL Falcon tubes to enable easier handling and to minimize risk of contamination. Unused media was stored inside a 4°C refrigerator, with the cap of the Falcon tube on tight to prevent oxygen from seeping in. This media was used as needed, and more was made when it ran out.

To grow the frozen bacteria, one full 50 mL tube of media was brought into the Shel Lab BacBASIC anaerobic glovebox where it was divided into two 50 mL Falcon tubes, one for control and one for the SRB. Each tube had approximately 22 mL of media. These two tubes were taken out of the glovebox and brought into a fume hood. The cap of the control media was removed in order to expose it to the ambient atmosphere. The box containing the frozen SRB stock was taken out of the -80°C freezer and brought into the fume hood. As quickly as possible, a pipette tip was scraped against the surface of the frozen SRB stock and then submerged in the media reserved for SRB. The pipette was pumped a few times in order to cycle media into and out of the tip. The frozen stock was then quickly returned to the freezer. Both tubes were capped and taken to the glovebox. Once inside the glovebox, both tubes remained tightly capped to prevent contamination. It took approximately 1 week for the SRB to grow, turning the media cloudy. The control media remained clear, indicating no contamination during this process. Once this bacteria culture was started, the media needed to be changed at least once a week. Changing the media consisted of simply transferring 1 mL of the old cloudy, SRB containing solution into approximately 15 mL of fresh media.

4.2.2 Qualitative comparison between microbiologically influenced corrosion and abiotic iron sulfide corrosion

SRBs were grown on the mild steel coupons that were used in Chapter 3. Each coupon was inserted into a 50 mL Falcon tube along with 15 mL of fresh media. 15 mL was used because this quantity totally submerged the coupon. To this media, 1 mL of the SRB containing solution was also added. Visible MIC was quickly observable; within 48 hours, the solution would turn dark black (Figure 4-1). The media for these SRB also required weekly changes. To change the media in this case, the coupon was simply moved into a new 50 mL Falcon tube containing 15 mL of fresh media. Various controls were also used to compare to the SRB containing media. Coupons were also added to: media without SRB; a solution containing 1 M Na_2SO_4 at pH 3; the same sulfate solution with an additional 50 ppm Na_2S. The coupon remained unchanged in the media without SRB, turned yellow-brown in the sulfate solution, and turned black in the sulfate solution containing 50 ppm Na_2S. Based on its color, the yellow-brown corrosion product in the sulfate solution is most likely ferric sulfate ($Fe_2(SO_4)_3$). All of the procedures described above took place inside the anaerobic glovebox.

In order to compare the corrosion caused by MIC and that caused by abiotic iron sulfide corrosion, three coupons were inserted into three different solution in the

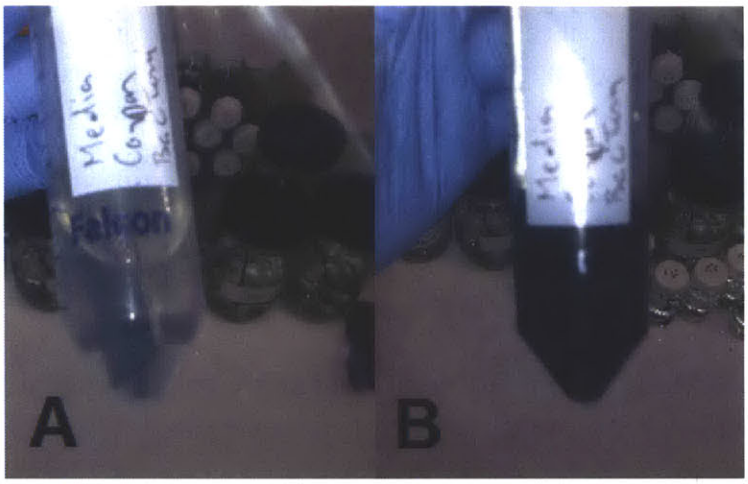

Figure 4-1: A mild steel coupon was submerged in 15 mL of modified Baar's media for sulfate reducers, and 1 mL of SRB containing media was added. A) Immediately after adding the SRB solution. B) 48 hours after adding the SRB solution.

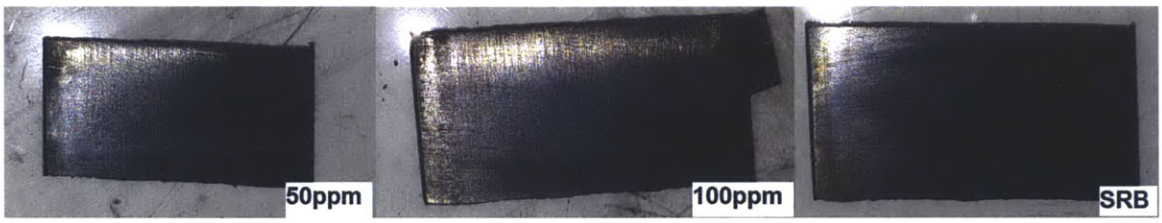

Figure 4-2: These coupons were corroded in various conditions. They were cleaned by submerging them in 20 mL of ethanol in a Falcon tube and placed in a sonicator for 2 hours.

anaerobic glovebox at the same time. The first contained 15 mL of the modified Baar's media containing SRB, the second and third contained 50 ppm and 100 ppm sulfide solutions as described in section 3.2. These three coupons were allowed to corrode for 1 week. After 1 week, all three coupons were removed from their respective solution and placed in 20 mL of ethanol in 50 mL Falcon tubes. These tubes were then brought out of the glovebox and placed in a sonicator. After 2 hours of sonication, a significant amount of the corrosion product was removed. However, all three coupons remained discolored which indicated the presence of a chemically bonded corrosion product (Figure 4-2).

In order to remove this chemically bonded corrosion product, each coupon was gently polished by hand on a 0.5 μm diamond grit lapping paper (Beuhler). These

coupons were polished until the first instance where the silvery color of the underlying steel could be seen. By doing this, minimal damage to the corrosion features on the steel surface was incurred. After polishing, each coupon was cleaning by sonication inside 20 mL of ethanol as before. These coupons were then brought to the Jeol 6610LV scanning electron microscope (SEM) in the DMSE department (Room 4-131) where SEM images were taken. The SEM was used in high vacuum mode with an electron beam voltage of 20 kV.

4.2.3 Electrochemical comparison between microbiologically influenced corrosion and abiotic iron sulfide corrosion

In addition to growing the SRBs on the mild steel coupons, SRBs were also grown on the working electrodes that were used in Chapter 2. Refer to Section 2.2.2 for more information regarding the design and construction of these electrodes. Each working electrode was inserted into a 50 mL Falcon tube containing 15 mL of fresh media. In this case, 15 mL was chosen because it was the amount used for the coupons. To this, 1 mL of the SRB containing media was added. This media was changed weekly by simply transferring the electrode to a new Falcon tube containing 15 mL of fresh media.

Unlike the coupons, MIC was not readily observed. Although the media turned cloudy, indicating the presence of live bacteria, it did not turn black even after 2 weeks. Likely, the exposed metal surface of the working electrode was too small to be able to generate enough ferrous ions to darken this solution within this time span. Regardless, live SRBs were confirmed to be present within the solution, thus a biofilm (although transparent) was assumed to coat the surface of the working electrode.

These biofilm coated working electrodes were tested by electrochemical experiments identical to those conducted in Chapter 2. Refer to Section 2.2.2 for the full procedures regarding the electrochemical experiments. No modifications were made to accommodate the live SRB biofilm.

In addition to testing working electrodes coated with live SRB biofilms, separate electrochemical experiments in which the bacteria cells were lysed were also conducted. By lysing the bacteria before the experiment, the effect of the biofilm could be isolated from the effect of the living bacteria. In order to lyse the bacteria without damaging the biofilm, the biofilm coated working electrodes were transferred to a 50 mL Falcon tube containing 40 mL of a 1% Alconox (a cleaning detergent) solution inside the glovebox. The electrode was allowed to sit in this Alconox solution for 1 hour immediately prior to the start of the electrochemical experiment.

4.3 Results and Discussion

4.3.1 Qualitative comparison between microbiologically influenced corrosion and abiotic iron sulfide corrosion

SEM images of the three polished coupons were taken. As mentioned, these coupons were previously corroded in an active SRB culture, and in a 50 ppm and a 100 ppm sulfide solution. Figures 4-3 through 4-5 are representative images of the surface condition of these samples. These images were taken using the secondary electron detector which specializes in imaging surface topology. Images were also taken using the backscatter electron detector, but those images tended to show material composition in addition to surface topology – denser elements would be brighter using this detector.

The surface of the coupon corroded in the 50 ppm sulfide solution (Figure 4-3) showed a great deal of damage. This is consistent with the loosely adhered black corrosion product that was found on coupons corroded in these conditions. This poor adhesion imparted poor protection of the metal surface from corrosion. Corrosion pits (roughly circular black spots) of approximately 1-3 μm can be seen throughout the surface. They are highly concentrated on the areas showing greatest damage.

In contrast to this, the surface of the coupon corroded in the 100 ppm sulfide solution (Figure 4-4) showed relatively less damage. The striations caused by polishing prior to submersion in the sulfide solution can still be seen. In addition to this, new material seems to have filled in parts of these striations. The pits here appear to be larger and more spread out. As a reminder, coupons corroded under these conditions grew a chemically adherent golden-colored film of unidentified iron sulfide composition. The relatively strong adherence of this film likely protected the metal surface from the extensive damage of the sort seen on the 50 ppm coupon. Moreover, the grains of the metal can be seen here, indicating some degree of intergranular attack.

Lastly, the surface of the coupon corroded by SRB (Figure 4-5) showed an intermediate amount of damage. The morphology of this damage is unlike that of the other two. It lacks the extensive damage seen on the 50 ppm coupon, but it also lacks the intergranular attack seen on the 100 ppm coupon. Long, thin cracks can be seen here. The pits that are present also appear to be correlated spatially with these cracks.

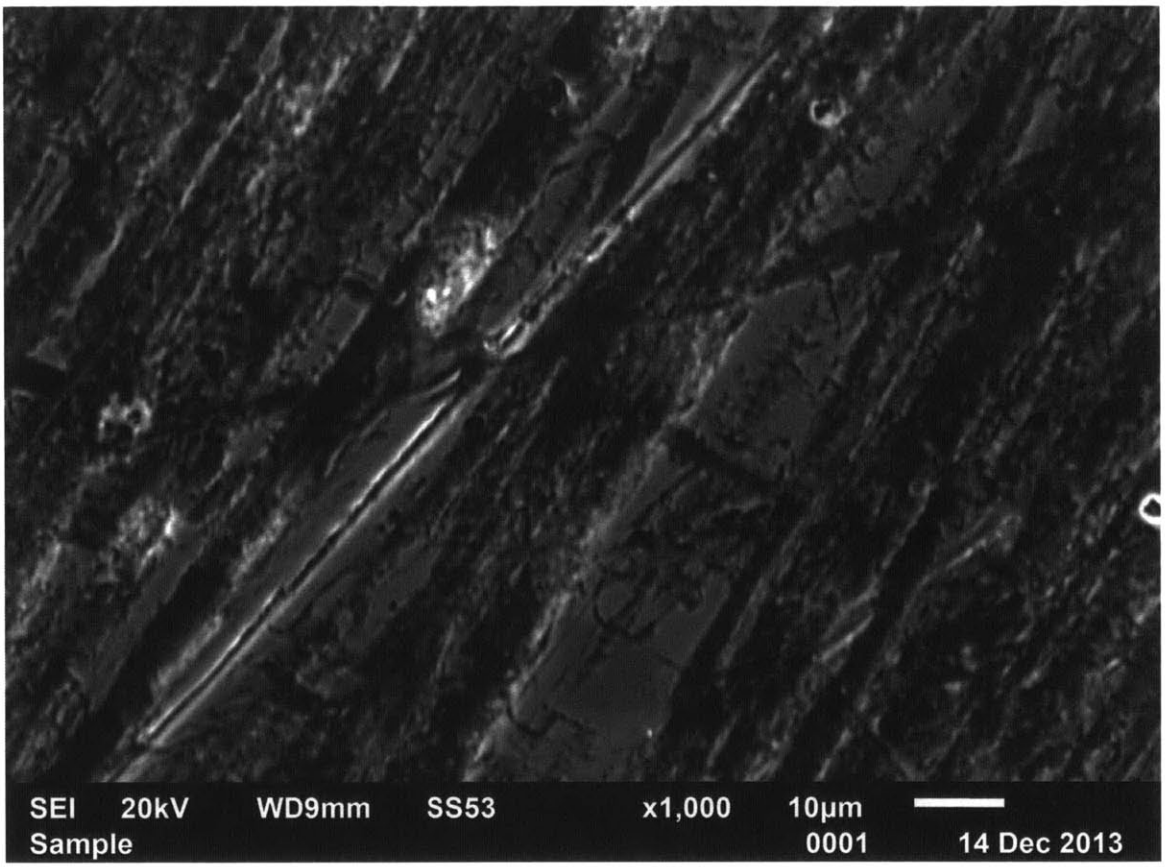

Figure 4-3: SEM image taking using the secondary electron detector of a coupon that had been corroded in a 50 ppm sulfide solution for 1 week.

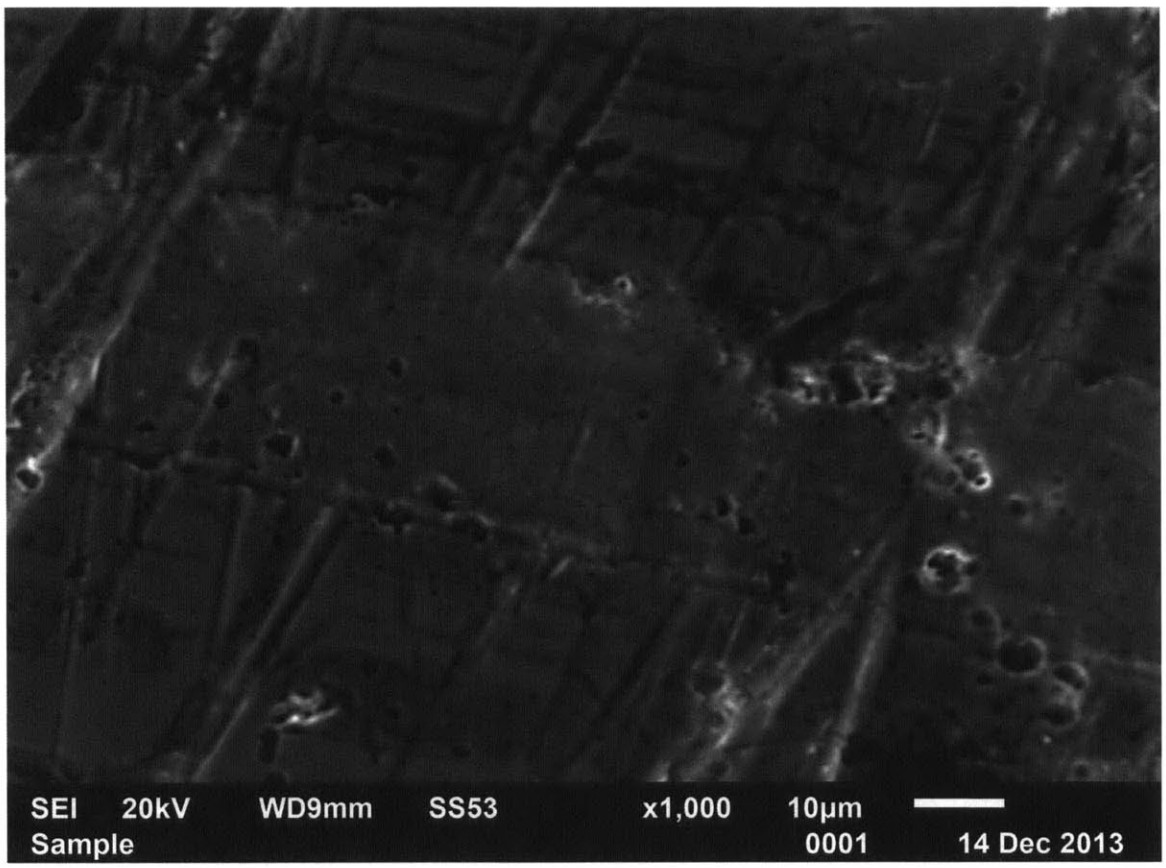

Figure 4-4: SEM image taking using the secondary electron detector of a coupon that had been corroded in a 100 ppm sulfide solution for 1 week.

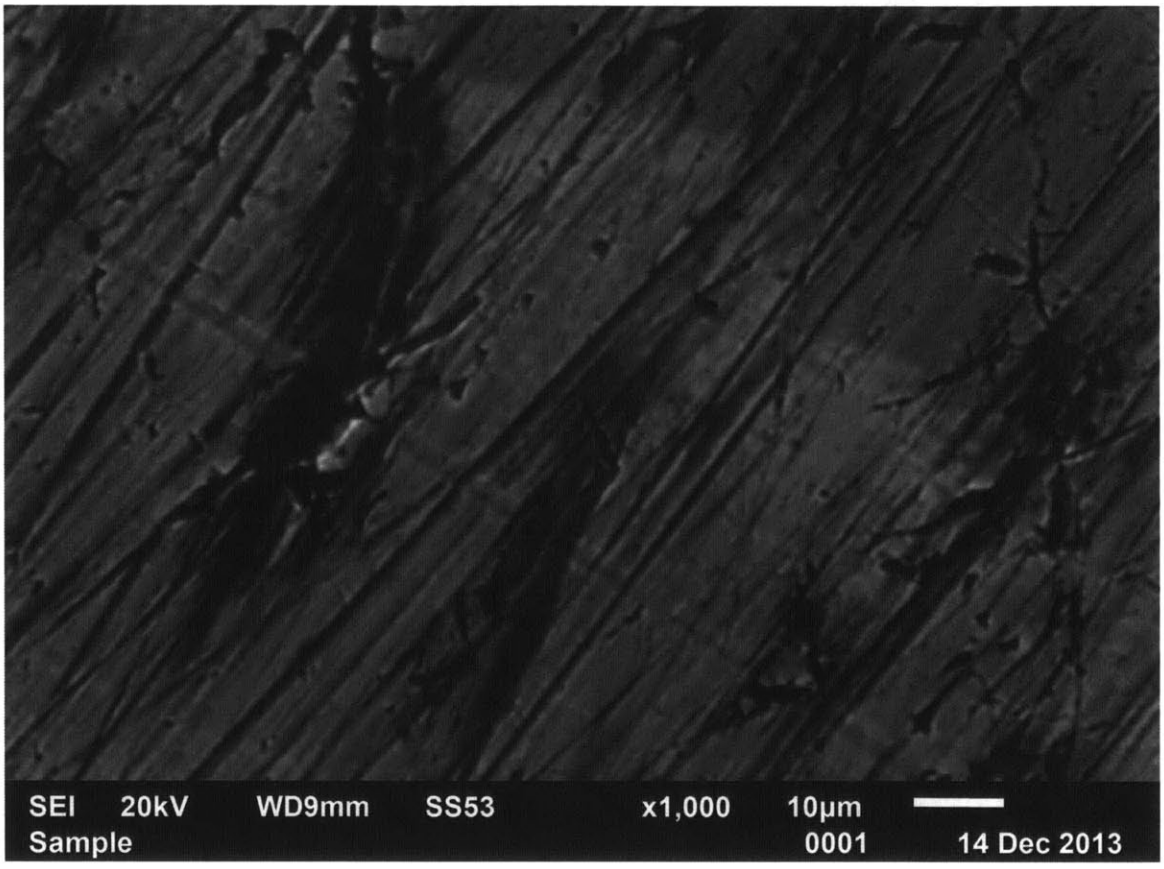

Figure 4-5: SEM image taking using the secondary electron detector of a coupon that had been corroded in an active SRB culture for 1 week.

4.3.2 Electrochemical comparison between microbiologically influenced corrosion and abiotic iron sulfide corrosion results

Figure 5-1 and Table 4.1 contain all the electrochemical data that was measured, including the data for the live SRB biofilm and the lysed SRB biofilm. Table 4.2 contains the statistical tests of significance conducted for both biofilms.

As can be seen from this data, both the living and lysed biofilms caused an increase in corrosion rate as compared to the bare steel control. Also, there is no statistically significant difference between corrosion rates for samples with the live and the lysed SRB biofilm. This implying that the living bacteria played little to no role in the measured corrosion rate; rather, it was the biofilm itself that caused the measured increase in corrosion. It should be noted that the bacteria were only assumed to be lysed – it may be possible that the biofilm itself provided enough of a barrier to protect the bacteria within from the Alconox detergent solution that was used to lyse them. I lacked any convenient method to test whether or not the bacteria within the biofilm survived the lysing procedure. Marking the bacteria within the biofilm using fluorescent dyes were considered, but no dyes specific to SRBs were immediately available. Transferring the nominally lysed SRB biofilm to fresh media was also considered. If any bacteria survived the lysing procedure, they would proliferate when placed in fresh media, but this process could take between a few days to weeks depending on how many bacteria survived. There was just not enough time.

Intriguingly, the increase in corrosion measured using the biofilm was approximately the same as the increase caused by calcium alginate alone, the iron sulfide alone, and the combination of calcium alginate and iron sulfide. Unfortunately, due to the high variance in the biofilm corrosion measurements, this inference cannot be concluded definitively. What is obvious, however, is that the biofilm did not provide a protective effect like that of agarose, as has been hypothesized in the literature. Of course, it should be noted that the results described here are applicable only to this specific species of SRB cultivated in these conditions – it may be that a biofilm that is the product of many bacterial species may behave differently from those observed here.

4.4 Summary

AISI 1008 carbon steel coupons were corroded in three different soultions: a 50 ppm sulfide solution, a 100 ppm sulfide solution, and an active culture of sulfate-reducing bacteria (SRB). These coupons were corroded for one week, then the accumulated

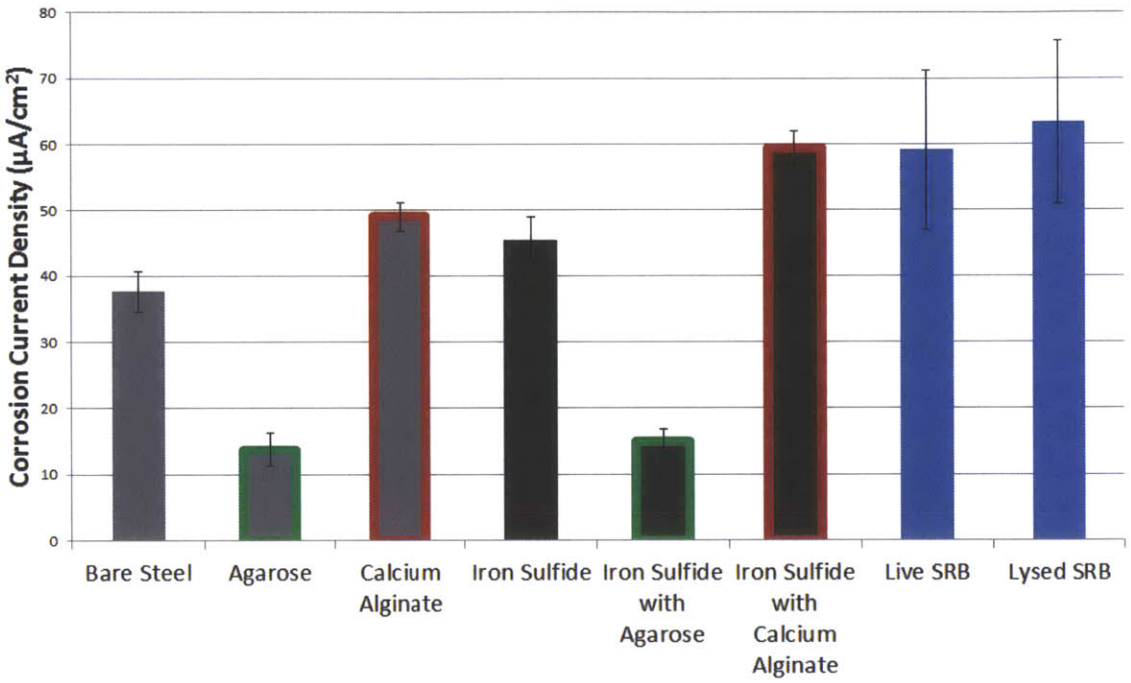

Figure 4-6: Compiled data for the electrochemical experiments including experiments involving SRB biofilms. Error bars are ± one standard deviation. Each bar excluding the SRB biofilm ones has been colored coded for convenience: grey fill color indicates a steel substrate; bronze fill color indicates an iron sulfide film substrate; green outline color indicates an agarose gel coating; red outline color indicates a calcium alginate gel coating; and no outline color indicates no gel coating.

Table 4.1: Electrochemical experimental results including experiments involving SRB biofilms (error is ± one standard deviation).

Condition	Number of Experiments	Mean Exchange Current Density ($\mu A/cm^2$)
bare steel	5	37.62 ± 3.08
agarose	4	13.67 ± 2.53
calcium alginate	4	49.03 ± 2.18
iron sulfide	2	45.55 ± 3.42
iron sulfide with agarose	3	14.98 ± 1.87
iron sulfide with calcium alginate	2	59.28 ± 2.73
live SRB biofilm	2	59.12 ± 12.04
lysed SRB biofilm	2	63.40 ± 12.35

Table 4.2: Statistical significance for the measured corrosion rates was tested for using t-tests with $\alpha = 0.05$. Entries are the p-values obtained from a two-tailed t-test. Italicized entries indicate no statistically significant differences between measured corrosion rates – all other entries are statistically significant.

	Steel	**Agarose**	**Calcium Alginate**	**Iron Sulfide**	**Iron Sulfide + Agarose**	**Iron Sulfide + Calcium Alginate**	**Lysed SRB Biofilm**
Live SRB Biofilm	0.0027	0.0012	*0.0548*	*0.1047*	0.0061	*0.0768*	*0.1117*
Lysed SRB Biofilm	0.0037	0.0004	0.0368	*0.0900*	0.0214	*0.5567*	-

corrosion product was removed. The underlying steel was imaged with scanning electron microscopy in order to determine qualitative differences: the 50 ppm coupon showed extensive corrosion damage, exhibiting a high degree of surface roughening; the 100 ppm coupon showed less damage with signs of pitting and intergranular damage; the SRB coupon showed localized cracking near pre-existing scratches.

Also, SRB biofilms were grown on the electrodes that were used in Chapter 2. Half of these biofilm were submerged in a detergent solution in order to lyse the bacteria within the biofilm, and half were not submerged. Both the lysed and living biofilm coasted electrodes were polarized electrochemically. Both biofilms exhibited similar corrosion rates, implying that the living bacteria had an insignificant effect on the overall corrosion rate.

Chapter 5

Conclusion

5.1 Summary of Results

From the electrochemical experiments conducted in Chapter 2, it was found that – contrary to previous results from the literature – agarose and calcium alginate did not behave similarly with respect to corrosion on a mild steel surface. Agarose decreased the measured rate of corrosion, while calcium alginate increased it. Additionally, the addition of an underlying iron sulfide film beneath these gels did not alter this behavior significantly.

From the work conducted in Chapter 3, it was found that two different forms of iron sulfide could be formed on mild steel coupons by simply varying the concentration of the sulfide in the solution in which these coupons were submerged. At below approximately 100 ppm sulfide concentration, a loose black corrosion product formed. Through a combination of x-ray diffraction and Raman spectroscopy, it was found that this product consisted of a mixture of several types of iron sulfides. Intriguingly, the identity of these iron sulfides seemed to change either with the drying history of the coupon or with the heating of the coupon, depending upon the effect the Raman laser had. Initially, Raman spectroscopy detected a mixture of greigite and marcasite, but heating and/or drying induced by the Raman laser altered the sample such that other iron sulfides were detected depending upon the power of the laser. At intermediate power, a mixture of pyrite, pyrrhotite, and marcasite was detected. At high power, mackinawite was detected. At above approximately 100 ppm sulfide concentration, an adherent golden-colored corrosion product formed. Attempts to identify this material using a variety of tools failed to return conclusive results.

From the work conducted in the Chapter 4, it was shown that the corrosion

morphology differed qualitatively between coupons that were corroded abiotically in an inorganic sulfide solution and coupons that were corroded biotically by an active culture of sulfate-reducing bacteria (SRB). Additionally, it was found that the SRB biofilm was similar to the calcium alginate biogel, in that both increased the corrosion current density. Moreover, lysing the bacteria had little effect on this increase in corrosion rate, implying that biofilm contributed strongly to the corrosion rate.

5.2 Contributions

The work contained within this thesis provided several novel contributions and observations. It was shown that an agarose gel decreased the rate of corrosion on a mild steel surface and that a calcium alginate gel increased it. This is contrary to previously published results by Roe et al. [43]. Moreover, it was shown that an SRB biofilm displayed an effect similar to that of calcium alginate. This provides further clues in regards to the mechanisms of MIC.

A novel method for the development of iron sulfide thin films was also developed. It was observed that both the phase and morphology of the resulting iron sulfide depended upon sulfide concentration, with sulfide concentration below 100 ppm forming a loose black corrosion product while sulfide concentrations above 100 ppm forming an adherent golden-colored corrosion product.

The black corrosion product was observed to change in composition depending upon the intensity of a laser beam that was applied to it during Raman spectroscopy, a phenomenon that does not appear to exist in the literature. Upon increasing the power of the laser beam, a mixture of greigite and marcasite was observed to change irreversibly into a mixture of pyrite, pyrrhotite, and marcasite; further increasing the power caused an irreversible change into mackinawite. This transformation into mackinawite is contrary to existing knowledge regarding the various iron sulfides: it is known that mackinawite is the precursor form for other iron sulfides, not vice versa.

5.3 Direction for Future Work

Many open questions remain with respect to the work conducted in this thesis. In Chapter 2, it was shown that calcium alginate enhanced the rate of corrosion while agarose decreased it. Several possible mechanisms were proposed in order to explain this observation, but further experiments will be required in order to identify the

correct mechanism. Electrochemical impedance spectroscopy (EIS) could provide a valuable tool in understanding the mechanisms involved. EIS consists of applying an alternative voltage to the working electrode in an electrochemical cell. By sweeping across a range of frequencies, insight into the capacitive properties of the electrode and its associated electrical double layer can be obtained. The limiting step in the electrochemical reaction could be found using this method: diffusion limitations can be distinguished from capacitive or resistive limitations, for example. Specifically, the measured impedance is plotted on the complex plane in a Nyquist diagram, and the shape of these diagrams can give mechanistic information regarding the reactions involved (Figure ??).

In Chapter 3, the identity of the black corrosion product was found to be a mixture of several iron sulfide phases through a combination of many techniques, mainly x-ray diffraction and Raman spectroscopy. The identity of the gold corrosion product, however, remains an open question. Attempts to identify it using a wide variety of techniques have all failed – further innovation here would be required. Additionally, many question remain regarding the iron sulfide development process itself. For example, why is there a phase change from the black corrosion product to the gold at a sulfide concentration of approximately 100 ppm? Also, why is it that the speed of development for the gold corrosion product inversely related to the sulfide concentration? At very high sulfide concentration (500 ppm and above), it took several weeks for the gold colored corrosion product to form. Speculation as to the cause of these observations were discussed in Chapter 3, but experiments will be required in order to validate or refute them. Moreover, these films consistently failed to develop on the much smaller steel surface of the working electrodes – new ideas and experiments will be required to find out why.

In Chapter 4, it was shown that SRB biofilms had a corrosive effect that is similar to calcium alginate, but further experiments will be required to concretely test these similarities. For example, does the SRB biofilms have the ability to bind metal ions like calcium alginate? Since active corrosion was not observed on the steel surface of the working electrode, the SRB biofilms that were used remained transparent and difficult to observe. Further work will be required to investigate the nature of this biofilm. Also, it is possible that the biofilm may have protected the bacteria within it from the lysing procedure – experiments will be required in order to investigate various methods for lysing bacteria within a biofilm and verifying their efficacy. For the experiments used in this thesis, it was assumed that the bacteria were lysed by the Alconox solution. Verification of this supposition of cell death is required.

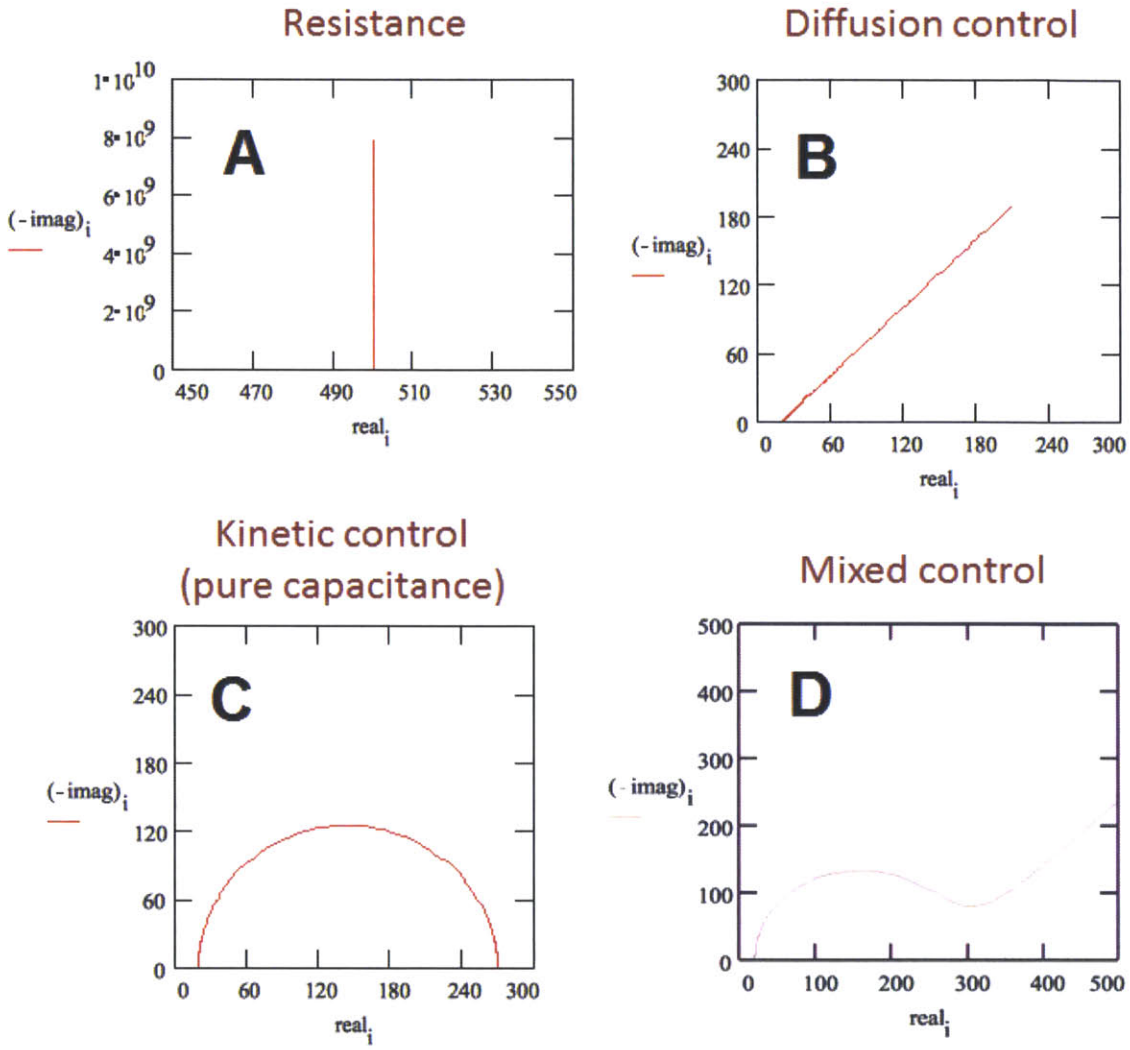

Figure 5-1: Example of the type of information that can be gained from electrochemical impedance spectroscopy (EIS). The measured impedance is plotted on the complex plane in a Nyquist diagram, and the shape of this diagram decribes the rate-limiting step in the electrochemical cell. A) A vertical line indicates pure resistance, either from the electronics or from the electrolyte solution. B) A diagonal line indicates that the diffusion of reactants or products from the electrode is the rate-limiting factor. C) A semi-circle indicates that the rate-limiting step is the kinetics of the electrochemical reaction occuring on the surface on the electrode. D) It's possible that a particular reaction can be limited by more than one factor as shown here in the mixed control pattern.

Appendix A

Mass Loss Method for Measuring Corrosion

Mass loss is the traditional method for measuring corrosion, but these corrosion experiments typically required a time span of several months and involved vigorous cleaning and harsh chemicals to dissolve off the accumulated corrosion products.

In the experiments attempted, the measurements were uniformly ruined by water that somehow adhered onto and into the samples tested and the epoxy that protected the sample. After nominally drying, the mass would continue to drop over time. As such, mass measurements taken on these samples did not represent the actual dry mass of the sample. Attempts to hasten drying of the samples using elevated temperatures instead destabilized the epoxy, releasing a noxious fume and causing its mass to also drop.

Appendix B

Example of a Full Set of Potentiostatic Measurements

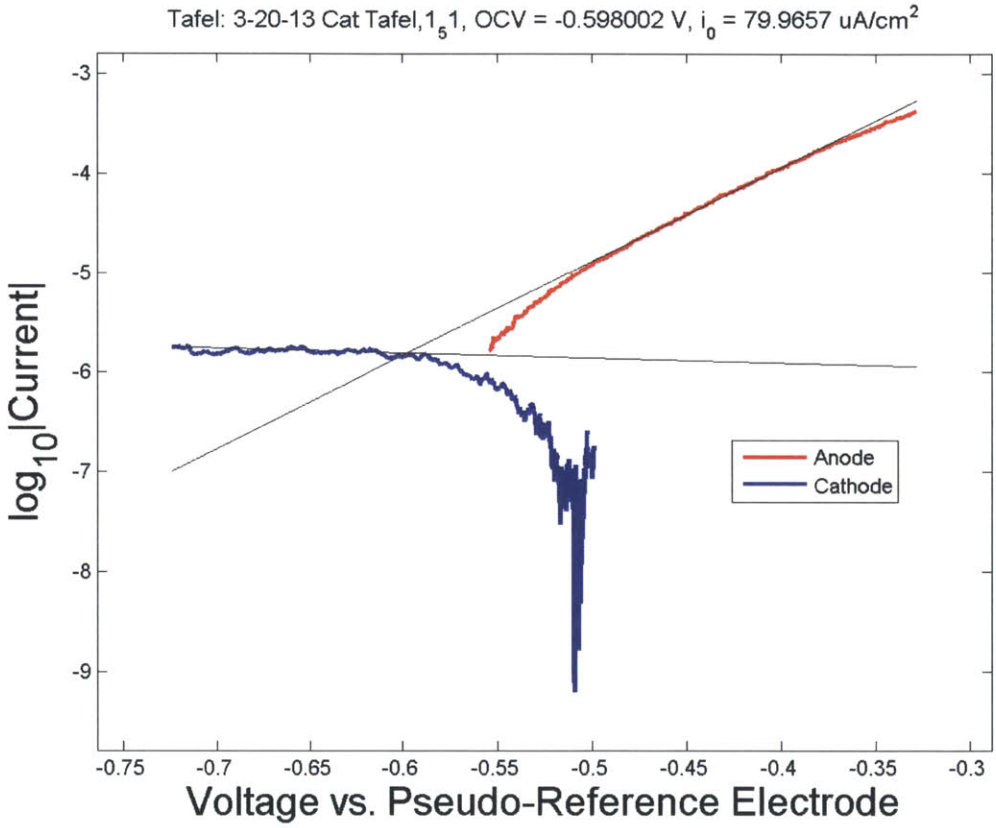

Figure B-1: Compared to the rest of the measurements taken, the one here is vastly different. This is a systematic behavior of the potentiostatic experiments.

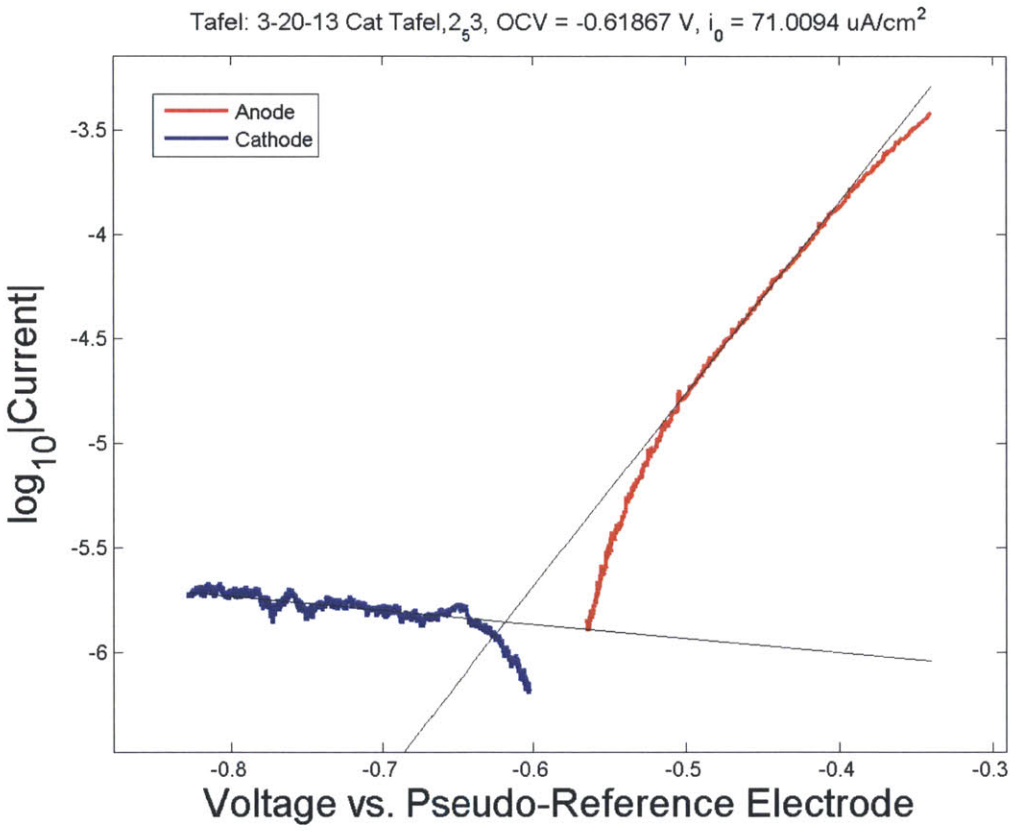

Figure B-2: Second measurement.

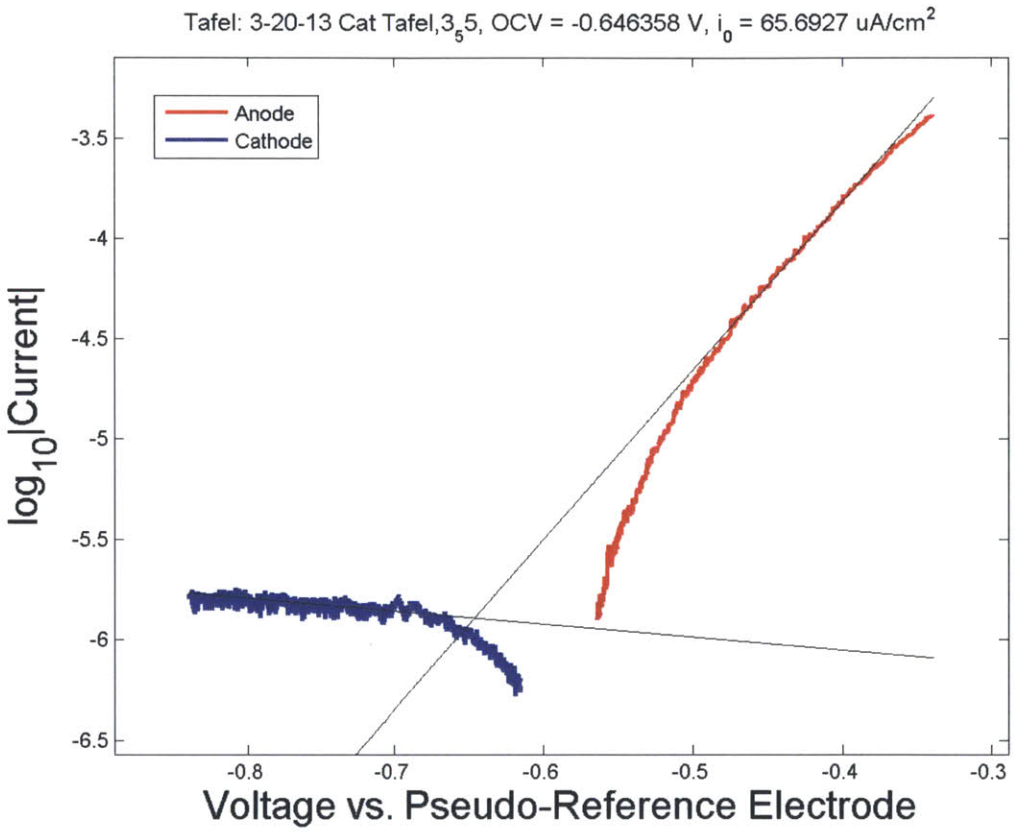

Figure B-3: Third measurement.

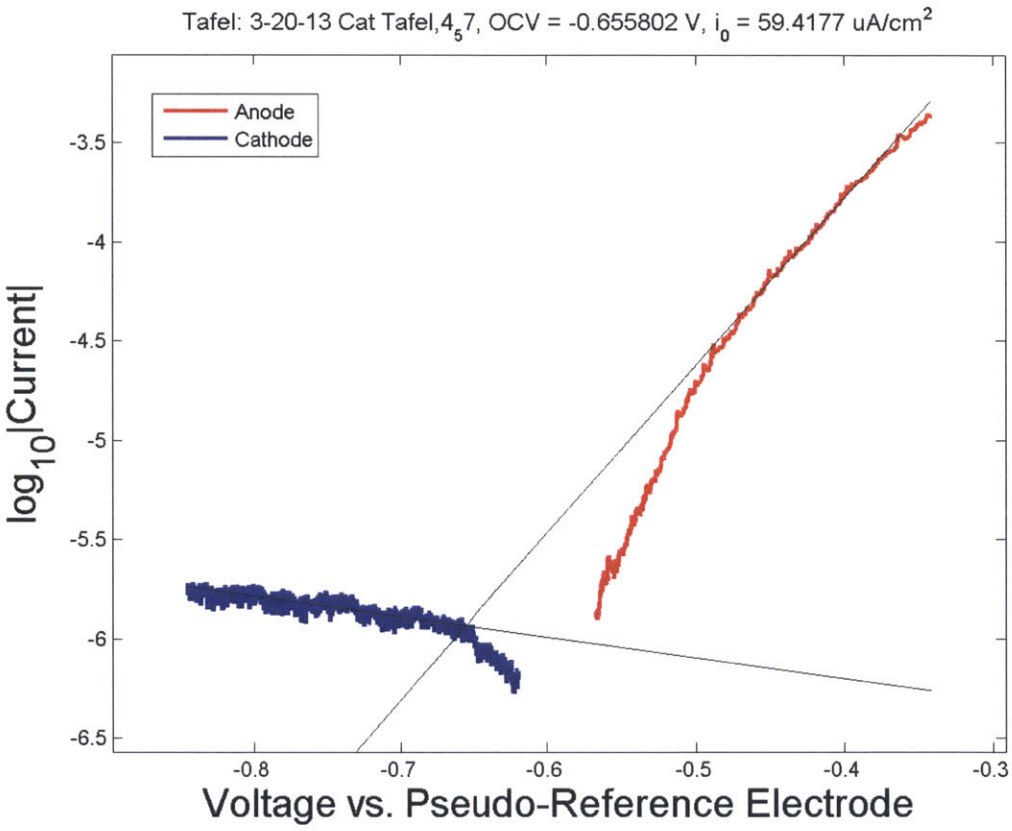

Figure B-4: Fourth measurement.

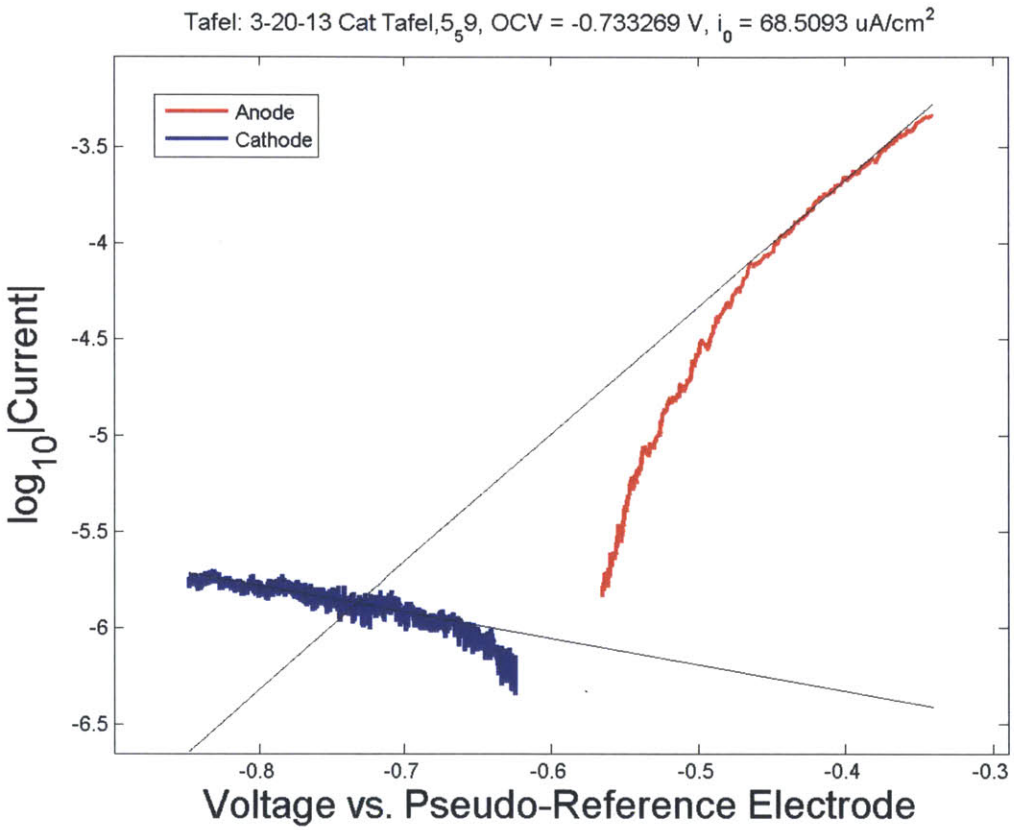

Figure B-5: Fifth measurement.

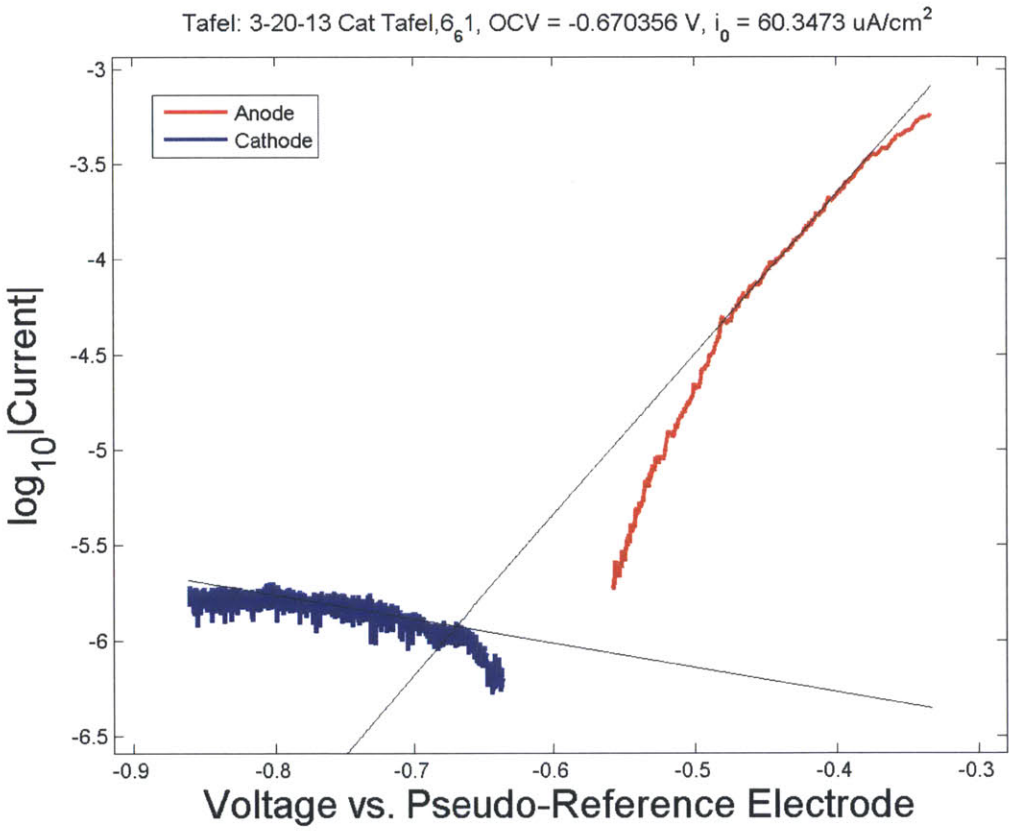

Figure B-6: Sixth measurement.

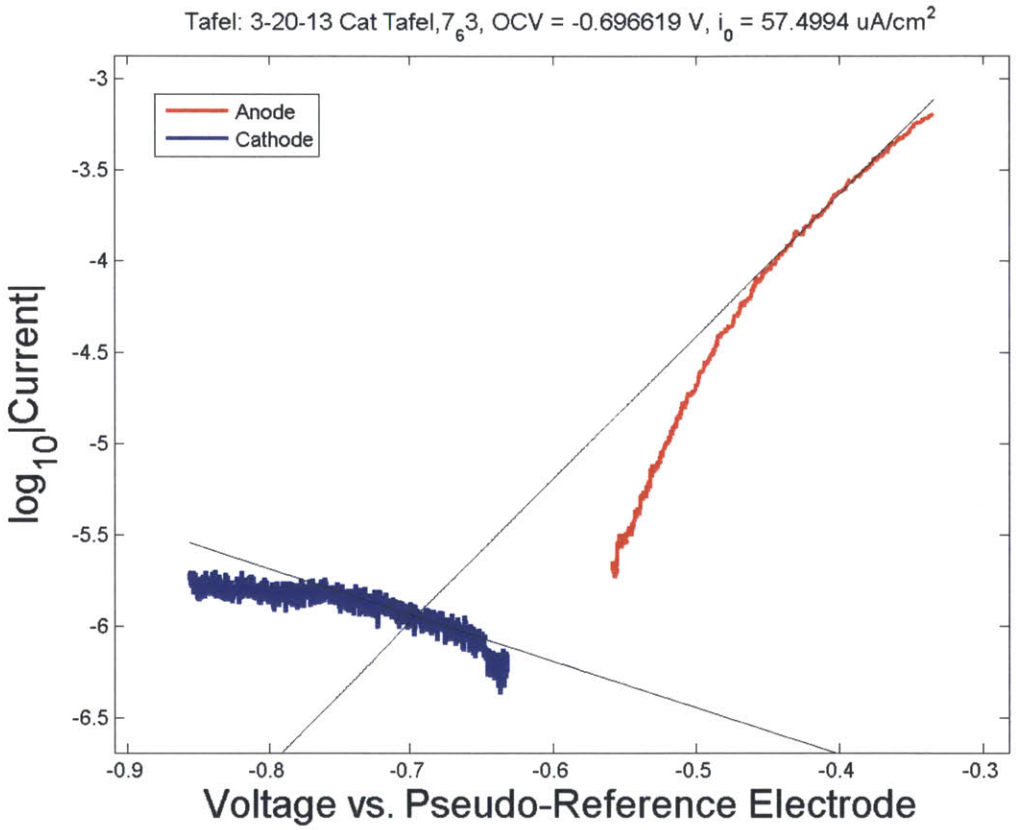

Figure B-7: Seventh measurement.

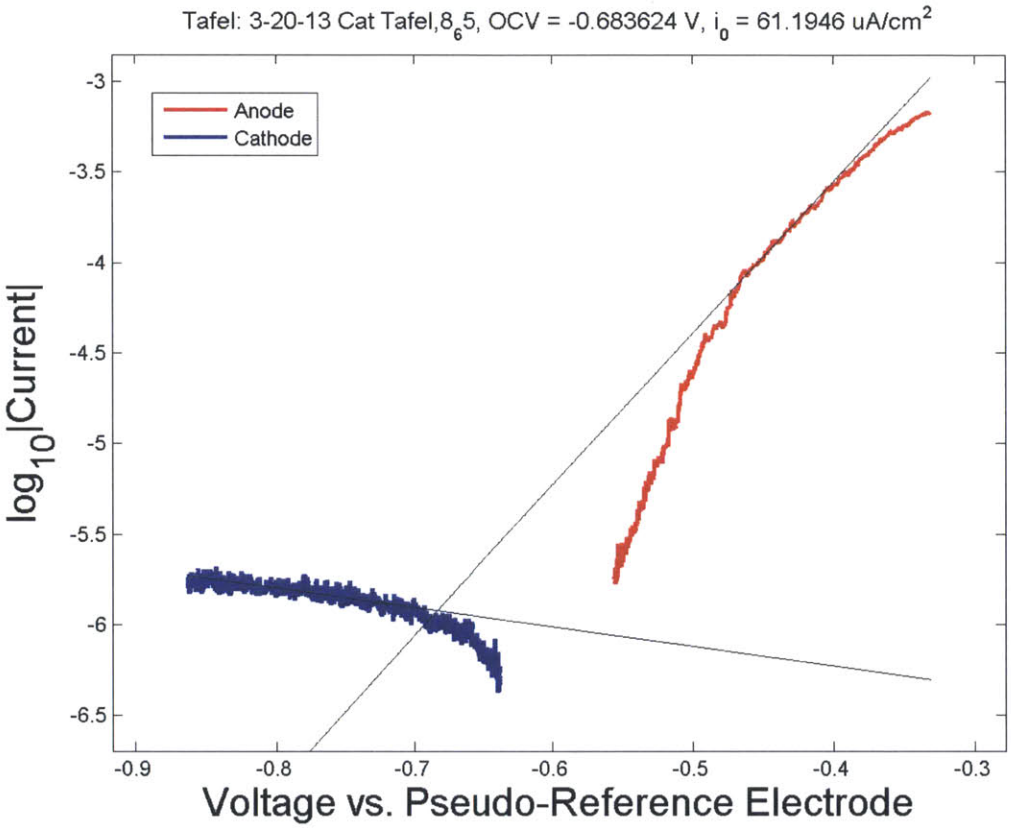

Figure B-8: Eighth measurement.

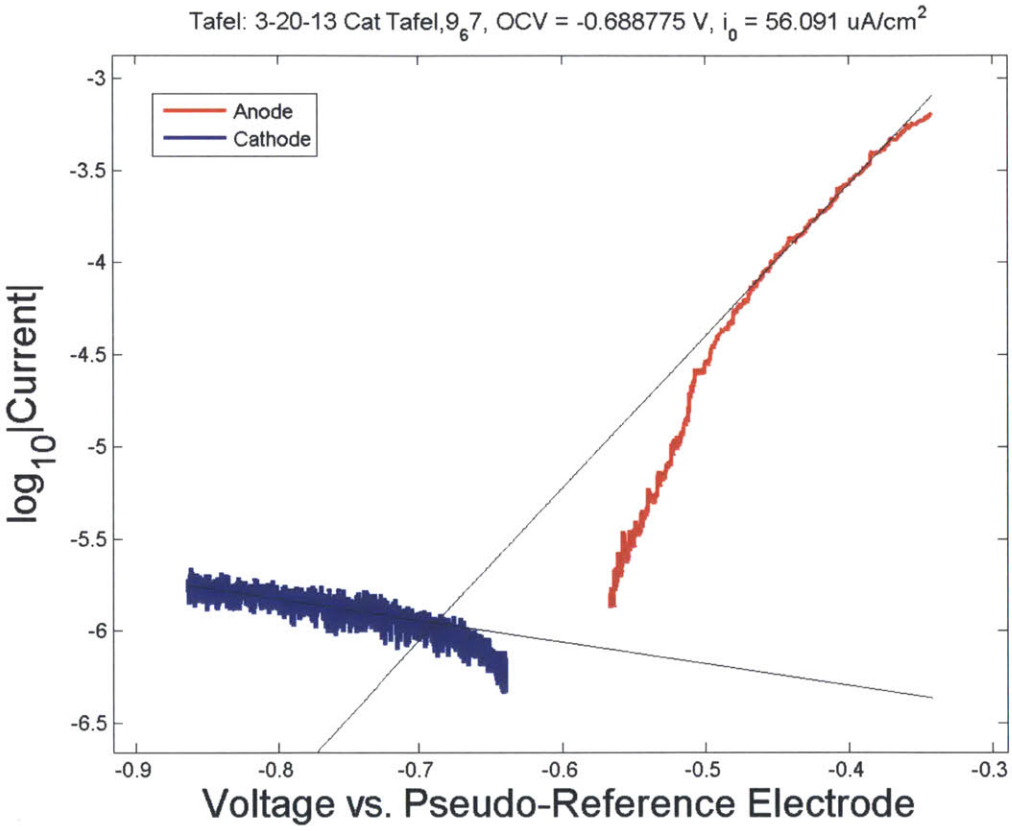

Figure B-9: Ninth measurement.

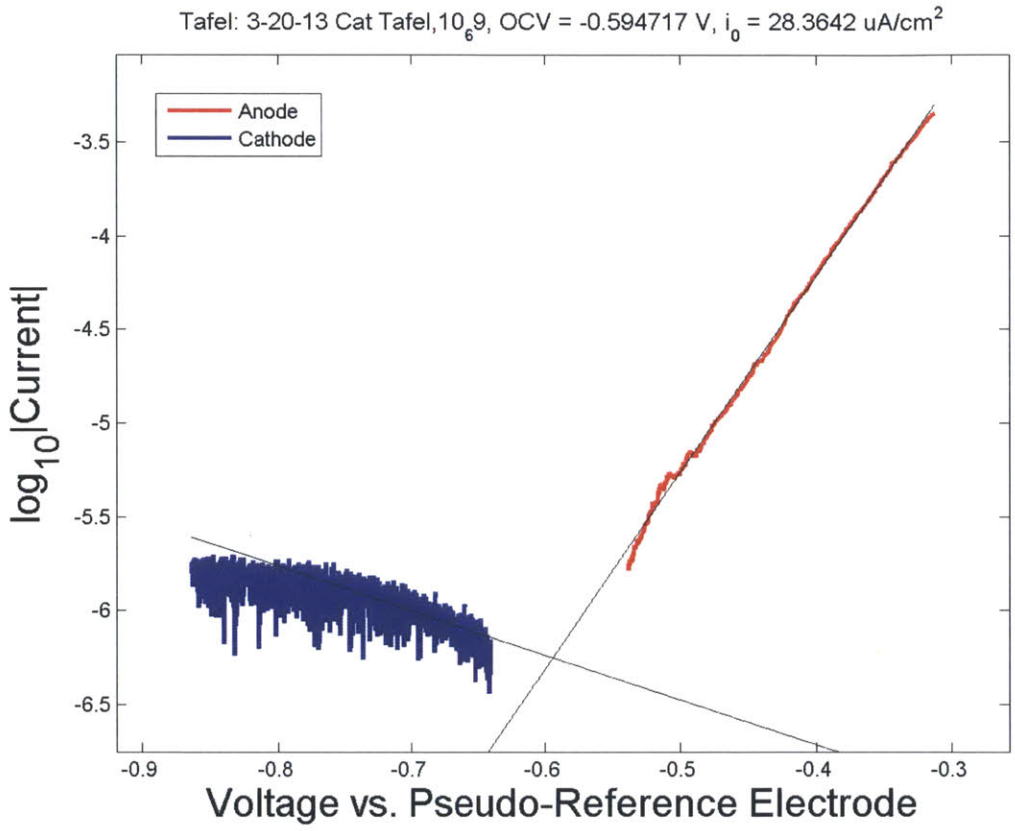

Figure B-10: Tenth measurement. The measured exchange current in this one is significantly different from the others, but aside from that there is no reason to exclude this measurement.

Appendix C

Differential Interference Contrast Images of Iron Sulfide Corrosion Products at Higher Magnifications

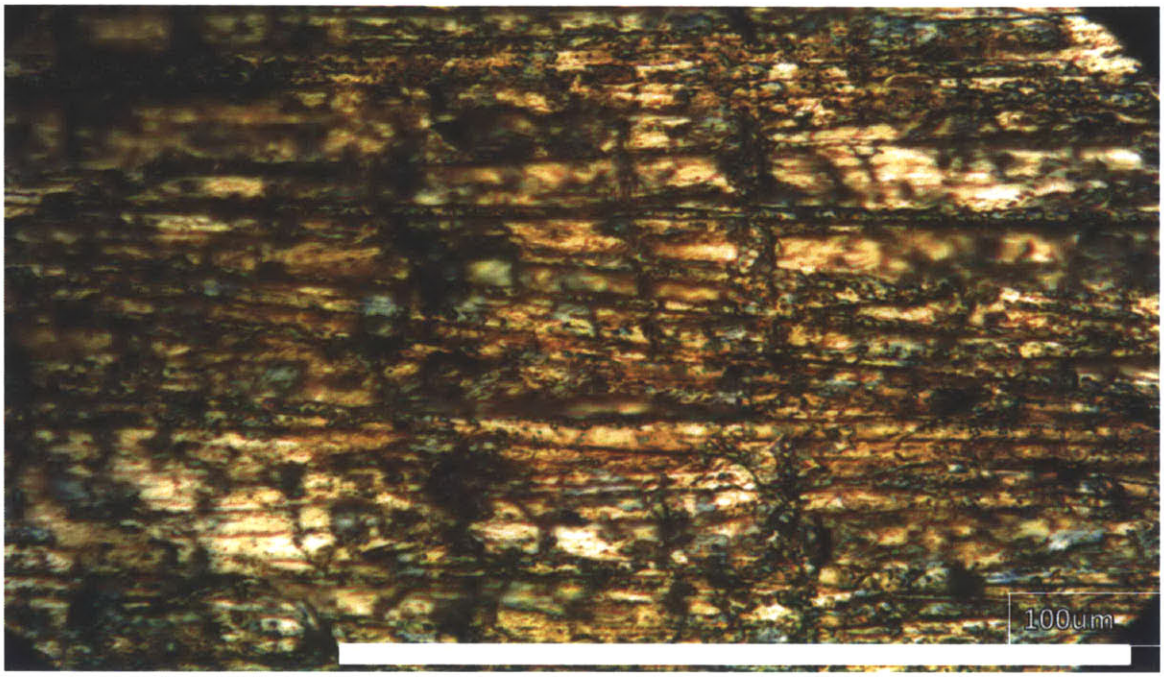

Figure C-1: This image of untreated steel was taken using differential interference contrast (DIC) and are not necessarily real colored. Images were taken at 900x magnification; scale bars are 100 μm.

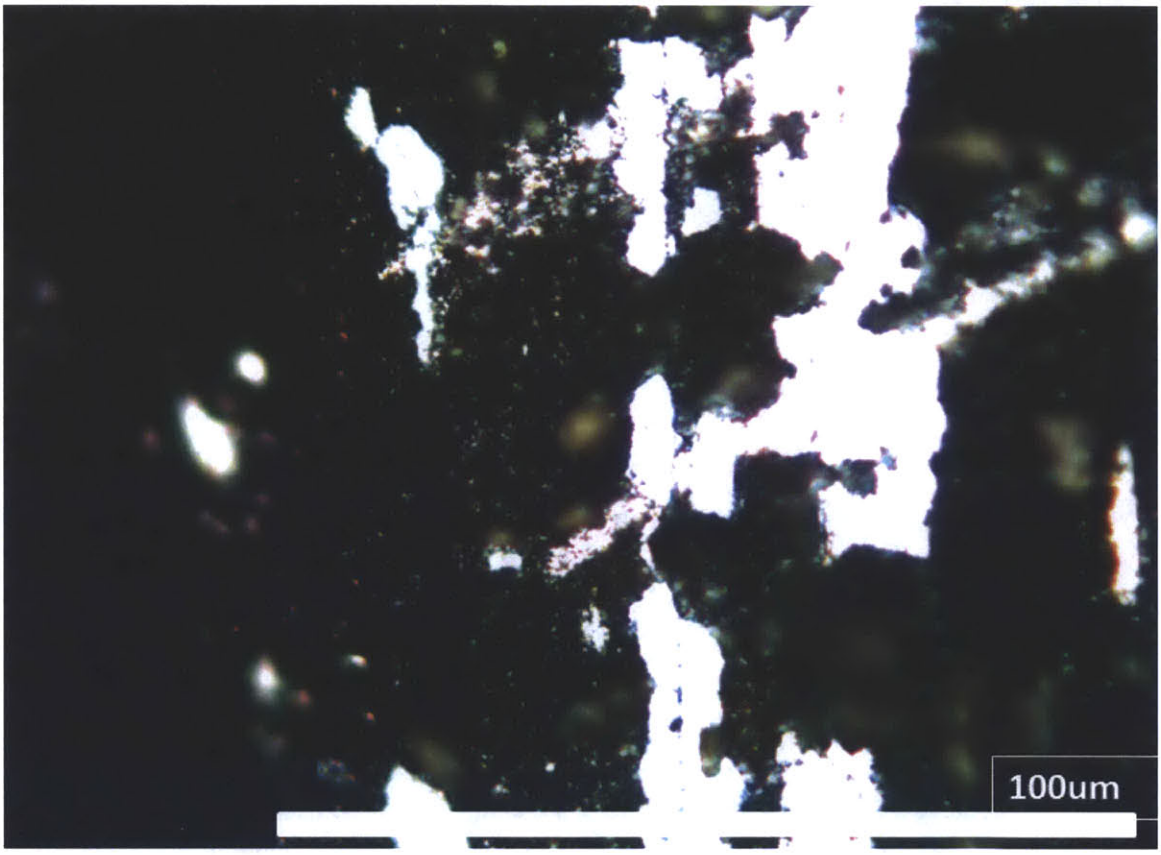

Figure C-2: This image of the black corrosion product was taken using differential interference contrast (DIC) and are not necessarily real colored. Images were taken at 900x magnification; scale bars are 100 μm.

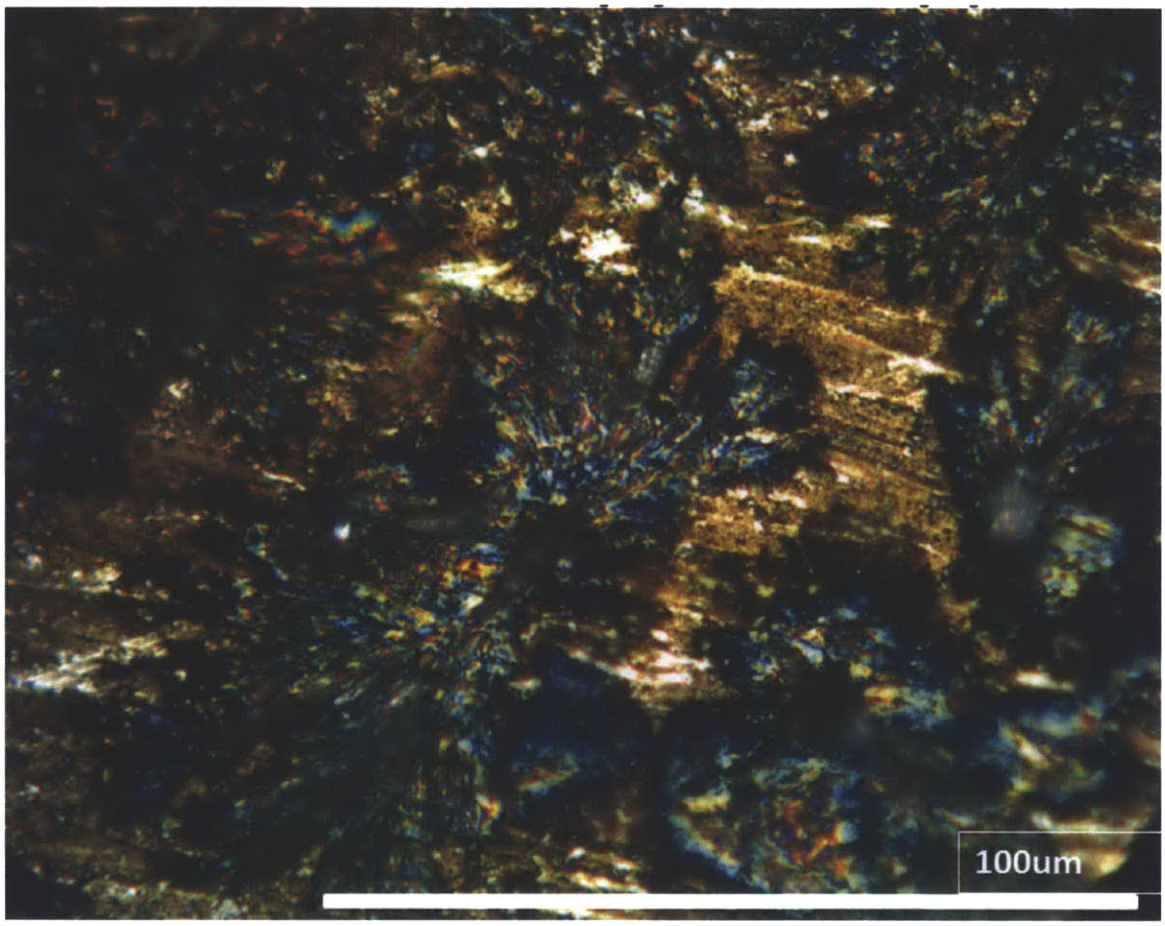

Figure C-3: This image of the gold corrosion product was taken using differential interference contrast (DIC) and are not necessarily real colored. Images were taken at 900x magnification; scale bars are 100 μm.

Appendix D

Raman Spectra from Literature

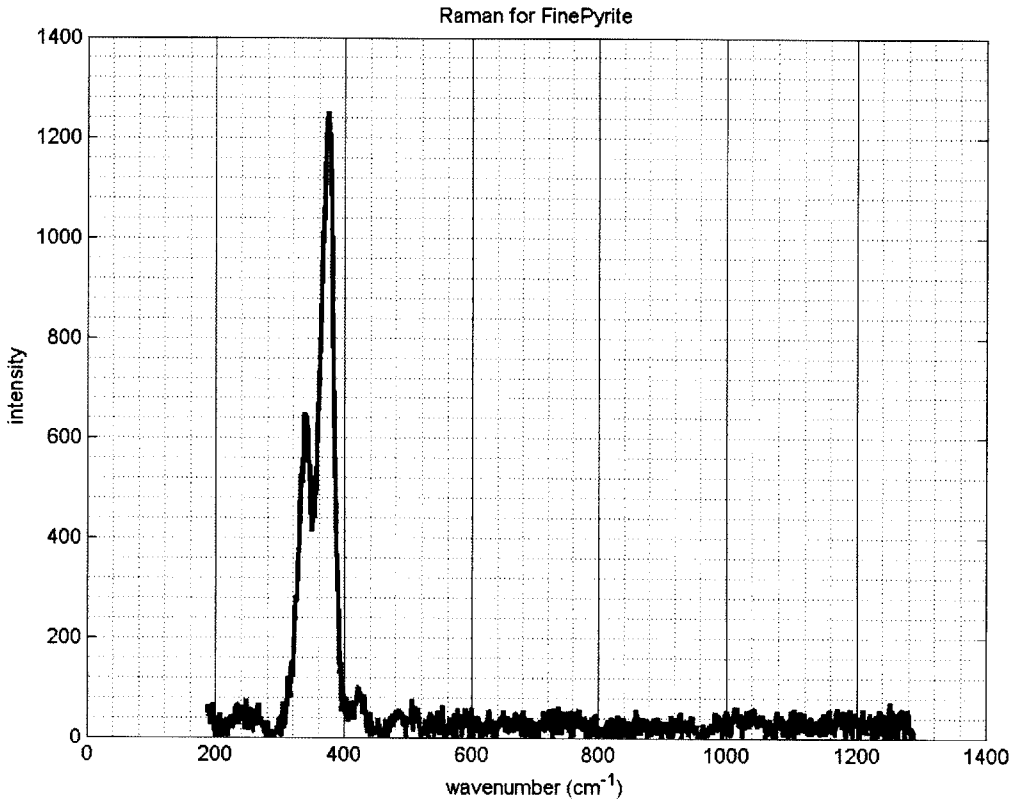

Figure D-1: Raman spectra for pyrite from the RRUFF Project, ID R070692. This sample was described as "extremely fine-grained".

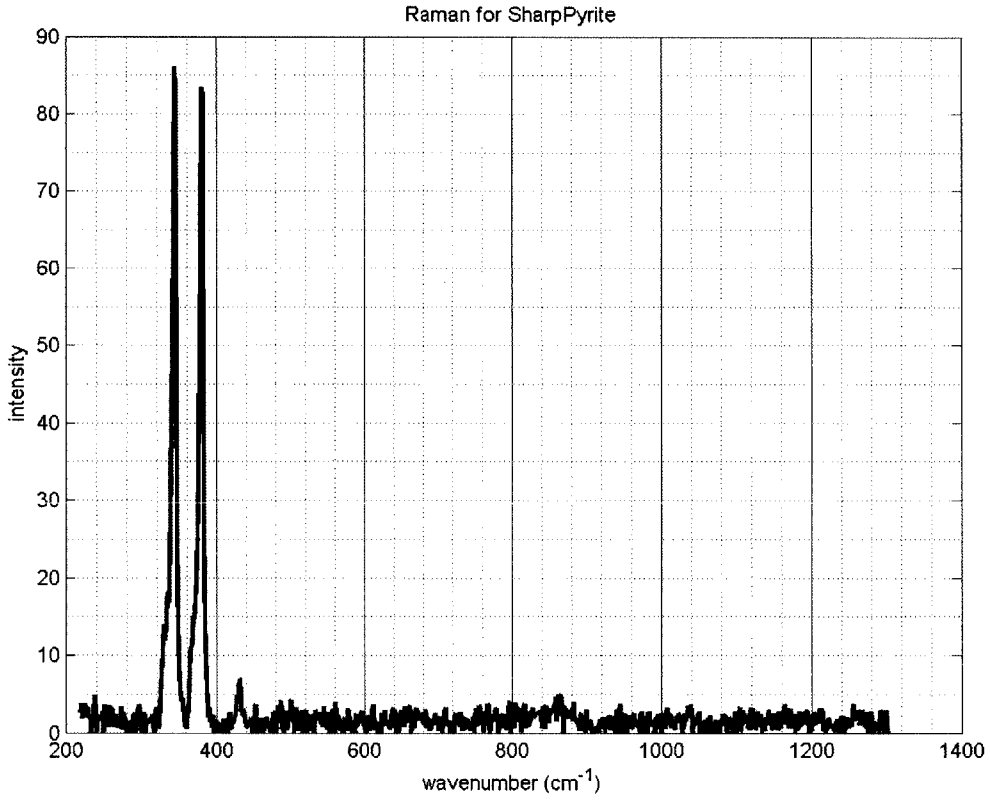

Figure D-2: Raman spectra for pyrite from the RRUFF Project, ID R100166. This sample displays the typical sharp double peaks expected of pure pyrite.

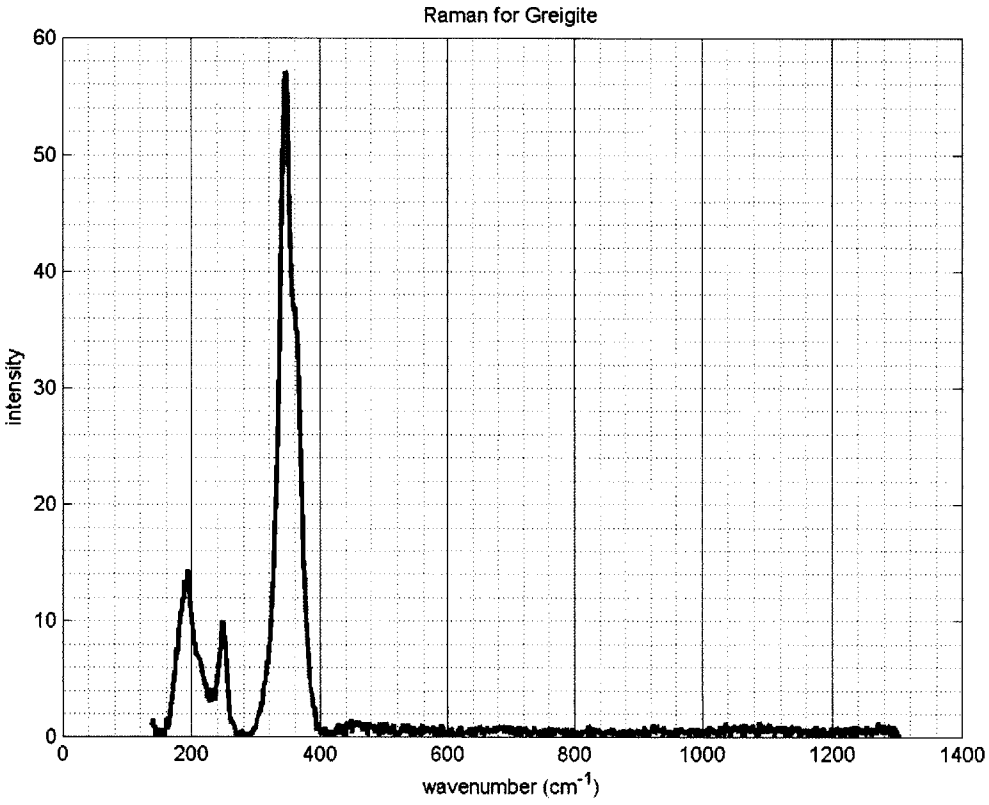

Figure D-3: Raman spectra for greigite from the RRUFF Project, ID R120103.

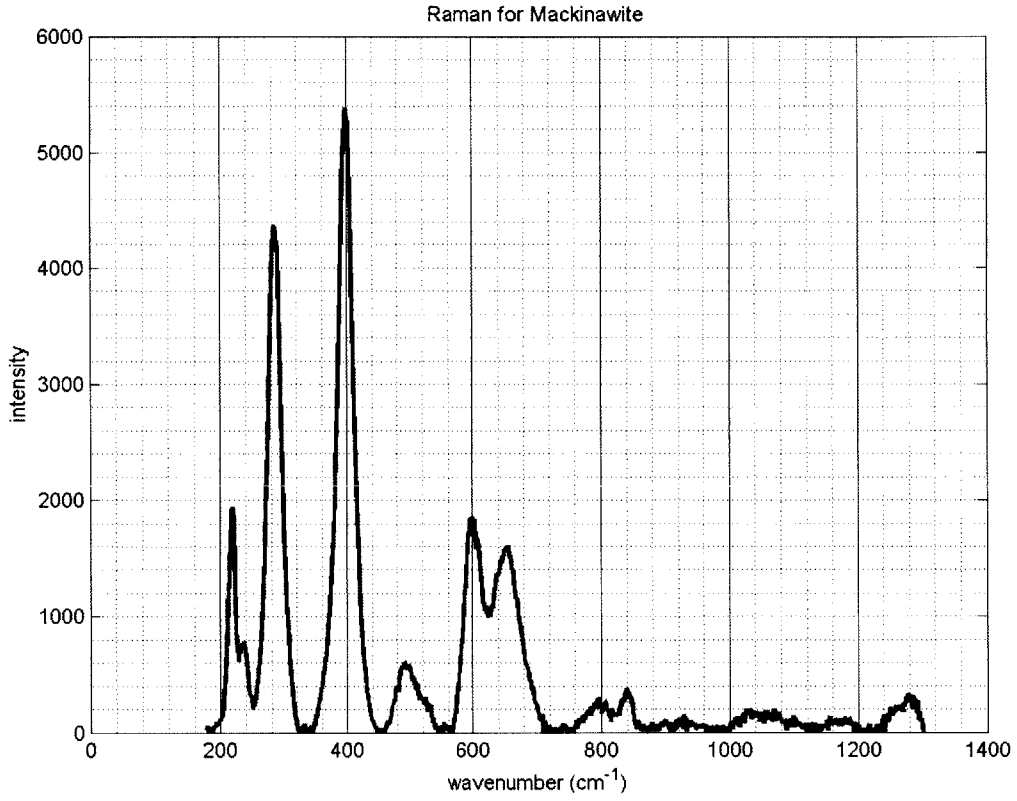

Figure D-4: Raman spectra for mackinawite from the RRUFF Project, ID R060388.

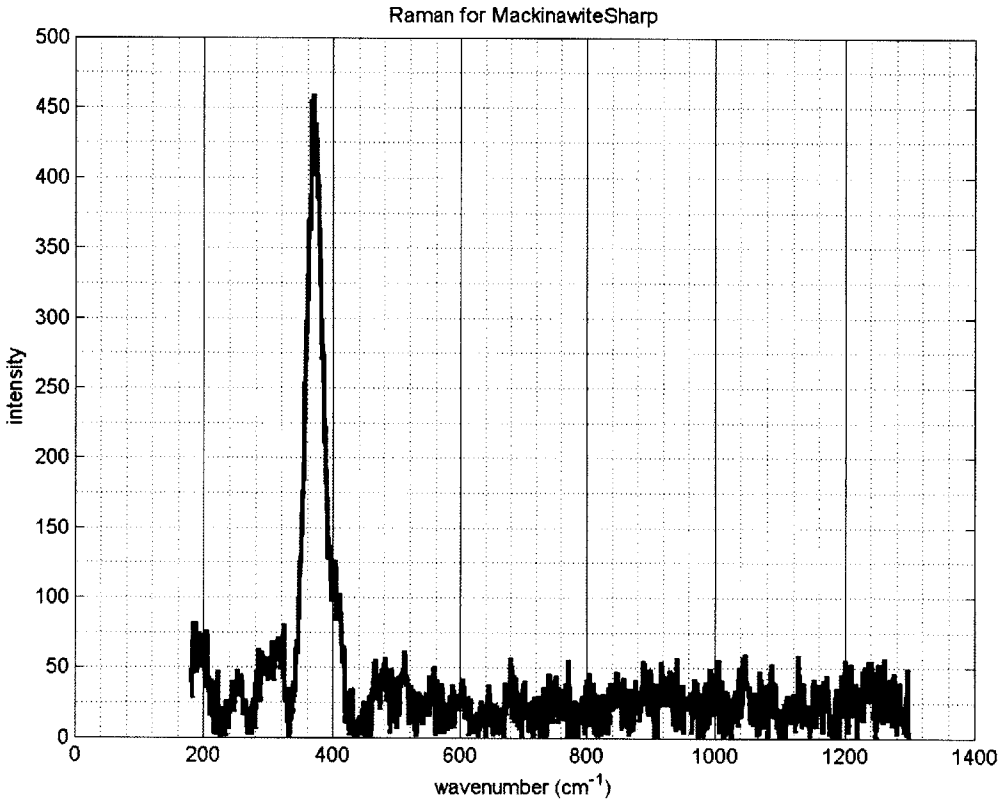

Figure D-5: Raman spectra for mackinawite from the RRUFF Project, ID R070302. This spectra shows only one peak, and this peak was also represented in the other mackinawite spectra. Since the RRUFF Project only had two mackinawite spectra in its database, this one was included for completion.

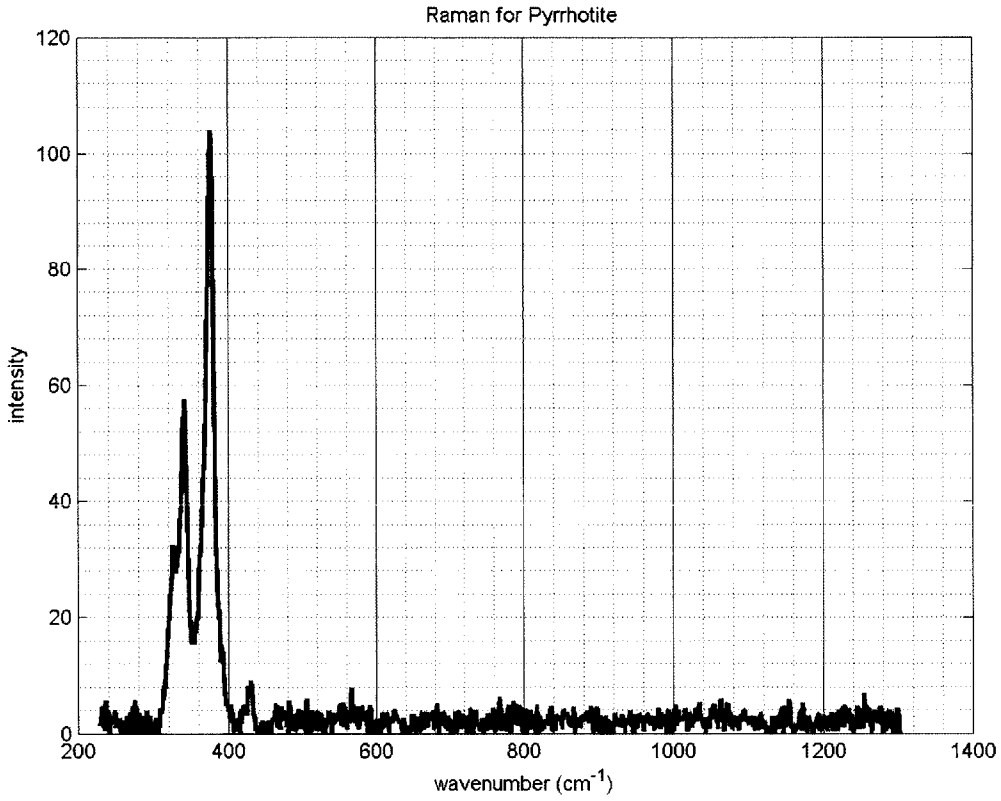

Figure D-6: Raman spectra for pyrrhotite from the RRUFF Project, ID R060440. The other pyrrhotite spectra in the database was excluded since it was very noisy.

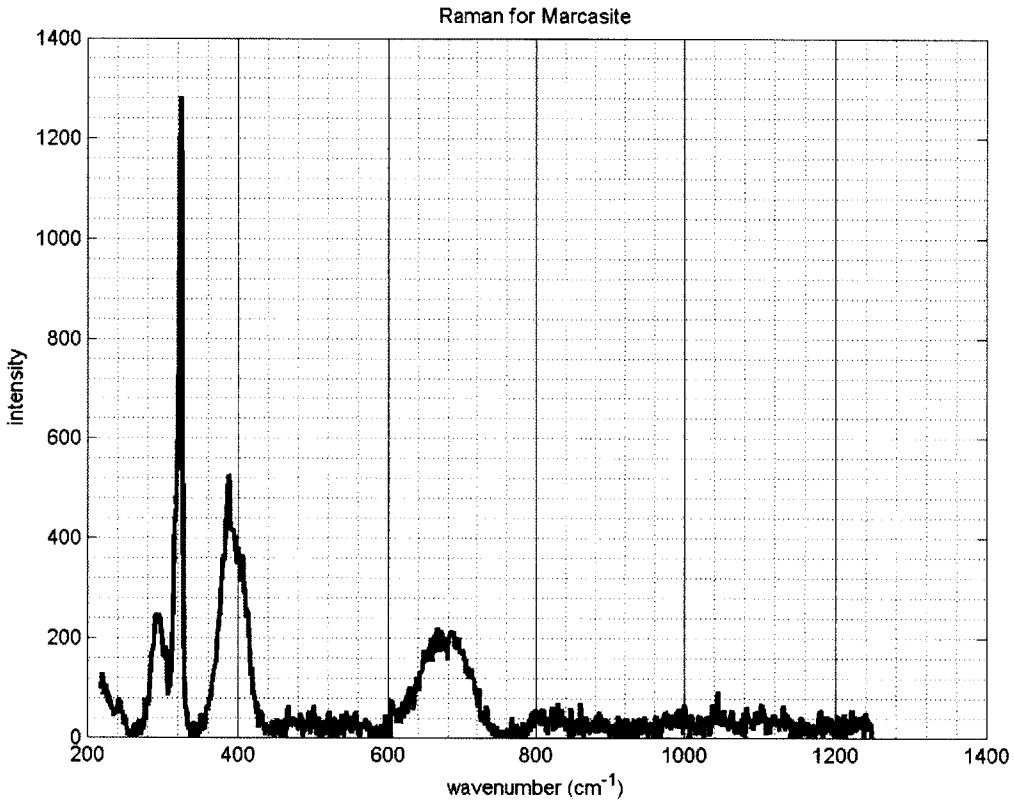

Figure D-7: Raman spectra for marcasite from the RRUFF Project, ID R060882.

Appendix E

Procedure for Making Modified Baar's Medium for Sulfate Reducers

The pH of each component (Table E.1) was adjusted to 7.5 using a Ag/AgCl pH sensor and stock solutions of 1 M HCl and 1 M NaOH. Each component was autoclaved. The three components were mixed inside the anaerobic glovebox in an atmosphere of 90% nitrogen, 5% hydrogen, and 5% carbon dioxide. A 3% stock solution of cysteine, 0.1 mL for each 5-10 mL of media, was added to the hot media. The media was capped tightly to exclude oxygen and stored at 4^{o}C.

Table E.1: Recipe for Modified Baar's Medium for Sulfate Reducers

Component I	
Magnesium Sulfate	2.0g
Sodium Citrate	5.0g
Calcium Sulfate	1.0g
Ammonia Chloride	1.0g
Distilled water	400.0mL
Component II	
Potassium Phosphate Dibasic	0.5g
Distilled Water	200.0mL
Component III	
Sodium Lactate	3.5g
Yeast Extract	1.0g
Distilled Water	400.0mL

Bibliography

[1] R. Javaherdashti, "Impact of sulphate-reducing bacteria on the performance of engineering materials," *Appl. Microbiol. Biotechnol.*, vol. 91, no. 6, pp. 1507–1517, 2011.

[2] T. Rao, *Microbial Fouling and Corrosion: Fundamentals and Mechanisms*, ch. 6, pp. 95–126. Springer US, 2012.

[3] R. George, "Current understanding and future approaches for controlling microbially influenced concrete corrosion: A review," *Concr. Res. Lett.*, vol. 3, no. 3, 2012.

[4] G. Abraham, V. Kain, and G. Dey, "Mic failure of type 316l seawater pipeline," *Mater. Perform.*, vol. 48, no. 1, pp. 64–69, 2009.

[5] F. Yu, J. Dillon, and T. Henry, "Identification and control of microbiologically influenced corrosion in a power plant," *Corrosion 2010*.

[6] M. Egan, "Internal corrosion suspected as cause of alaskan pipeline leak," *Mater. Perform.*, vol. 50, no. 5, pp. 14–23, 2011.

[7] G. Voordouw, A. A. Grigoryan, A. Lambo, S. Lin, H. S. Park, T. R. Jack, D. Coombe, B. Clay, F. Zhang, R. Ertmoed, K. Miner, and J. J. Arensdorf, "Sulfide remediation by pulsed injection of nitrate into a low temperature canadian heavy oil reservoir," *Environ. Sci. Technol.*, vol. 43, no. 24, pp. 9512–9518, 2009.

[8] S. Maruthamuthu, B. D. Kumar, S. Ramachandran, B. Anandkumar, S. Palanichamy, M. Chandrasekaran, P. Subramanian, and N. Palaniswamy, "Microbial corrosion in petroleum product transporting pipelines," *Ind. Eng. Chem. Res.*, vol. 50, no. 13, pp. 8006–8015, 2011.

[9] I. B. Beech, C. Sunny Cheung, C. Patrick Chan, M. A. Hill, R. Franco, and A.-R. Lino, "Study of parameters implicated in the biodeterioration of mild steel in the presence of different species of sulphate-reducing bacteria," *Int. Biodeterior. Biodegrad.*, vol. 34, no. 3, pp. 289–303, 1994.

[10] I. B. Beech and J. Sunner, "Biocorrosion: towards understanding interactions between biofilms and metals," *Curr. Opin. Biotechnol.*, vol. 15, no. 3, pp. 181–186, 2004.

[11] K. Li, M. Whitfield, and K. J. Van Vliet, "Beating the bugs: roles of microbial biofilms in corrosion," *Corrosion Reviews*, vol. 31, pp. 73–84, 2013.

[12] L. Thomas and Y. Chung, "Comparison of mic pit morphology with chloride induced pits in types 304/304l/e308 stainless steel base metal/welds," *Corrosion 99*, 1999.

[13] B. Little, R. Ray, P. Wagner, J. Jones-Meehan, C. Lee, and F. Mansfeld, "Spatial relationships between marine bacteria and localized corrosion on polymer coated steel," *Biofouling*, vol. 13, no. 4, pp. 301–321, 1999.

[14] R. D. Bryant, W. Jansen, J. Boivin, E. J. Laishley, and J. W. Costerton, "Effect of hydrogenase and mixed sulfate-reducing bacterial populations on the corrosion of steel," *Appl. Environ. Microbiol.*, vol. 57, no. 10, pp. 2804–2809, 1991.

[15] R. King, J. Miller, and D. Wakerley, "Corrosion of mild steel in cultures of sulphate-reducing bacteria: effect of changing the soluble iron concentration during growth," *Br. Corros. J.*, vol. 8, no. 2, pp. 89–93, 1973.

[16] B. Vu, M. Chen, R. Crawford, and E. Ivanova, "Bacterial extracellular polysaccharides involved in biofilm formation," *Molecules*, vol. 14, no. 7, pp. 2535–2554, 2009.

[17] N. Fernandez, E. E. Diaz, R. Amils, and J. L. Sanz, "Analysis of microbial community during biofilm development in an anaerobic wastewater treatment reactor," *Microb. Ecol.*, vol. 56, no. 1, pp. 121–132, 2008.

[18] M. S. Johnson, I. B. Zhulin, M. Gapuzan, and B. L. Taylor, "Oxygen-dependent growth of the obligate anaerobe desulfovibrio vulgaris hildenborough," *J. Bacteriol.*, vol. 179, no. 17, pp. 5598–5601, 1997.

[19] R. Prasad, "Assessment and control of mic in the oil industry in the 20th century," *Corrosion 2000*, 2000.

[20] A. Rajasekar, B. Anandkumar, S. Maruthamuthu, Y. Ting, and P. Rahman, "Characterization of corrosive bacterial consortia isolated from petroleum-product-transporting pipelines," *Appl. Microbiol. Biotechnol.*, vol. 85, no. 4, pp. 1175–1188, 2009.

[21] T. Thorstenson, T. Torsvik, J. Beeder, B.-L. Lillebo, E. Sunde, and G. Bodtker, "Biocide replacement by nitrate in sea water injection systems," *Corrosion 2002*, 2002.

[22] J. Mohanakrishnan, M. Kofoed, J. Barr, Z. Yuan, A. Schramm, and R. Meyer, "Dynamic microbial response of sulfidogenic wastewater biofilm to nitrate," *Appl. Microbiol. Biotechnol.*, vol. 91, no. 6, pp. 1647–1657, 2011.

[23] A. J. Sedriks, "Corrosion of stainless steel, 2," 1996.

[24] I. B. Beech and C. C. Gaylarde, "Recent advances in the study of biocorrosion: an overview," *Rev. Microbiol.*, vol. 30, no. 3, pp. 117–190, 1999.

[25] C. von Wolzogen Kuehr and L. Van der Vlugt, "Graphitization of cast iron as an electrobiochemical process in anaerobic soils," tech. rep., DTIC Document, 1964.

[26] J. Stott, "What progress in the understanding of microbially induced corrosion has been made in the last 25 years? a personal viewpoint," *Corros. Sci.*, vol. 35, no. 1, pp. 667–673, 1993.

[27] R. Cord-Ruwisch, "Mic in hydrocarbon transportation systems," *Corros. Australas.*, vol. 21, pp. 8 11, 1996.

[28] S. Da Silva, R. Basséguy, and A. Bergel, "The role of hydrogenases in the anaerobic microbiologically influenced corrosion of steels," *Bioelectrochemistry*, vol. 56, no. 1, pp. 77 79, 2002.

[29] J.-L. Crolet, "From biology and corrosion to biocorrosion," *Oceanol. Acta*, vol. 15, no. 1, pp. 87–94, 1992.

[30] W. Iverson and G. Olson, "Anaerobic corrosion by sulfate-reducing bacteria due to a highly-reactive volatile phosphorus compound. final report," tech. rep., National Bureau of Standards, Washington, DC (USA), 1983.

[31] I. Beech and C. S. Cheung, "Interactions of exopolymers produced by sulphate-reducing bacteria with metal ions," *Int. Biodeterior. Biodegrad.*, vol. 35, no. 1, pp. 59–72, 1995.

[32] R. Edyvean, I. BENSON, C. Thomas, I. Beech, and H. Videla, "Biological influences on hydrogen effects in steel in seawater," *Mater. Perform.*, vol. 37, no. 4, pp. 40–44, 1998.

[33] W. Lee and W. Characklis, "Corrosion of mild steel under anaerobic biofilm," *Corrosion*, vol. 49, no. 3, pp. 186–199, 1993.

[34] T. Rohwerder, T. Gehrke, K. Kinzler, and W. Sand, "Bioleaching review part a," *Appl. Microbiol. Biotechnol.*, vol. 63, no. 3, pp. 239–248, 2003.

[35] G. Booth and F. Wormwell, "Corrosion of mild steel by sulphate-reducing bacteria. effect of different strains of organisms," in *First International Congress on Metallic Corrosion*, pp. 341 4, 1961.

[36] G. Booth, P. Shinn, and D. Wakerley, "The influence of various strains of actively growing sulphate-reducing bacteria on the anaerobic corrosion of mild steel," in *Congres Int. de la Corrosion Marine et des Salissures, Cannes*, vol. 363, 1964.

[37] H. Bunker, "Microbiological experiments in anaerobic corrosion," *J. Soc. Chem. Ind*, vol. 58, p. 93, 1939.

[38] G. Booth, P. M. Cooper, and D. Wakerley, "Corrosion of mild steel by actively growing cultures of sulphate-reducing bacteria. the influence of ferrous iron," *Br. Corros. J.*, vol. 1, no. 9, pp. 345–349, 1966.

[39] G. Booth, A. Cooper, and P. Cooper, "Rates of microbial corrosion in continuous culture," *Chem. Ind.*, vol. 9, pp. 2084–2085, 1967.

[40] P. C. Singer, W. Stumm, *et al.*, "Acidic mine drainage: the rate-determining step.," *Science*, vol. 167, no. 3921, p. 1121, 1970.

[41] A. Rajasekar, B. Anandkumar, S. Maruthamuthu, Y.-P. Ting, and P. K. Rahman, "Characterization of corrosive bacterial consortia isolated from petroleum-product-transporting pipelines," *Appl. Microbiol. Biotechnol.*, vol. 85, no. 4, pp. 1175–1188, 2010.

[42] C. Picioreanu and M. C. van Loosdrecht, "A mathematical model for initiation of microbiologically influenced corrosion by differential aeration," *J. Electrochem. Soc.*, vol. 149, no. 6, pp. B211–B223, 2002.

[43] F. Roe, Z. Lewandowski, and T. Funk, "Simulating microbiologically influenced corrosion by depositing extracellular biopolymers on mild steel surfaces," *Corrosion*, vol. 52, no. 10, pp. 744–752, 1996.

[44] D. Rickard and G. W. Luther III, "Chemistry of iron sulfides," *Chem. Rev.*, vol. 38, no. 19, 2007.

[45] O. Cwalina and Z. Dzierzewicz, "The influence of sulfur oxy-anions on the rate of biocorrosion of metals," *Eur. Fed. Corros. Publ.*, vol. 29, pp. 47–52, 1999.

[46] H. Ma, X. Cheng, G. Li, S. Chen, Z. Quan, S. Zhao, and L. Niu, "The influence of hydrogen sulfide on corrosion of iron under different conditions," *Corros. Sci.*, vol. 42, no. 10, pp. 1669–1683, 2000.

[47] R. Stumper, "La corrosion du fer en presence du sulfure de fer," *Compt. Rend. Acad. Sci.(Paris)*, vol. 176, p. 1316, 1923.

[48] R. King, J. Miller, and J. Smith, "Corrosion of mild steel by iron sulphides," *Br. Corros. J.*, vol. 8, no. 3, pp. 137–141, 1973.

[49] "Tafel.png," November 2013.

[50] "Carbon steel: AISI 1008," Dec. 2013.

[51] E. McCafferty, "Validation of corrosion rates measured by the tafel extrapolation method," *Corrosion science*, vol. 47, no. 12, pp. 3202–3215, 2005.

[52] A. Davoodi, M. Pakshir, M. Babaiee, and G. Ebrahimi, "A comparative H2S corrosion study of 304L and 316L stainless steels in acidic media," *Corrosion Science*, vol. 53, no. 1, pp. 399–408, 2011.

[53] D. Rickard, "Kinetics of fes precipitation: Part 1. competing reaction mechanisms," *Geochimica et cosmochimica acta*, vol. 59, no. 21, pp. 4367–4379, 1995.

[54] J.-A. Bourdoiseau, M. Jeannin, R. Sabot, C. Rémazeilles, and P. Refait, "Characterisation of mackinawite by raman spectroscopy: Effects of crystallisation, drying and oxidation," *Corrosion Science*, vol. 50, no. 11, pp. 3247–3255, 2008.